MASTERARBEIT

Titel der Masterarbeit

Testing the feasibility of calculating stellar and gaseous true circular velocities from CALIFA IFU data

Verfasser

Markus Arzt, BSc BSc

angestrebter akademischer Grad

Master of Science (MSc)

Wien, Jänner 2014

Studienkennzahl lt. Studienblatt:	A 066-861
Studienrichtung lt. Studienblatt:	Masterstudium Astronomie
Betreuerin / Betreuer:	Univ.-Prof. Dipl.-Phys. Dr. Bodo Ziegler

Abstract - English and German

Based on the **C**alar **A**lto **l**egacy **i**ntegral **f**ield spectroscopy **a**rea (CALIFA) survey sample available in December 2012, a small sample of 10 galaxies has been selected based on various criteria, whereof the inclusion of different morphological types was the driving one.
The stellar and gaseous kinematics of these galaxies had been analysed separately, as these constituents of a galaxy behave differently in the presence of turbulence. In addition to the gravitational velocity dispersion that stars show, the gaseous statistics is also composed of a well constrained fraction of thermal motion, as well as a so far unquantified fraction of turbulent motion.
To disentangle these different causes of velocity dispersion is a non-trivial problem, which was tackled by Weijmans et al. (2008), but necessary in order to obtain the true circular velocity, which traces the gravitational potential.

This attempt is based on the idea that turbulence is only present in the center of a galaxy and the knowledge that the different behaviour of a galaxies' components is imprinted in their associated true circular velocities.
To obtain the true circular velocity of a galaxy an asymmetric drift correction has to be applied. The magnitude of the correction term will vary with radius. But according to Weijmans et al. (2008) a reliable estimation of the gravitational contribution to the velocity dispersion of the gas can be found by first ignoring turbulence and later assuming a constant asymmetric drift correction with radius.
Assuming the constant value to be the amplitude of the asymmetric drift correction of the first approach at large radii is equivalent to remove turbulence from the observed velocity dispersion. As the difference of this corrected true circular velocity, which should coincide with the true circular velocity of the stars, and the circular velocity of the first approach is solely due to a different velocity dispersion, the calculation can be done in the reverse direction to estimate the contribution of each velocity dispersion agent.

The analysis of Weijmans et al. (2008) showed that turbulence is the major contributor to the observed velocity dispersion of NGC2974 up to 8 arcsec. Following the same procedure as in that paper, it was possible to obtain reliable results for the stellar true circular velocities using the CALIFA data. Unfortunately, the analysis of the gaseous data was not successful, in the sense that the asymmetric drift correction of most of the galaxies did not reach a plateau at larger radii, i.e., an estimation of the gravitational contribution to the velocity dispersion was not possible.
The data of the gas kinematics was not binned, which implies a low signal-to-noise ratio. Therefore the low spectral resolution line Hα + [NII] (unresolved) had to be used instead of the [OIII] line, is available in high spectral resolution. As the true circular velocity of the stars seems reasonable, the input data is expected to be the problem in the analysis.

Aufgrund diverser Kriterien, wovon die wichtigste eine möglichst lückenlose Abdeckung der Hubbletypen war, wurde eine kleine Auswahl von 10 Galaxien aus dem im Dezember 2012 zur Verfügung stehenden Katalog des **C**alar **A**lto **l**egacy **i**ntegral **f**ield spectroscopy **a**rea (CALIFA) Programm ausgewählt.
Da die Kinematik von Sternen und Gas sich in Anwesenheit von Turbulenzen deutlich unterscheiden, wurden diese Bestandteile getrennt von einander analysiert. Zusätzlich zur gravitativen Geschwindigkeitsdispersion üben bei der Gasstatistik auch noch, derzeit nicht quantifizierte, turbulente Phänomene und fast vernachlässigbare thermische Bewegung einen Einfluss aus.
Die einzelnen Ursachen der Geschwindigkeitsdispersion gesondert zu erhalten stellt ein nicht triviales Problem dar, allerdings nötig zur Ermittlung der wahren Kreisgeschwindigkeit, welche die Berechnung des Gravitationspotential erlaubt. Einen Versuch, dieses Problem zu lösen, zeigen Weijmans et al. (2008) auf.

Dieser Versuch beruht auf der Idee, dass sich Turbulenz nur im Zentrum von Galaxien ausbilden kann, und dem Wissen, dass sich das unterschiedliche Verhalten von Sternen und Gas in Gegenwart von Turbulenz in der wahren Kreisgeschwindigkeit abbildet.
Die wahre Kreisgeschwindigkeit unterscheidet sich von der beobachteten Rotationsgeschwindigkeit durch lokale Einflüsse die man mit einer asymmetrischen Driftkorrektur quantifizieren kann. Wenn man zu Beginn naiv annimmt, dass Turbulenz vernachlässigbar ist, sollte der Korrekturwert mit dem Radius variieren und sich bei größerer Entfernung zum galaktischen Zentrum auf eine Konstante einpendeln.
Die Annahme, dass dieser Wert der Korrektur für alle Radien gültig ist, ist equivalent zur Berücksichtigung von Turbulenzen in der Geschwindigkeitsdispersion. Da sich die aus dieser Annahme ergebende wahre Kreisgeschwindigkeit, welche der wahren Kreisgeschwindigkeit der Sterne entsprechen sollte, von jener des naiven Versuches nur durch die Werte der Geschwindigkeitsdispersion unterscheidet, kann man durch Umkehr des Rechenweges die Geschwindigkeitsdispersion in ihre Bestandteile aufspalten.

Die Analyse von Weijmans et al. (2008) zeigt, dass Turbulenzen den Hauptbestandteil der Geschwindigkeitsdispersion von NGC2974 bis zu einem Radius von 8 arcsec ausmachen. Anhand dieses Artikels war es mir möglich, vertrauenswürdige Resultate für die wahre Kreisgeschwindigkeit der Sterne aus den CALIFA Daten abzuleiten. Leider schlug jedoch die Analyse bei den Gasdaten fehl, da sich kein konstanter Wert der asymmetrischen Driftkorrektur bei großer Distanz zum galaktischen Zentrum ausbildete und, in Folge dessen der gravitative Einfluss auf die Geschwindigkeitsdispersion nicht abgeschätzt werden konnte.
Die Gasdaten standen leider nur per Spaxel zur Verfügung und damit einhergehend mit einem geringen Signal-zu-Rausch Verhältnis. Deshalb konnte für die Analyse nur die in geringer spektraler Auflösung vorhandene Linie Hα + [NII] (nicht aufgelöst) verwendet werden, anstatt der, bei hoher spektraler Auflösung verfügbaren, [OIII] Linie. Da die Methodik für die Sternkinematik vernünftige Ergebnisse lieferte, liegt das Problem wohl bei den Eingangsdaten der Gaskinematik.

Acknowledgments

I want to thank Bodo Ziegler, Glenn ven de Ven and their groups, emphasising the contribution of Oliver Czoske, for the opportunity and support during the process of writing this thesis and the rest of the CALIFA team, in particular Begona Garcia Lorenzo and Jesus Falcon Barroso, for providing the reduced data of the analysed galaxies.
Furthermore I want to thank Christoph, Roman and Philipp for the division of work and the fun during our studies.
Last but not least I want to thank my family. Without their support this thesis and my whole academic experience would not have been possible.

Contents

Introduction

For this thesis I was drawn back to my bachelor topic cosmology, which offers many interesting questions to be answered. Cosmology deals with one of the oldest of all questions of mankind: Where do we come from? It is often topic and inspiration in art, e.g. Paul Gauguin, Henk Wieman, The Bible. Therefore cosmology and myself, by writing about it, are in the fortunate position of no need for justification, since it is mankind inherited. Simply how I take part in answering this question with what I am doing is sometimes a challenge when speaking to other people.

The field of astrophysics is concerned with the formation, evolution and death of celestial objects. In the case of cosmology it is the universe itself and its major visible components, the galaxies, which are the objects of interest.
Only about 6% of the universe can be directly detected with our current technology. The rest consists of nonbaryonic, weakly interacting dark matter (26%) and an even more mysterious relict from the inflaton field – dark energy (68%) (Ade et al., 2014). As dark matter is weakly interacting the only possibility to learn about it is through its impact on the gravitational potential of different objects. In case of galaxies the link between the visible and the invisible universe is given by the true circular velocity of stars and gas around the galactic center.
To obtain the radial true circular velocity spatial as well as spectral information about the galaxies is necessary. Both are supplied by the CALIFA project. The integral field spectrograph provides this information in the form of 3D data cubes, whereof 2 dimensions represent the projected spatial dimensions of the galaxy and the third includes the spectral information for each spatial pixel (spaxel).
From this data, it is possible to extract the velocity and velocity dispersion profiles of the stellar and gaseous components. The different kinematic reaction of stars and gas in the presence of turbulence can be used to quantify the influence of inhomogeneities and needs to be accounted for when obtaining the true circular velocity.

This thesis can be placed in the broad context of cosmology to deal with the evolution of the universe, on the one hand through looking in great detail at one temporal slice in the history of the universe and on the other hand by quantification of phenomena independent of morphological type. The last point is one step from the current qualitative description of the universe to a physical picture.

First, I will explain in Section 1 how it is possible to obtain from observations the true circular velocity and what assumptions have to be applied. In Section 2 I will discuss my sample and the criteria, which led to these galaxies. Section 3 will deal with certain steps in the data analysis, including also the computational point of view and the results will be presented in Section 4.

Chapter 1

Theory

In this chapter I describe how the measurement of the velocity can be linked to the theoretical description of a galaxy. Furthermore I will discuss the physical behaviour of the constituents of a galaxy and which corrections have to be applied in order to recover the true circular velocity from the measurements.
All of the final equations (numbered ones) have already been derived in the literature (Weijmans et al. (2008) and Binney and Tremaine (1987)). But since the intermediate steps are not always depicted in the references and the hints include typos, I will provide those here, to make it easier following the derivations. I also will highlight the assumptions along the way.

The observations of dark matter halo profiles contradict current simulations of a cold dark matter universe (Weijmans et al., 2008). The former shows core dominated profiles, while the latter predicts cuspy centers. To further investigate this problem more detailed information on the mass distribution of galaxies is necessary.
The mass distribution determines the gravitational potential, which primarily dictates the circular motion of stars and neutral and ionised gas in a galaxy. The combination of the kinematic information from these tracers of the gravitational potential provides a complete picture of a galaxies mass distribution. But in order to find the correct gravitational potential and therefore mass distribution corrections for all other influences must be applied.

Since the density of stars is rather small, their velocity dispersion emerges solely due to gravitational influences via dynamical friction, which lowers the observed circular velocities. Therefore the observed velocity does not trace the gravitational potential. The difference between the observed and the true circular velocity can be corrected by an **a**symmetric **d**rift **c**orrection (ADC).
For gas the measured velocity dispersion includes additional contributions from thermal and turbulent motions (Weijmans et al., 2008).

$$\sigma_{\text{obs}}^2 = \sigma_{\text{thermal}}^2 + \sigma_{\text{turb}}^2 + \sigma_{\text{grav}}^2 \tag{1.1}$$

The thermal motion emerging from the temperature of the gas is random and contributes only to the dispersion and not to the ordered circular motion of the gas. The same applies for turbulent phenomena like shocks. To obtain the correct true circular velocity of the gas, it is essential to first know the quantitative contribution of the different velocity dispersion components.

According to the three phase model (McKee and Ostriker, 1977) ionised gas should have a temperature of about 10^4 Kelvin. Therefore, the thermal contribution is quite small and can be approximated to be 10 km s^{-1} assuming a Maxwellian velocity distribution.
Turbulent motions are primarily expected to be found near galactic centers. Neutral gas shows an extended disc, but forms a ring around the center and therefore cannot be found in the inner parts of a galaxy. In contrast, the ionised gas can only be found in the central part of the galaxies, which makes it the best candidate for quantifying turbulence. But to disentangle the remaining two constituents of the velocity dispersion, a full analysis of the stellar and ionised gas rotation curve performing an ADC is necessary, as will be shown in this chapter.
Besides the calculation of the true circular velocity of the ionised gas, the quantification of turbulence near galactic centers allows other investigations, e.g., the relation of black hole masses to the gaseous velocity dispersion of the corresponding bulge (Verdoes-Kleijn et al., 2004).

The most precise measureable quantity of other galaxies, besides the flux, is the velocity, using spectroscopy. Due to the projection from 3D onto 2D, the signal we get is not from one single point in the galaxy but represents the **l**ine **o**f **s**ight **v**elocity **d**istribution (LOSVD). Binney and Tremaine (1987) showed that the connection between the observables, mean line-of-sight velocity $v_{\|}$ and mean line of sight velocity dispersion $\sigma_{\|}^2$, and the theoretical model is given by the probability of finding a certain star at a fixed position

$$\nu(\mathbf{x}) \equiv \int f(\mathbf{x}, \mathbf{v})\ d^3v \tag{1.2}$$

where $f(\mathbf{x}, \mathbf{v})$ is the distribution function explained in Section 1.1, the mean velocity

$$\overline{\mathbf{v}}(\mathbf{x}) = \frac{1}{\nu(\mathbf{x})} \int \mathbf{v} f(\mathbf{x}, \mathbf{v})\ d^3v \tag{1.3}$$

and the symmetric velocity dispersion tensor, which defines the shape of the velocity ellipsoide

$$\sigma_{ij}^2 = \frac{1}{\nu(\mathbf{x})} \int (v_i - \overline{v}_i)(v_j - \overline{v}_j) f(\mathbf{x}, \mathbf{v})\ d^3v = \overline{v_i v_j} - \overline{v}_i \overline{v}_j \tag{1.4}$$

1.1 The Collisionless Boltzmann Equation

In analogy to thermodynamics, a complex system like a galaxy cannot be described by the motion of the individual particels, e.g., stars, but by the probability of finding a star in a certain volume element in the 6D phase space. In following closely the reasoning of Binney and Tremaine (1987) it is practical to define the **d**istribution **f**unction (DF) $f(\mathbf{x}, \mathbf{v}, t)$ as the probability of finding a certain star in a volume element of the phase space at some point in time. A trivial property of the DF is that the integral of the DF over the whole space must be equal to 1 at all times.

Under the assumption that no stars are born or destroyed, which is reasonable on a short timescale, the probability is a conserved quantity. The mathematical description is the same as for mass in fluid dynamics.

$$\frac{\partial f}{\partial t} + \frac{\partial (f \dot{\mathbf{w}})}{\partial \mathbf{w}} = 0 \tag{1.5}$$

where $\mathbf{w}$ is an arbitrary set of canonical coordinates q and p.

Eliminating $\dot{\mathbf{w}}$ using Hamilton's equation and Schwarz' theorem[1] leads to the **c**ollisionless **B**oltzmann **e**quation (CBE)

$$\frac{\partial f}{\partial t} + \dot{\mathbf{q}} \cdot \frac{\partial f}{\partial q} + \dot{\mathbf{p}} \cdot \frac{\partial f}{\partial p} = \frac{\partial f}{\partial t} + [f, H] = 0 \tag{1.6}$$

A disc dominated galaxy, especially a spiral galaxy, is best described by a rotating disc. Therefore standard **cylindrical coordinates** are the natural choice to describe such a system.

$$x = r\cos\varphi \qquad y = r\sin\varphi \qquad z = z$$

The Hamiltonian then becomes

$$H = \frac{1}{2}\mathbf{p}^2 + \Phi(\mathbf{q}, t) = \frac{1}{2}(\dot{r}^2 + r^2\dot{\varphi}^2 + \dot{z}^2) + \Phi(\mathbf{q}, t) \tag{1.7}$$

and by inserting in equation 1.6 the CBE in cylindrical coordinates can be obtained.

$$\frac{\partial f}{\partial t} + \frac{\partial f}{\partial r}\dot{r} + \frac{\partial f}{\partial \varphi}r^2\dot{\varphi} + \frac{\partial f}{\partial z}\dot{z} + \frac{\partial f}{\partial \dot{r}}\left(r\dot{\varphi}^2 - \frac{\partial \Phi}{\partial r}\right) - \frac{\partial f}{\partial \dot{\varphi}}\frac{\partial \Phi}{\partial \varphi} + \frac{\partial f}{\partial \dot{\varphi}}\,\dot{r}\dot{\varphi} - \frac{\partial f}{\partial \dot{z}}\frac{\partial \Phi}{\partial z} = 0 \tag{1.8}$$

1.2 Axisymmetric Jeans Equations

The CBE is a first step towards the full description of a galaxy, but the dependence of the form of the DF on the observables is still unknown. The Jeans theorem states that any integral of motion[2] is a solution of the steady-state CBE and all solutions to the steady-state CBE depend on the phase space coordinates through the integrals of motion (Mo et al., 2013) or in its strong version:

[1] If H has continuous second partial derivatives at any given point in $\mathbb{R}^n$, the partial derivations of this function are commutative (Bronstein et al., 2008).

[2] A function I of the coordinates which is constant along a trajectory in phase space (Weisstein, 2013a), i.e., $dI/dt = 0$.

The DF of a steady-state stellar system in which almost all orbits are regular with non-resonant frequencies may be presumed to be a function only of three independent isolating integrals, which may be taken to be the actions. (Binney and Tremaine, 1987)

An axisymmetric potential is a realistic ansatz for the orbits of stars in a galaxy. Taking advantage of the conservation of angular momentum around the z axis, the 3D motion can be reduced to a motion in the meridional plane, i.e., independent of φ. Richstone (1982) showed that there exists a third integral I_3, in addition to the classical integrals of motion H and L_z, for which we so far have unfortunately no analytical expression. Those integrals of motion fully describe the DF.

In cases where the DF does not or only in a simple way depend on the third integral, analytical solutions exist. For more complicated systems two different approaches can be applied.
A numerical, orbit-based approach (Schwarzschild, 1979) is to take the observed density distribution and put a grid above it. Then the gravitational potential can be obtained and a huge number of orbits can be calculated (orbit data base). Comparing the time averaged orbital densities with the measurements and performing optimisation by assigning non-negative weights to the orbits is equivalent to finding the DF of the system (de Zeeuw, 2012).

The second one, which will be applied in this thesis, is based on the Jeans theorem stated above. Not the DF itself, but its moments will be used to describe the dynamics of a galaxy.
By multiplying the **axisymmetric**, **steady state** form of equation 1.8 with the velocity v_i and integrating over all velocities the three Jeans equations can be obtained.

$$\int d^3v\ \frac{\partial f}{\partial r} v_r v_i + \int d^3v\ \frac{\partial f}{\partial z} v_z v_i + \int d^3v\ \frac{\partial f}{\partial v_r} \frac{v_\varphi^2 v_i}{r} + \int d^3v\ \frac{\partial f}{\partial v_\varphi} \frac{v_r v_\varphi v_i}{r} - \int d^3v\ \frac{\partial f}{\partial v_r} \frac{\partial \Phi}{\partial r} v_i - \int d^3v\ \frac{\partial f}{\partial v_z} \frac{\partial \Phi}{\partial z} v_i = 0$$

According to Leibniz's rule (Weisstein, 2013b) the derivatives in the first two terms can be written in front of the integral, as the DF and its derivatives are continuous and the spatial coordinates are independent of the velocity. The other terms can be transformed using partial integration, with the goal of getting rid of the derivative of the DF.

$$\frac{\partial}{\partial r} \int d^3v\ f v_r v_i + \frac{\partial}{\partial z} \int d^3v\ f v_z v_i + \int d^3v\ f \frac{\partial (v_\varphi^2 v_i / r)}{\partial v_r} + \int d^3v\ f \frac{\partial (v_r v_\varphi v_i / r)}{\partial v_\varphi} + \frac{\partial \Phi}{\partial r} \int d^3v\ f \frac{\partial v_i}{\partial v_r} + \frac{\partial \Phi}{\partial z} \int d^3v\ f \frac{\partial v_i}{\partial v_z} = 0$$

Performing the derivatives with respect to the velocities and using Equations 1.2 and 1.3, the final results can be obtained for $v_i = v_r, v_\varphi, v_z$.

$$\frac{\partial(\nu\overline{v_r^2})}{\partial r} + \frac{\partial(\nu\overline{v_z v_r})}{\partial z} + \frac{\nu\overline{v_\varphi^2}}{r} + \frac{\nu\overline{v_r^2}}{r} = -\nu\frac{\partial\Phi}{\partial r} \tag{1.9a}$$

$$\frac{\partial(\nu\overline{v_r v_\varphi})}{\partial r} + \frac{\partial(\nu\overline{v_z v_\varphi})}{\partial z} + \frac{2\nu\overline{v_r v_\varphi}}{r} = 0 \tag{1.9b}$$

$$\frac{\partial(\nu\overline{v_r v_z})}{\partial r} + \frac{\partial(\nu\overline{v_z^2})}{\partial z} + \frac{\nu\overline{v_r v_z}}{r} = -\nu\frac{\partial\Phi}{\partial z} \tag{1.9c}$$

1.3 Asymmetric Drift Correction

The asymmetric drift is the difference between the velocity of a perfect circular orbit and the measured mean rotational velocity (Golubov and Just, 2012), due to surface density and velocity dispersion gradients (Binney and Tremaine, 1987) and can be directly derived from the Jeans equations. As the circular velocity traces the potential of a galaxy, the goal is to obtain an expression of this quantity including only observables. Furthermore, under certain assumptions, the velocity dispersion is split into its different contributions as a by-product, which is important for this thesis.
Starting with equation 1.9a and inserting the expression for the circular velocity $v_c^2 = r \cdot \partial\Phi/\partial r$ gives

$$\frac{\partial(\nu\overline{v_r^2})}{\partial r} + \frac{\partial(\nu\overline{v_z v_r})}{\partial z} - \frac{\nu}{r}\left(\overline{v_\varphi^2} - \overline{v_r^2} - v_c^2\right) = 0 \tag{1.10}$$

which can be transformed evaluating the derivatives and using that $\partial\nu/\partial z = 0$ in the disc plane due to symmetry. At that point the expressions for the velocity dispersions $\sigma_r^2 = \overline{v_r^2}$, $\sigma_\varphi^2 = \overline{v_\varphi^2} - \overline{v_\varphi}^2$ and $\sigma_z^2 = \overline{v_z^2}$ will be introduced.

$$\frac{\partial\nu}{\partial r}\sigma_r^2 + \frac{\partial\sigma_r^2}{\partial r}\nu + \frac{\partial\overline{v_r v_z}}{\partial z}\nu - \frac{\nu}{r}\left(\sigma_\varphi^2 + \overline{v_\varphi}^2 - \overline{v_r^2} - v_c^2\right)$$

Multiplying by r/ν and re-arranging leads to

$$v_c^2 = \overline{v_\varphi}^2 - \sigma_r^2\left(\frac{\partial\ln\nu}{\partial\ln r} + \frac{\partial\ln\sigma_r^2}{\partial\ln r} + 1 - \frac{\sigma_\varphi^2}{\sigma_r^2} + \frac{r}{\sigma_r^2}\frac{\partial\overline{v_r v_z}}{\partial z}\right) \tag{1.11}$$

By aligning the velocity ellipsoid with the coordinate system an expression for $\overline{v_r v_z}$ can be obtained. In case of alignment with the cylindrical coordinate system the expression would be zero, but not if aligned with the spherical coordinate system. To be able to vary the alignment the parameter κ is introduced and the expression in the thin disc approximation reads

$$\overline{v_r v_z} = (\sigma_r^2 - \sigma_z^2)\frac{\kappa z}{r}\begin{cases}\kappa = 0 & \text{alignment with cylindrical coordinate system}\\ \kappa = 1 & \text{alignment with spherical coordinate system}\end{cases} \tag{1.12}$$

Performing the derivative gives

$$v_c^2 = \overline{v_\varphi}^2 - \underbrace{\sigma_r^2 \left[\frac{\partial \ln \nu}{\partial \ln r} + \frac{\partial \ln \sigma_r^2}{\partial \ln r} + 1 - \frac{\sigma_\varphi^2}{\sigma_r^2} + \kappa \left(1 - \frac{\sigma_z^2}{\sigma_r^2} \right) \right]}_{\text{asymmetric drift correction}}$$

Expression for $\sigma_\varphi^2 \ / \ \sigma_r^2$

Not all of these quantities can be observed or extracted from observations. To obtain the missing expressions, higher order velocity moments of the CBE have to be calculated. Starting by multiplying the CBE with $v_r v_\varphi$ and integrating over all velocities leads to

$$\frac{\partial(\nu \overline{v_r^2 v_\varphi})}{\partial r} + \frac{\partial(\nu \overline{v_r v_\varphi v_z})}{\partial z} + \frac{2\nu \overline{v_r^2 v_\varphi}}{r} - \frac{\nu \overline{v_\varphi^3}}{r} + \frac{\partial \Phi}{\partial r} \ \nu \overline{v_\varphi} = 0 \qquad (1.13)$$

The expectation value $\overline{XY}$ is linear and in case of uncorrelated variables X and Y also multiplicative. Generalised coordinates are by definition uncorrelated and the distribution function can be factorised in case of alignment with the coordinate system. Therefore the expressions $\overline{v_r^2(v_\varphi - \overline{v_\varphi})} = 0$ and $\overline{v_r v_z (v_\varphi - \overline{v_\varphi})} = 0$ hold, which are equivalent to $\overline{v_r^2 v_\varphi} = \sigma_r^2 \overline{v_\varphi}$ and $\overline{v_r v_\varphi v_z} = \overline{v_r v_z} \ \overline{v_\varphi}$. Inserting those into the equation reveals the expression

$$\frac{\partial(\nu \sigma_r^2)}{\partial r} \ \overline{v_\varphi} + \frac{\partial \overline{v_\varphi}}{\partial r} \ \nu \sigma_r^2 + \frac{\partial(\nu \overline{v_r v_z})}{\partial z} \ \overline{v_\varphi} + \frac{\partial \overline{v_\varphi}}{\partial z} \ \nu \overline{v_r v_z} - \frac{\nu}{r} \left(\overline{v_\varphi^3} - \frac{\partial \Phi}{\partial r} \ r \overline{v_\varphi} - 2\sigma_r^2 \overline{v_\varphi} \right) = 0$$

The similarity to Equation 1.10 suggests multiplying Equation 1.10 with $\overline{v_\varphi}$ and subtracting from the previous one, which results in

$$\frac{\partial \overline{v_\varphi}}{\partial r} \ \sigma_r^2 + \frac{\partial \overline{v_\varphi}}{\partial z} \ \overline{v_r v_z} - \frac{\overline{v_\varphi^3} - \overline{v_\varphi^2} \ \overline{v_\varphi} - \sigma_r^2 \overline{v_\varphi}}{r} = 0 \qquad (1.14)$$

Expanding the expression $\overline{(v_\varphi - \overline{v_\varphi})^3}$ enables the next step in the derivation.

$$\overline{(v_\varphi - \overline{v_\varphi})^3} = \overline{v_\varphi^3} + \underbrace{3 \ \overline{v_\varphi \overline{v_\varphi}^2} - 3 \ \overline{v_\varphi^2 \overline{v_\varphi}} - \overline{v_\varphi}^3}_{2 \ \overline{v_\varphi} \underbrace{(\overline{v_\varphi}^2 - \overline{v_\varphi^2})}_{-\sigma_\varphi^2} - \overline{v_\varphi} \ \overline{v_\varphi^2}}$$

By first substituting $\overline{v_\varphi^3} - \overline{v_\varphi^2} \ \overline{v_\varphi} = 2\sigma_\varphi^2 \overline{v_\varphi} + \overline{(v_\varphi - \overline{v_\varphi})^3}$ and using Equation 1.12 some terms can be eliminated. By multiplying with $r/(\sigma_r^2 \overline{v_\varphi})$ and re-arranging the final expression for $\sigma_\varphi^2 / \sigma_r^2$ can be obtained.

$$\frac{\sigma_\varphi^2}{\sigma_r^2} = \frac{1}{2} \left[1 + \underbrace{\frac{\partial \ln \overline{v_\varphi}}{\partial \ln r}}_{\alpha_r} + \underbrace{\frac{\partial \ln \overline{v_\varphi}}{\partial \ln z}}_{\alpha_z} \ \kappa \left(1 - \frac{\sigma_z^2}{\sigma_r^2} \right) - \underbrace{\frac{\overline{(v_\varphi - \overline{v_\varphi})^3}}{\sigma_r^2 \overline{v_\varphi}}}_{\text{almost zero}} \right] \qquad (1.15)$$

Expression for σ_z^2 / σ_r^2

Starting again with the CBE, this time multiplied with $v_z v_\varphi$, and integrating over all velocities leads to

$$\frac{\partial[\nu\overline{v_r v_z v_\varphi}]}{\partial r} + \frac{\partial[\nu\overline{v_z^2 v_\varphi}]}{\partial z} + \frac{\partial\Phi}{\partial z}\ \nu\overline{v_\varphi} + \frac{2\nu\overline{v_r v_\varphi v_z}}{r} = 0$$

Looking again for similarities with the Jeans equations suggests multiplying 1.9c with $\overline{v_\varphi}$ and subtracting the expression above to obtain

$$\underbrace{\frac{\partial[\nu\overline{v_r v_z v_\varphi}]}{\partial r} - \frac{\partial(\nu\overline{v_r v_z})}{\partial r}\ \overline{v_\varphi}}_{\frac{\partial\overline{v_\varphi}}{\partial r}\ \nu\overline{v_r v_z}} + \underbrace{\frac{\partial[\nu\overline{v_z^2 v_\varphi}]}{\partial z} - \frac{\partial(\nu\overline{v_z^2})}{\partial z}\ \overline{v_\varphi}}_{\frac{\partial\overline{v_\varphi}}{\partial z}\ \nu\overline{v_z^2}} + \frac{2\nu\overline{v_r v_\varphi v_z}}{r} - \frac{\nu\overline{v_r v_z}\ \overline{v_\varphi}}{r} = 0$$

After multiplying this equation with z/v_φ one finds

$$\alpha_r\nu\ \overline{v_r v_z}\ \frac{z}{r} + \nu\ \overline{v_r v_z}\ \frac{z}{r} + \alpha_z\nu\sigma_z^2 = 0 \tag{1.16}$$

Inserting equation 1.12 and dividing by $\alpha_z \cdot \sigma_r^2$ and re-arranging yields the final expression for σ_z^2/σ_r^2.

$$\frac{\sigma_z^2}{\sigma_r^2} = -\frac{(1+\alpha_r)\kappa z^2}{\alpha_z r^2 - (1+\alpha_r)\kappa z^2} \tag{1.17}$$

Final result for v_c^2

Inserting the obtained expressions into the preliminary results of the ADC correction gives the final result for performing the ADC including only observable quantities.

$$v_c^2 = \overline{v_\varphi}^2 - \sigma_r^2\left[\frac{\partial\ln\nu}{\partial\ln r} + \frac{\partial\ln\sigma_r^2}{\partial\ln r} + \frac{1}{2}(1-\alpha_r) + \left(1-\frac{\alpha_z}{2}\right)\frac{\kappa\alpha_z r^2}{\alpha_z r^2 - (1+\alpha_r)\kappa z^2}\right]$$

Anticipating the results of Section 3.3 the derivatives of the velocity profile can be inserted explicitly and the equation can be evaluated in the disc plane (Weijmans et al., 2008).

$$v_c^2 = \overline{v_\varphi}^2 - \underbrace{\sigma_r^2\left(\frac{\partial\ln\Sigma}{\partial\ln r} + \frac{\partial\ln\sigma_r^2}{\partial\ln r} + \frac{r^2}{2R_{\rm mod}^2} + \frac{\kappa r^2}{\kappa(2R_{\rm mod}^2 - r^2) + r^2}\right)}_{\text{asymmetric drift correction}} \tag{1.18}$$

As a thin disc has been assumed already, the surface brightness Σ can be used as an approximation for the density function ν (Weijmans et al., 2008). The modified radius $R_{\rm mod}$ will be introduced later, when fitting the radial velocity profile (see Section 3.3).
This important result allows to link the observations with theoretical models based on a small number of assumptions. Most of them seem reasonable, but the thin disc approximation could be problematic for the analysis of some of the selected galaxies, although the sample of this thesis includes only fast rotators.

Chapter 2

The Sample

The team of the CALIFA survey observes galaxies at the Calar Alto 3.5m telescope with the PMAS/PPAK instrument using two different setups (Husemann et al., 2013).

V500 Wavelength: 3650 - 7500 Å, Resolution: 850, FWHM: 6.0 Å, τ_{exp}: 900 s

V1200 Wavelength: 3650 - 4840 Å, Resolution: 1650, FWHM: 2.3 Å, τ_{exp}: 1800 s

The data has been reduced by the CALIFA team. The stellar kinematics has been extracted from the best continuum fit to the data, while for the gas kinematics the emission line of different elements has been used. The emission lines have been obtained by subtracting the best continuum fit from the raw data. Datacubes for the stellar kinematics and for each of the emission lines have been provided separately.
The data cubes for each of the emission lines provide the information on the spatial coordinates together with the flux, the velocity, the velocity dispersion and the signal-to-noise ratio at each spaxel. Additionally to these parameters, the datacubes of the stellar continuum include the same properties in binned form (Cappellari and Copin, 2003) to provide a minimum signal-to-noise ratio of 20 per spaxel (Garcia-Lorenzo et al., 2014).

The high spectral resolution V1200 setup covers the [OII], Hδ + Hγ emission lines of the ionised gas, while Hα + [NII] and [OIII] are available in the lower resolution V500 setup. For global structure phenomena, e.g, position angle, also a combined data cube of the two setups has been provided by the CALIFA team. Due to dithering, the spatial resolution of the V1200 setup and the combined data improved from originally 2 to 1 arcsec.
The sample studied in this thesis was taken from 176 stellar kinematic maps and 120 gas kinematic maps from the CALIFA isophotal diameter-limited ($45'' <$

$D_{25} < 80''$) and redshift constrained ($0.005 < z < 0.3$) mother sample (Husemann et al., 2013) that were first analysed.
The selection criteria for the analysed sample were checked only by eye. All galaxy maps were ranked according to the following criteria:

Completeness of the Sample The analysis should be applicable to all kind of morphological galaxy types, which was provided by splitting the sample in 50% late type and 50% early type galaxies. Unfortunately it was not possible to find elliptical galaxies fulfilling the other criteria, thus the group consists of early type galaxies only of S0 galaxies.

Velocity Structure of the Galaxy Emsellem et al. (2011) showed the existence of two types of galaxies – slow and fast rotators. The latter show ordered motion and can be considered to be disc dominated. In order to satsify the assumptions of Chapter 1 it is crucial that the galaxies of the sample belong to the group of fast rotators.

Completeness of the Map Some parts will be neglected during the analysis to avoid wrong input data from noisy spaxels and others will be masked due to contamination with foreground objects. Hence the kinematic map of some galaxies will look patchy, which affects the analysis described in Section 3.2.

Smoothness of the Map The kinematic map of a galaxy can show kinematic distinct areas, which cause turbulent motions. Consideration of these in the analysis would be necessary in order to find the gravitational potential and complicate the analysis unnecessarily. Therefore, only galaxies with smooth kinematic maps are choosen.

Comparability of the Sample If the kinematics of a galaxy have been analysed previously by the community, a comparison with the results obtained in this thesis would be possible.

The final selection contains the 10 galaxies given in Table 2.1.

Table 2.1: The table shows the sample analysed in this thesis.

Galaxy	Type	α(J2000)	δ(J2000)	Distance
NGC 1167	SA0	45.43	35.21	69.2 Mpc
NGC 2253	Scd	100.81	65.68	89.0 Mpc
NGC 6081	S0	241.57	18.25	156.3 Mpc
NGC 6762	S0/a	248.40	63.93	41.2 Mpc
NGC 7466	Sb	345.51	27.05	105.3 Mpc
UGC 05771	S0/a	159.33	43.59	101.8 Mpc
UGC 08778	S?	208.03	38.07	45.6 Mpc
UGC 09873	Sc	232.46	42.63	79.0 Mpc
UGC 10384	S?	246.70	11.58	69.0 Mpc
UGC 11228	SB0	276.19	41.49	81.4 Mpc

For photometric SDSS images and the kinematic maps of the stellar and gaseous components of these galaxies see Sections A.1 and A.2.

Chapter 3

Procedure

In this section I will describe the steps of the analysis. First the data will be deprojected and the system parameters will be determined. Then the radial profiles can be extracted by a fourier expansion along ellipses. Those need to be fitted, before the contributions to the velocity dispersion can be seperated. Also some information concerning the computational techniques and programs I used will be given. I will show samples of the self-written codes and describe the steps of the procedures provided by the astronomical community.

3.1 Analysis Preparation

To perform the analysis described in Section 1 it is crucial to take into account that galaxies have certain relative velocities to the observer and can have an arbitrary orientation in the sky. Therefore it is necessary to deproject the galaxies, which requires two angles.

The inclination is the angle between the line perpendicular to the galaxy disc and the line of sight (Garcia-Gomez et al., 2002) and describes whether we see the galaxy face-on or edge-on (see Figure 3.1). In the former case the inclination equals 0°. In the simple case of a thin disc with circular isophotes the inclination can be determined using the axial ratio of the galaxy (Ward, 2000).

$$i \text{ [deg]} = \cos^{-1}(q) \cdot \frac{180}{\pi} = \cos^{-1}(1-\epsilon) \cdot \frac{180}{\pi} \tag{3.1}$$

$$\Delta i \text{ [deg]} = \frac{di}{d\epsilon} \cdot \Delta\epsilon = \frac{180}{\pi\sqrt{1-(1-\epsilon)^2}} \cdot \Delta\epsilon$$

where the flattening q is the ratio of the minor axes b and major axes a. In reality, galaxies are not always well described by an infinitesimal thin disc. Due to a thick disc the axial ratio will never reach 0, i.e. one has to assume an intrinsic flattening q_0 which represents the inclination in the edge-on case.

$$\cos^2(i) = \frac{q^2 - q_0^2}{1 - q_0^2} \tag{3.2}$$

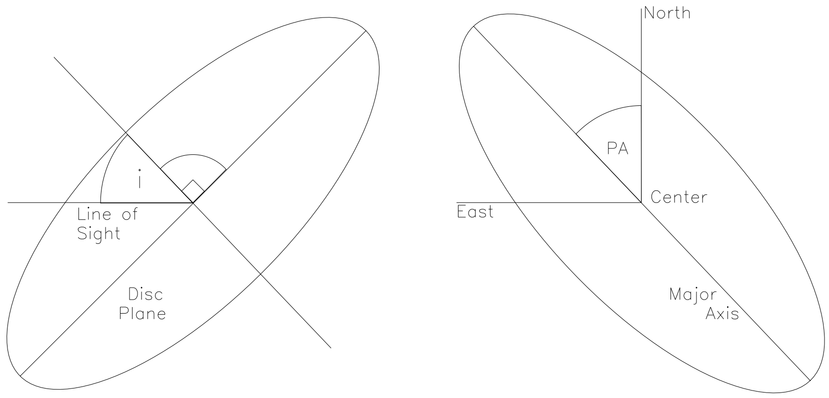

Figure 3.1: The *left panel* shows a schematic plot of the position of the inclination viewed from a position perpendicular to the line-of-sight and the *right panel* a schematic plot of the position of the position angle viewed along the line of sight.

The **p**osition **a**ngle (PA) is measured from north over east to south[1] and describes the position of the major axis relative to the north pole (see Figure 3.1). It is necessary to distinguish between the photometric and kinematic PA. The former will be used when analysing the photometry and the latter when dealing with the kinematics and can be measured, because the radial gradient of the velocity coincides with the major axis of the galaxy.

VSYS.pro & KIN_PA.pro These **I**nteractive **D**ata **L**anguage (IDL) programs extract from the input data the system velocity and the kinematic position angle. The kinematic position angle extraction is based on G. van de Vens' 'global_kin_pa', which is an advanced version of 'fit_kinematic_pa' by M. Cappellari (Krajnovic et al., 2005). The enhancements are an error estimation by weighting the bins corresponding to their uncertainties and an optimised symmetrisation (see Section 3.2) as described in van den Bosch and de Zeeuw (2012). The code for the symmetrisation had been written by R.C.E. van den Bosch and is also used for the determination of the system velocity.

Since the velocity of an emission line can be estimated to a higher precision when the resolution is better, the datacubes from the V1200 setup are used for the analysis of the system velocity.
The simplest approach to obtain the system velocity is taking the mean of all measurements. The result will be more precise when additional information, such as the symmetry properties of the velocity field are included in the analysis.

[1]Take into account that in astronomy the compass goes counterclockwise.

The kinematic position angle is a global phenomenon. Therefore the combined data cubes of the V500 and V1200 setups are used for this analysis.
First the velocities must be converted into the system, i.e., the system velocities have to be subtracted for each spaxel. Then outliers are removed using sigma clipping taking into account the velocity and the velocity dispersion. In case of a kinematic distinct core in the central region, the problematic part can be excluded. For a user provided stepsize (default is 1°) the program calculates for different position angles the χ^2 of the comparison of the binned data and a symmetrised velocity field based on the symmetry properties.

3.2 Radial Profile Extraction

The idea behind the extraction of the radial profiles is that the galaxy can be split into several ellipses. Along each of these, the considered moment of the LOSVD can be described by a superposition of simple cosine and sine functions (Fourier expansion). Krajnovic et al. (2005) showed that for a velocity map $K(a, \varphi)$ a small finite number of harmonic terms is sufficient to describe the profiles.

$$K(a, \varphi) = A_0(a) + \sum_{n=1}^{6} A_n(a) \sin(n\varphi) + B_n(a) \cos(n\varphi) \tag{3.3}$$

Here a is the semi-major axis of the considered ellipse and φ the azimuthal angle. In case of even moments the A_0 term dominates and describes the amplitude of the moment, while for odd moments the $k_1 = \sqrt{A_1^2 + B_1^2}$ is the dominant one.

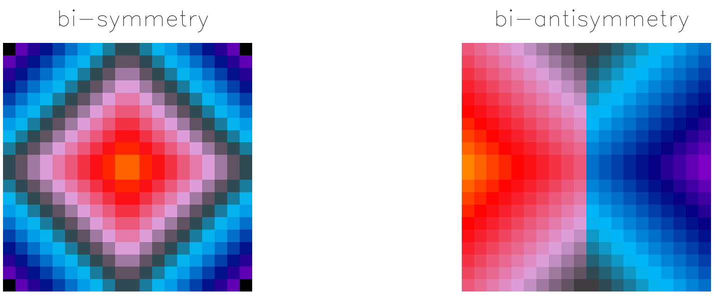

Figure 3.2: The LOSVD shows a high degree of symmetry. Even moments are bi-symmetric under the assumption of axisymmetry and odd moments bi-antisymmetric. These symmetries are used during the minimisation of kinemetry and for the calculation of the kinematic position angle.

KINEMETRY.pro Kinemetry (Krajnovic et al., 2005) itself is based on the ellipse fitting method "photometry" (see for example Bender and Moellenhoff (1987) or Jedrzejewski (1987)), but a generalisation for higher moments of the LOSVD.
For each radius the best fitting ellipse for odd moments (in axisymmetry bi-antisymmetric, see Figure 3.2), e.g. velocity, is determined by minimising the

coefficients of $\sin(x)$, $\sin(3x)$ and $\cos(3x)$ of the fourier expansion of the profile. In the case of even moments (in axisymmetry bi-symmetric, see Figure 3.2), e.g. surface brightness or velocity dispersion, the coefficients of $\sin(x)$, $\sin(2x)$, $\cos(x)$ and $\cos(2x)$ are minimised.

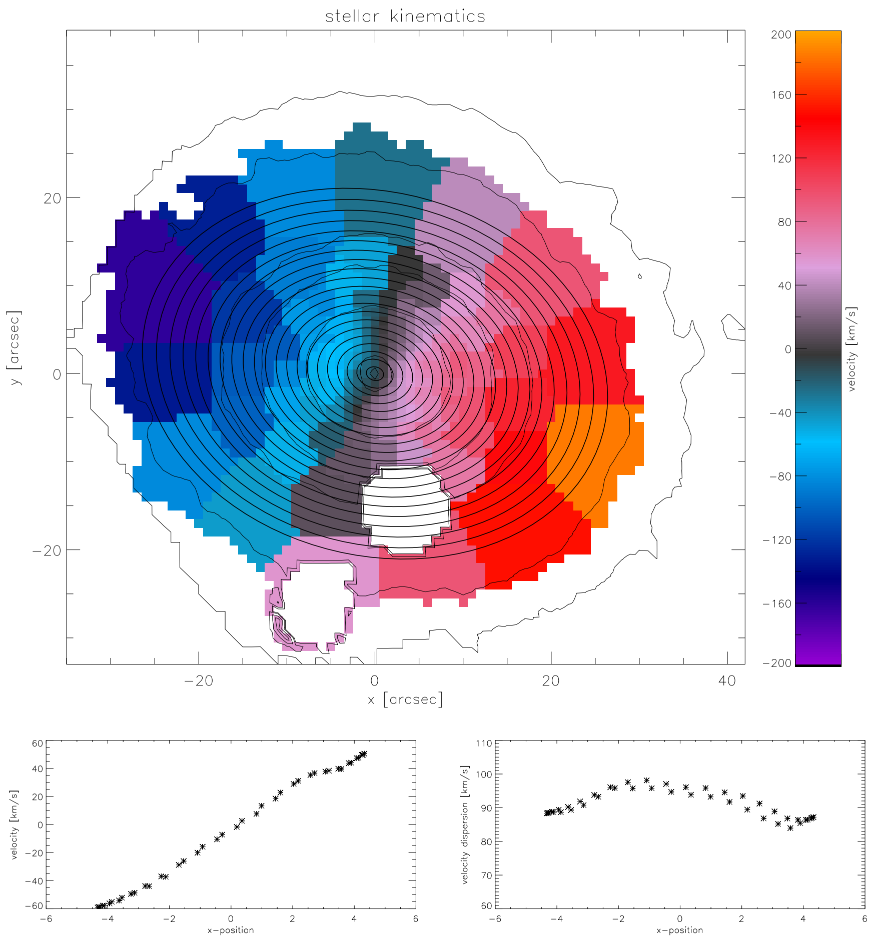

Figure 3.3: The *upper panel* shows the kinematic map of NGC1167. The Vorronoi binned data is overplotted with some isophotes and the ellipses at which profiles have been extracted. The *bottom row* shows selected profiles of the velocity (left) and the velocity dispersion (right) from the third extracted ellipse. The clear similarity of the velocity profile with a sine function and the similarity of the velocity dispersion with a cosine function is noticeable. For this representation the azimuthal coordinate is not considered.

Fitting to low quality data introduces a lot of uncertainties, which makes, in theory, the V1200 setup the best choice for all radial profile extractions, except for the zero*th* moment of the LOSVD (surface brightness).
The results of the previous analyses are solid estimates for the position angle and the inclination. Therefore, these can be fixed during the analysis, which decreases the computational costs drastically, i.e. the 2D map is rotated prior to the analysis and two parameters less have to be taken into account during minimisation. For each ellipse missing bins are interpolated and then assigned with the error of the closest pre-existing bin.

For the analysis an elliptical coordinate system is constructed and depending on the investigated moment and therefore symmetry properties the corresponding fourier coefficients are minimised (see Figure 3.3). The system of linear equations is solved using singular value decomposition and back-substitution. Finally the fourier coefficients are converted according to Krajnovic et al. (2005) for further analysis.

MGE.pro Cappellari (2002) showed that the surface brightness can be modelled efficiently by using a **m**ulti-**g**aussian **e**xpansion (MGE) method. Since the brute force method of directly fitting Gaussians to the pixels showed some convergence problems the program fits a 1D logarithmic profile to logarithmically spaced Gaussians to reach the global minimum. For a complete 2-dimensional analysis the 1D profile is analysed at several azimuthal angles. As in the case of kinemetry the center and position angle are the important parameters to correctly deproject the image. As a result, not only the surface brightness profile is obtained, but under the assumption of a certain mass-to-light ratio, also the gravitational potential, produced by the baryonic visible mass can be estimated, which allows in principle the determination of the gravitational potential.
Unfortunately the surface brightness profile extracted from SDSS data with this method did not result in a reasonable true circular velocity. Therefore, the results will be discarded immediatly and the reader is reffered to Cappellari (2002) and Cappellari (2008) for more details on MGE. The negative result of this approach may emerge from the instrumental differences between the CALIFA and SDSS surveys.

3.3 Fitting Radial Profiles

As shown in Section 1.3 the extracted radial velocity profile is not the true circular one, therefore corrections have to be applied. Drawing attention to equation 1.18, it becomes clear that fitting the profiles is necessary to obtain a stable expression for the logarithmic derivatives.

Radial Surface Brightness Profile

The extracted surface brightness profile can be well described by the double-exponential function 3.4 (bulge and disc) to reproduce the data well. Also shown is its logarithmic derivative with respect to the radius (Equation 3.5). The impact of each parameter independent of the others can be seen in Figure 3.4.

$$\ln \Sigma(r) = \Sigma_1 \; e^{-\frac{r}{R1}} + \Sigma_2 \; e^{-\frac{r}{R2}} \tag{3.4}$$

$$\frac{\partial \ln \Sigma}{\partial \ln r} = \frac{r}{\Sigma} \; \frac{d\Sigma}{dr} = -\frac{r}{\Sigma} \left(\frac{\Sigma_1}{R_1} e^{-\frac{r}{R_1}} + \frac{\Sigma_2}{R_2} e^{-\frac{r}{R_2}} \right) \tag{3.5}$$

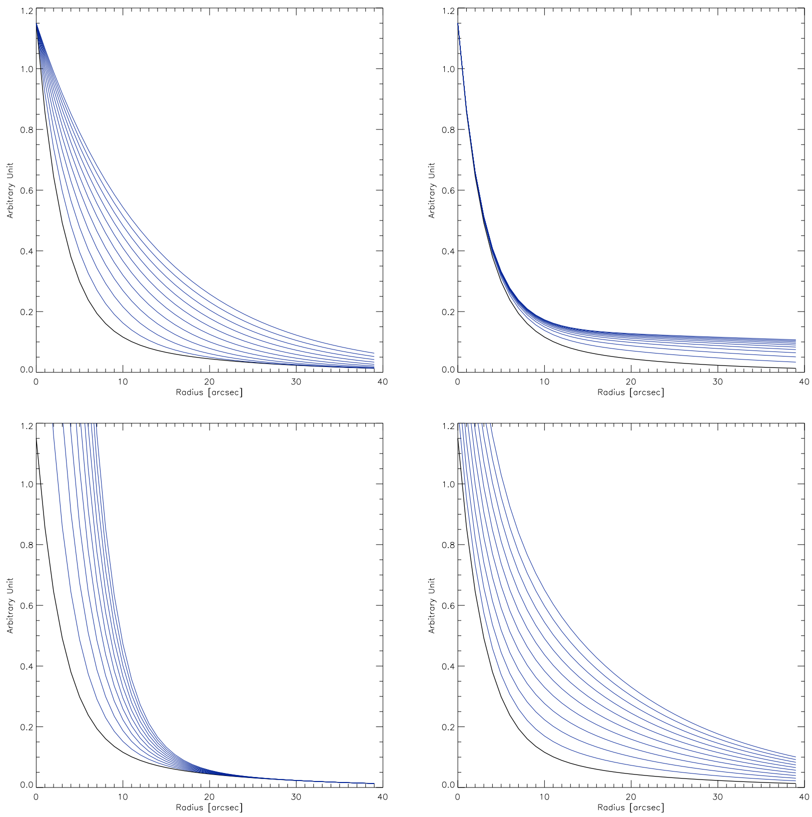

Figure 3.4: Each panel shows the variation of one parameter of the fit function of the surface brightness profile. The *top left* panel shows R_1 (3 - 13), *top right* shows R_2 (16 - 160), *bottom left* shows Σ_1 (1 - 10) and the *bottom right* panel shows the variation in Σ_2 (0.15 - 1.15). As basis of the curves the rounded results of the analysis of NGC1167 (lower limits) have been taken and the parameter under consideration has been altered with a stepsize of (upper limit - lower limits)/10. The black curve in each panel corresponds to the results of NGC1167.

Radial Velocity Profile

Using a simplified version of Evans and de Zeeuw (1994), the function

$$\overline{v_\varphi}(r,z) = \frac{v_{\text{inf}} \ \ r}{\sqrt{R_c^2 + r^2 + z^2}} = \frac{v_{\text{inf}} \ \ r}{\sqrt{R_{\text{mod}}^2 + z^2}} \tag{3.6}$$

reproduces the general features of the mean orbital motion quite well. The parameter v_{inf} is the velocity at large radii and R_c the core radius defining the slope near the center. The core radius introduces the modified radius $R_{\text{mod}}^2 = R_c^2 + r^2$. Hence the logarithmic derivatives necessary for Equation 1.18 are

$$\alpha_r = \frac{\partial \ln \overline{v_\varphi}}{\partial \ln r} = \frac{r}{\overline{v_\varphi}} \frac{\partial \overline{v_\varphi}}{\partial r} = 1 - \frac{r^2}{R_{\text{mod}}^2 + z^2} \tag{3.7a}$$

$$\alpha_z = \frac{\partial \ln \overline{v_\varphi}}{\partial \ln z} = \frac{z}{\overline{v_\varphi}} \frac{\partial \overline{v_\varphi}}{\partial z} = -\frac{z^2}{r^2}(1 - \alpha_r) \tag{3.7b}$$

The profile will be evaluated in the disc plane, i.e., $z = 0$. The influence of the remaining two parameters on the shape of the profile can be seen in Figure 3.5.

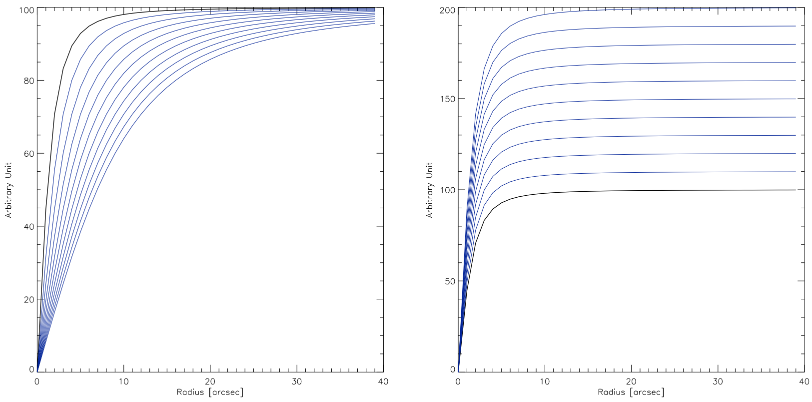

Figure 3.5: Each panel shows the variation of one parameter of the fit function of the velocity profile The *left* panel shows R_c (2 - 12) and the *right* panel shows the variation in $v_{\rm inf}$ (100 - 200). As basis of the curves the rounded results of the analysis of NGC1167 (lower limits) have been taken and the parameter under consideration has been altered with a stepsize of (upper limit - lower limits)/10. The black curve in each panel corresponds to the results of NGC1167.

Radial Velocity Dispersion Profile

The observed velocity dispersion profile can be described by a single exponential function.

$$\sigma_{\rm obs}(r) = \sigma_0 + \sigma_1 \; e^{-\frac{\sqrt{r^2+R_c^2}}{\sigma_2}} \tag{3.8}$$

The behaviour of this function can be seen in Figure 3.6. The core radius of the velocity profile is used to reproduce better the flattening towards the center. The derivative with respect to the radial coordinate is therefore

$$\frac{\partial \sigma_{\rm obs}}{\partial r} = -\frac{\sigma_1 r}{\sigma_2 R_{\rm mod}} \; e^{-\frac{\sqrt{r^2+R_c^2}}{\sigma_2}} \tag{3.9}$$

Weijmans et al. (2008) showed that the radial velocity dispersion can be derived from the observed one, when the velocity dispersion of an **axisymmetric**, **thin disc** is **evaluated in the disc plane** and **along the major axis**

$$\sigma_{\rm obs}^2 = \sigma_r^2 \underbrace{\left(1 - \frac{r^2 \sin^2 i}{2R_{\rm mod}^2} - \frac{r^2 \cos^2 i}{\kappa R_{\rm mod}^2 (2 - \frac{r^2}{R_{\rm mod}^2}) + r^2}\right)}_{a} \tag{3.10}$$

In Equation 3.10 i is the inclination, under which the galaxy is viewed. The

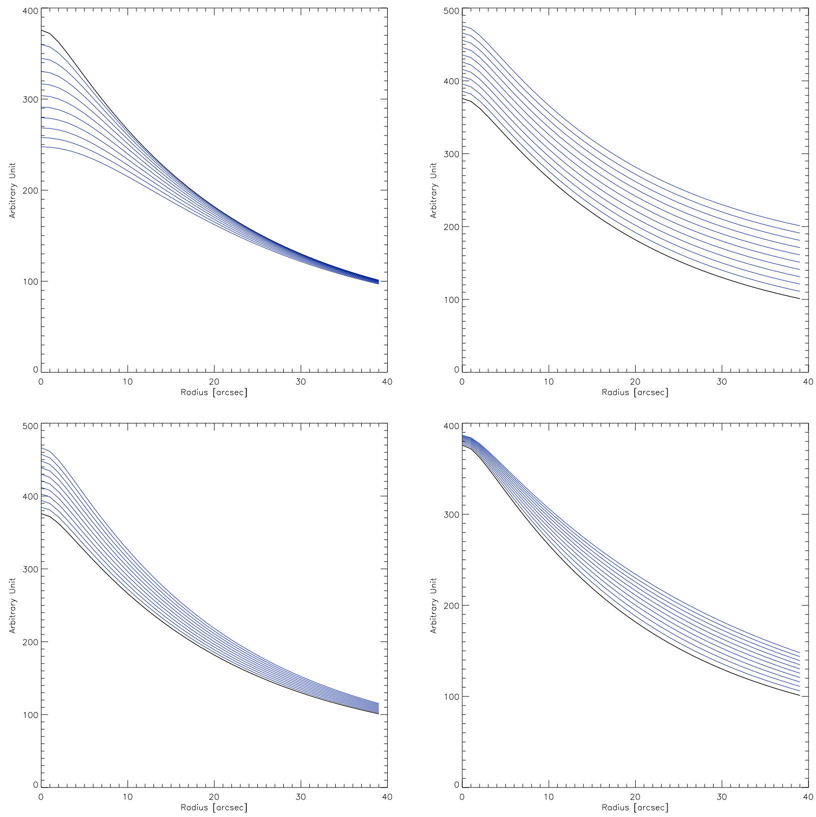

Figure 3.6: Each panel shows the variation of one parameter of the fit function of the velocity dispersion profile The *top left* panel shows R_c (2 - 12), *top right* shows σ_0 (50 - 60), *bottom left* shows σ_1 (360 - 460) and the *bottom right* panel shows the variation in σ_2 (20 - 30). As basis of the curves the rounded results of the analysis of NGC1167 (lower limits) have been taken and the parameter under consideration has been altered with a stepsize of (upper limit - lower limits)/10. The black curve in each panel corresponds to the results of NGC1167.

derivative can be written in a nice way using the defined variable a.

$$\frac{\partial a}{\partial r} = \frac{r^3 \sin^2 i}{(2R_{\mathrm{mod}}^2)^2} - \frac{2r \sin^2 i}{2R_{\mathrm{mod}}^2} - \frac{2r \cos^2 i}{b} + \frac{r^2 \cos^2 i}{b^2}\,(2\kappa r + 2r) \tag{3.11}$$

Finally the logarithmic derivative of the radial velocity dispersion with respect to the radial coordinate can be expressed as

$$\frac{\partial \ln \sigma_r^2}{\partial \ln r} = \frac{r}{\sigma_r^2}\frac{\partial \sigma_r^2}{\partial r} = \frac{2r}{\sigma_r}\frac{\partial \sigma_r}{\partial r} = \frac{2r}{\sigma_r} \cdot \left(a^{-\frac{1}{2}} \frac{\partial \sigma_{\mathrm{obs}}}{\partial r} - \frac{a^{-\frac{3}{2}} \sigma_{\mathrm{obs}}}{2} \frac{\partial a}{\partial r} \right) \tag{3.12}$$

IDL Realisation

Since not every part of the observed galaxies produces enough signal to estimate the velocity at that point, not every point of the extracted profiles is useful for a fit and an option for excluding some points is necessary. The user can define a lower and an upper radial limit. Every point that does not satisfy this condition will be skipped during minimisation.

```
;##########################################################################
;
;sub-routine for selecting the points considered during minimisation
;
;INPUT:
;       radius      the x-axis of the raw data
;       Y           the y-axis of the raw data
;       error       the y-error of the raw data
;       moment      the considered moment
;       Rc          the core radius (necessary for fit to velocity dispersion)
;
;OUTPUT:
;       Yfit        the points on the y-axes considered during minimisation
;       radiusfit   the points on the x-axes considered during minimisation
;       errorfit    the errors on the y-axes considered during minimisation
;
;AUTHOR: Markus Arzt
;
;##########################################################################

pro selection,  radius, Y, error, moment,$
        Yfit, radiusfit, errorfit, Rc

  if moment EQ "phot" then yrange = [0.001,1.0] else $
  if moment EQ "v" then yrange = [0.0,max(Y)] else $
  if moment EQ "sigma" then yrange = [0.0,max(Y)]

  ploterror, radius, Y, error, psym=2, xrange=[0,40], YRange=yrange
  READ, cut_off_low, PROMPT='Enter x-value fit starts (greater than): '
  READ, cut_off_high, PROMPT='Enter x-value fit ends (lower than): '

  sel = where(radius GT cut_off_low)
  Y_low = Y[sel]
  radius_low = radius[sel]
  error_low = error[sel]

  sel = where(radius LT cut_off_high)
  Y_high = Y_low[sel]
  radius_high = radius_low[sel]
  error_high = error_low[sel]

  Yfit = Y_high
  radiusfit = radius_high
  errorfit = error_high

end
```

IDL has some built in tools for curve fitting, e.g., CURVEFIT (least square) or AMOEBA (downhill simplex), but these turned out to be not stable enough for some fits. A good and powerful alternative to these tools is MPFIT. MPFIT is a robust non-linear least square curve fitting tool (Markwardt, 2009). To fit the radial profiles in IDL using MPFIT, model functions for each of the profiles have to be defined. The function then returns the residuals of the real data and the model.

```
;###########################################################################
;
;functions for defining the fit function
;surface brightness:   f(x) = S1 * exp(-x/R1) + S2 * exp(-x/R2)
;velocity:             f(x) = v_inf * x / (Rc^2 + x^2)
;velocity dispersion:  f(x) = sigma_0 + sigma_1 * exp(-(x^2 + Rc^2)/sigma_2)
;
;PARAMETERS:
;      A[0]   S1   or    v_inf    or    sigma_0
;      A[1]   R1   or    Rc       or    sigma_1
;      A[2]   S2   or             or    sigma_2
;
;AUTHOR: Markus Arzt
;
;###########################################################################

function phot_func, A, XVAL=radius, YVAL=Y, ERRVAL=error

  model = A[0] * exp(-radius/A[1]) + A[2] * exp(-radius/A[3])
  resid = (Y - model)/error
  return, resid

end

function vel_func, A, XVAL=radius, YVAL=Y, ERRVAL=error

  model = A[0] * radius / sqrt(radius^2 + A[1]^2)
  resid = (Y - model)/error
  return, resid

end

function vel_disp_func, A, XVAL=radius, YVAL=Y, ERRVAL=error, RC=Rc

  model = A[0] + A[1] * exp(-sqrt(radius^2 + Rc^2)/A[2])
  resid = (Y - model)/error
  return, resid

end
```

A typical fitting sequence is shown below for the velocity profile. First the initial parameters and the parinfo structure, defining which parameters shall be limited and fixed during minimisation are filled with the appropriate values. Then the selection for the points considered during the fitting process is taken. Since IDL variables are passed by reference no structure is necessary here to return multiple arrays. The formal 1-σ error computed from the covariance matrix is saved in the PERROR variable.

```
    ;-----------------------------------------------------------------

    if moment EQ "v" then begin

      inipar = [100.0,5.0,0.0,0.0,0.0,0.0,0.0]
      parinfo.limited = [[1,1],[1,1],[0,0],[0,0],[0,0],[0,0],[0,0]]
      parinfo.fixed = [0,0,1,1,1,1,1]

      Y = k1
      error = erk1

      SELECTION, radius, Y, error, moment,$
        Yfit, radiusfit, errorfit

      result = MPFIT('vel_func',inipar,$
           FUNCTARGS={XVAL:radiusfit,YVAL:Yfit,ERRVAL:errorfit},$
           PARINFO=parinfo,PERROR=perror,/QUIET)

    endif

    ;-----------------------------------------------------------------
```

3.4 Separation of σ Contributions

As all ingredients for equation 1.18 are available at that point of the analysis, the true circular velocity of the stars and the gas can be obtained.

```
;##########################################################################
;
;function to calculate the true circular velocity
;
;INPUT:
;       r         the x-axis of the raw data
;       kappa     parameter for alignment of velocity ellipsoide
;       incl      inclination under which galaxy is viewed
;
;       S1        fitted parameter of surface brightness profile
;       R1        fitted parameter of surface brightness profile
;       S2        fitted parameter of surface brightness profile
;       R2        fitted parameter of surface brightness profile
;
;       Rc        fitted parameter of velocity profile
;       vinf      fitted parameter of velocity profile
;
;       sigma0    fitted parameter of velocity dispersion profile
;       sigma1    fitted parameter of velocity dispersion profile
;       sigma2    fitted parameter of velocity dispersion profile
;
;OUTPUT:
;       dlnbright         logarithmic derivative of surface brightness
;       dlnsigma_r_sq     logarithmic derivative of squared radial velocity dispersion
;       term3             core radius term of ADC
;       a                 conversion factor between radial and observed velocity
      dispersion
;
;AUTHOR: Markus Arzt
;
;##########################################################################

function v_circ, r, S1, R1, S2, R2,$
       Rc, vinf,$
       sigma0, sigma1, sigma2, kappa, incl,$
       dlnbright, dlnsigma_r_sq, term3, a

;--------------------------------------------------------------------------
;calculating the logarithmic derivative of the surface brightness

  bright = S1*exp(-r/R1) + S2*exp(-r/R2)
  dlnbright = -r/bright * (S1/R1*exp(-r/R1) + S2/R2*exp(-r/R2))

;--------------------------------------------------------------------------
;calculating the azimuthal velocity

  R_mod = sqrt(r^2 + Rc^2)
  v_phi = vinf * r / R_mod

;--------------------------------------------------------------------------
;calculating the logarithmic derivative of the squared radial velocity dispersion

  sigma_obs = sigma0 + sigma1 * exp(-R_mod/sigma2)
  b = kappa*(2*R_mod^2 - r^2) + r^2
  a = 1 - r^2*sin(incl)^2/(2 * R_mod^2) - r^2*cos(incl)^2/b
  sigma_r = sigma_obs * a^(-0.5)
  dsigma_obs = -sigma1*r/(sigma2*R_mod) * exp(-R_mod/sigma2)
  da = -2*r*sin(incl)^2/(2*R_mod^2) + r^3*sin(incl)^2/(4*R_mod^4) - 2*r*cos(incl)^2/
     b + r^2*cos(incl)^2*(2*kappa*r+2*r)/b^2
  dlnsigma_r_sq = 2*r/sigma_r * (dsigma_obs/sqrt(a) - sigma_obs*da/(2*a^(-3.d/2.d)))

;--------------------------------------------------------------------------
;finally calculating the true circular velocity and return result

  term3 = r^2/(2*R_mod^2) + kappa*r^2/b
  v_c = sqrt(v_phi^2 - sigma_r^2 * (dlnbright + dlnsigma_r_sq + term3))

  return, v_c

end
```

The ADC ($\sqrt{v_c^2 - \overline{v_\varphi}^2}$) for the stars is performed straight forward by inserting in equation 1.18, while for the ADC of the ionised gas turbulence will be neglected for the moment, i.e., $\sigma_{\text{turb}} = 0$, to obtain the ADC. In case the true circular velocity of the stars and the circular velocity of the ionised gas neglecting turbulence overlap, the assumption that turbulence is not important is correct and turbulence can be neglected. But based on the results of Weijmans et al. (2008) this should not be the case near the center.

The ADC of the ionised gas plotted against the radius should first increase, show a maximum which corresponds to turbulent motions near the galactic center, then decrease and settle down to a fixed value at higher radii, where turbulence does not play an important role anymore (see also Figure 4.5). As turbulence has no contribution to the velocity dispersion at large distances to the galactic center and the ADC can be approximated to be constant throughout the galaxy, the components of the velocity dispersion can be disentangled.
Adding quadratically the value of the ADC at large radii to the entire observed rotation curve of the ionised gas is equivalent to considering turbulent motions in the velocity dispersion. This corrected true circular velocity of the ionised gas should coincide with the true circular velocity of the stars, if the model for turbulence applied here is correct.

As the fixed ADC squared is equal to the underbraced term in equation 1.18 the equation can be re-arranged as a first order linear ordinary differantial equation of the form

$$A = B \cdot x + r\frac{\partial x}{\partial r} \quad \longrightarrow \quad x(r) = \frac{A}{B} + \text{const} \cdot r^{-B} \tag{3.13}$$

where A is the value of the fixed ADC squared, B the logarithmic derivative of the surface brightness plus the core radius terms in the ADC and $x = \sigma_r^2$. The constant can be determined under the assumption that the observed velocity dispersion at large radii is composed of gravitational influences and the minor influence of thermal motions, i.e., $x(\text{large } r)$ equals $\sigma_r^2(\sigma_{\text{obs}},\ \sigma_{\text{thermal}})$. Using equation 3.10 the observed velocity dispersion emerging solely from gravitational influences can be determined.
Now the velocity dispersions including only gravitional influences can be subtracted from the one including gravitational and turbulent influencens to quantify the turbulent motions. The next steps will depend on the resulting curves. If they show similiarities with small deviations, the idea is to look if these deviations are related to one or more, easy to observe properties, e.g., surface brightness.

Chapter 4

Results

4.1 Inclination

The data for the ellipticity and therefore the inclination was provided by J. Falcon Barroso's analysis of the photometry and is shown in Table 4.1.

Table 4.1: The ellipticities and inclinations for the complete sample.

Galaxy	ϵ	i [deg]
NGC1167	0.228 ± 0.015	39.47 ± 1.35
NGC2253	0.227 ± 0.023	39.38 ± 2.08
NGC6081	0.587 ± 0.023	65.61 ± 1.45
NGC6762	0.716 ± 0.004	73.50 ± 0.24
NGC7466	0.623 ± 0.005	67.85 ± 0.31
UGC05771	0.329 ± 0.026	47.86 ± 2.01
UGC08778	0.704 ± 0.005	72.78 ± 0.30
UGC09873	0.746 ± 0.005	75.29 ± 0.30
UGC10384	0.729 ± 0.004	74.28 ± 0.24
UGC11228	0.326 ± 0.029	47.62 ± 2.25

4.2 System Velocity

The system velocity of the stellar component of the galaxies was obtained as described in Section 3.1 and revealed no problems. Although the system velocity should be the same for different constituents of a galaxy, it is crucial to test whether that is really the case.
Even the simplest approach of taking the mean of all velocities, of spaxels with sufficient signal-to-noise ratio, showed that the system velocity for the gas data differs clearly from that of the stars. But plotting the velocity fields of the gas

Table 4.2: The system velocity for the stellar kinematic maps has been obtained by symmetrisation (see Section 3.2 and taking the mean of all binned spaxels, which provides automatically also the error. While the system velocities for the gas kinematic maps had to be measured by eye, with changes down to 5 km s^{-1}. But due to the unprecise approach, errors of up to 10 km s^{-1} should be expected.

Galaxy	$v_{\text{sys, stellar}}$ [km s^{-1}]	$v_{\text{sys, gas}}$ [km s^{-1}]			
		HaNII	HdHg	OII	OIII
NGC1167	4862.02 ± 0.74	4874	4863	4963	4910
NGC2253	3523.05 ± 0.45	3585	3534	3614	3537
NGC6081	5030.69 ± 1.52	5001	5179	5179	5001
NGC6762	2920.05 ± 0.71	2960	2917	2967	2905
NGC7466	7448.59 ± 1.47	7493	7554	7574	7477
UGC05771	7324.97 ± 1.15	7391	7442	7412	7381
UGC08778	3228.08 ± 1.02	3230	3306	3386	3229
UGC09873	5563.21 ± 3.41	5609	5646	5666	5587
UGC10384	4933.30 ± 1.16	4963	4989	5089	4957
UGC11228	5683.28 ± 0.74	5735	5761	5811	5768

data (see also Section A.2) showed that this approach is not satisfying for the H_δ/H_γ and Hα/[NII] cubes and clearly wrong for most of the [OII] and [OIII] cubes. The signal-to-noise ratio difference between reliable and untrustworthy spaxels is quite small which makes sigma clipping difficult and leads to an ineffective weighting and contamination with wrong measurements.
Unfortunately, due to the noisy data, there was no other possibility than visually analysing the kinematic maps and to manually determine the most fitting system velocities. The system velocity of the stellar maps acted as starting point and have been altered step by step, with a stepsize of 5 km s^{-1} until the map looked similiar to the stellar velocity map. For the determination of the system velocity the most important attributes were the position of the kinematic center relative to the overplotted isophotes and the symmetry properties predicted by theory. As the system velocity had been obtained by eye, a precise error determination was not possible.

The resulting kinematic maps for NGC1167 can be seen in Figure 4.1. The kinematic maps of the remaining sample can be seen in Section A.2 together with the velocity dispersion maps, while the value of the system velocities can be found in Table 4.2.

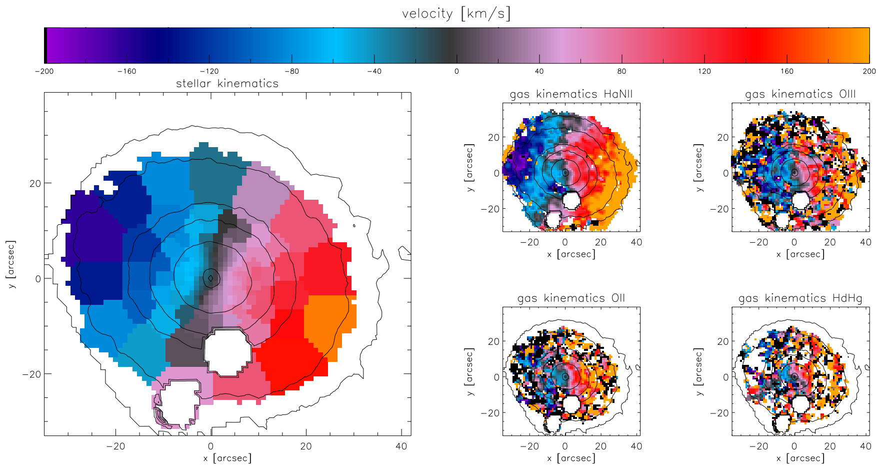

Figure 4.1: The *left panel* shows the Voronoi (Cappellari and Copin, 2003) binned kinematic velocity map of the stars of NGC1167, with a dynamic range from -200 to 200 km s^{-1} and overplotted with isophotes. The *right panel* shows the unbinned gas maps of the $H\alpha$+NII, OII, OIII and H_δ + H_γ lines, each separate with the same dynamic range and also overplotted with isophotes.

4.3 Position Angle

The direct approach described in Section 3.1 worked for all galaxies but NGC1167 and UG09873. In the latter case an inner circle with a radius of 4 arcsec and for NGC1167 a ring from 10 to 20 arcsec had been excluded from the analysis. Furthermore the number of steps were descreased to 60, to avoid local minima. The resulting position angle of NGC1167 can be seen in Figure 4.2.

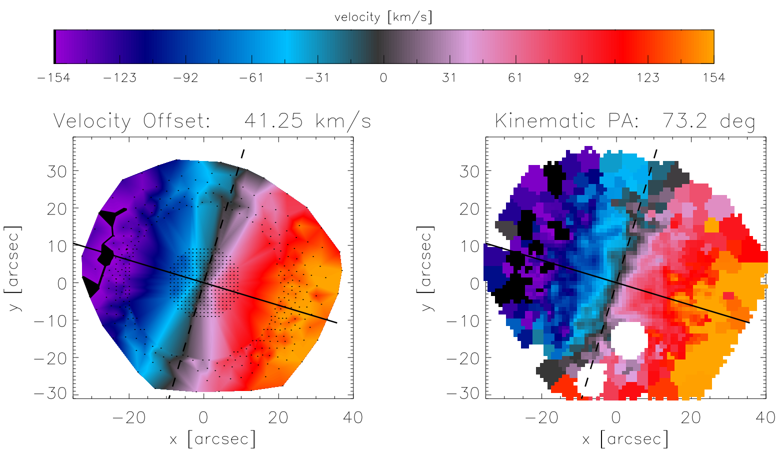

Figure 4.2: The kinematic position angle of NGC1167. Shown is in the *right panel* the binned data and the symmetrised velocity field in the *left panel*. The points considered during the analysis are indicated by the black dots in the left panel. The solid line is the velocity gradient and dashed line shows the parts without rotational velocity. Also shown is the velocity offset, which is the median of the differences between the binned data and the symmetrised velocity field.

The results for the other galaxies are given in Table 4.3 and the associated maps can be seen in Section A.2.

Table 4.3: The photometric position angles had been provided by J. Falcon Barroso. The kinematic position angles were extracted as described in Section 3.1.

Galaxy	photometric PA	kinematic PA
NGC1167	62.5 ± 3.1	73.22 ± 1.53
NGC2253	8.7 ± 2.2	118.33 ± 2.01
NGC6081	128.2 ± 0.6	124.35 ± 3.01
NGC6762	119.0 ± 0.5	119.33 ± 2.26
NGC7466	25.7 ± 0.5	29.58 ± 4.26
UGC05771	60.4 ± 2.2	48.13 ± 2.76
UGC08778	116.6 ± 0.3	112.81 ± 8.52
UGC09873	126.0 ± 0.2	128.14 ± 25.93
UGC10384	92.8 ± 0.7	93.76 ± 3.51
UGC11228	178.5 ± 1.6	177.99 ± 1.50

4.4 Extraction of Radial Profiles

The input parameters for the extraction of the radial profiles are the inclination, the kinematic, respectively for the surface brightness the photometric, position angle and the system velocity. The stellar kinematics were analysed without problems by using kinemetry. Only the cover parameter, which specifies the percentage of points necessary along an ellipse allowed, had to be varied between 0.5 and 0.75.
But the analysis of the gas datacubes revealed some problems. Table 4.4 shows for which lines kinemetry worked and how well. Based on this table the Hα + [NII] datacubes had been chosen for the further analysis. The other lines were ignored from this point on, to avoid introducing any systematic uncertainties. The fits to the kinematic profiles of NGC6081 can be seen in Figure 4.3 and the extracted curves, as well as their best fits of all galaxies are shown in Section A.4.

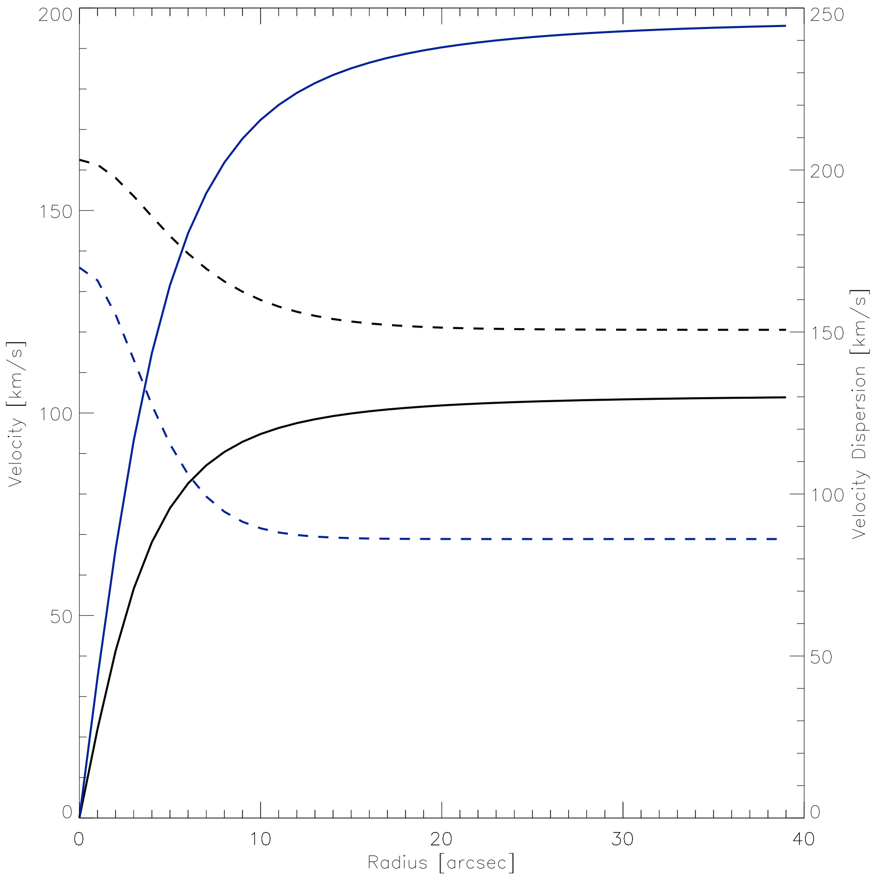

Figure 4.3: This plot shows the fits of the radial profiles of NGC6081. The solid lines are the velocity profiles of the stellar (black line) and the Hα + [NII] (blue line) datacubes, with the y-axis on the left hand side. While the dashed lines represent the velocity dispersion profiles of the stellar (black line) and the Hα + [NII] (blue line) datacubes, with the y-axis on the right hand side. This galaxy has been choosen, because it agrees best with the theoretical predictions that the gas rotates faster than the stars but shows less dispersion.

As for the MGE analysis the bands g, i, r, u and z were available in the SDSS database, it was not clear from the beginning which band to take for the analysis. After extraction of the radial profile for all bands and all galaxies it turned out that there is only little difference in the slope of the radial profile for a radius smaller than 40 arcsec for the different bands, as can be seen in Figure 4.4. But the galaxies emit the most in the z band and therefore the z band was the least contaminated with other objects in the field of view and the band selected to be analysed. As expected, MGE could handle elliptical galaxies easier than spiral galaxies, but even the ADC result of those was not suitable for further analysis.
For the first approach extracting the radial surface brightness of the stars using kinemetry, the flux of the binned data points had been used. But looking at the resulting ADC, the binning seemed to underestimate the flux for larger radii. Therefore the binned data was exchanged with the unbinned. For the gaseous

Table 4.4: Table on the performance of kinemetry in analysing the gas kinematics. There was no problem of divergence, when the field is smoothed prior to the analysis. ✓denotes an output suitable for further analysis, while (✓) means further analysis may be possible but not very reliable and x indicates useless output. The extracted profiles of the discarded lines can be seen in Section A.6

Galaxy	Hα + [NII]		H_δ + H_γ		[OII]		[OIII]	
	v	σ	v	σ	v	σ	v	σ
NGC1167	✓	✓	x	x	✓	(✓)	✓	(✓)
NGC2253	✓	✓	✓	(✓)	✓	(✓)	✓	x
NGC6081	✓	✓	x	x	x	(✓)	✓	(✓)
NGC6762	✓	✓	x	x	✓	(✓)	✓	✓
NGC7466	✓	✓	✓	✓	✓	(✓)	✓	(✓)
UGC05771	✓	✓	x	x	✓	(✓)	✓	✓
UGC08778	✓	✓	✓	✓	✓	x	✓	x
UGC09873	✓	✓	✓	x	(✓)	x	✓	x
UGC10384	✓	✓	✓	✓	✓	✓	✓	✓
UGC11228	✓	✓	x	x	x	(✓)	(✓)	(✓)

data only unbinned data was available. The neglected ADC results of the SDSS data and the binned CALIFA data can be seen in Section A.7.

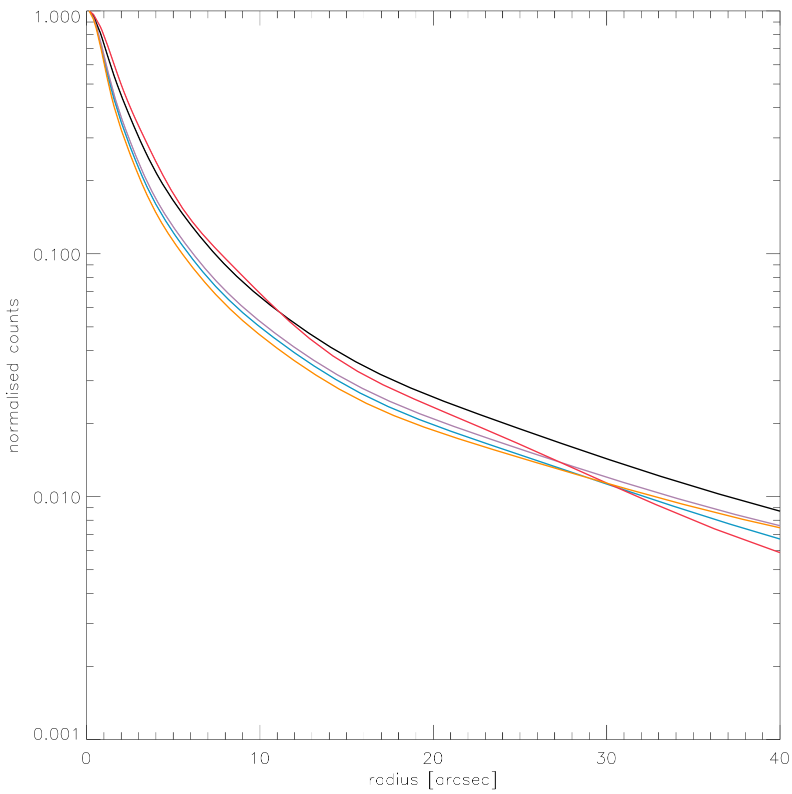

Figure 4.4: Radial surface brightness profiles of all SDSS band for NGC1167. All bands show almost exactly the same profile for radii smaller than 40 arcsec.

4.5 Separation of σ Contributions

The calculation of the true circular velocities of the stellar components was overall successful. But the ADC of 8 out of 10 galaxies showed tendencies of divergence towards large radii. Splitting up the ADC into its compoenents showed that the most important contribution arises, by far, from the logarithmic derivative of the surface brightness.
The ADCs of the gas kinematics almost never behaved as expected in Section 3.4 and the analysis of 4 out of 10 galaxies even produced negative values of the ADC. Of the remaining galaxies the ADC of 5 out of 6 showed no or just a small maximum at low radii and strong divergence with increasing radius. Only the ADC of NGC1167 behaved as expected. Therefore a reliable estimation of the gravitational contribution to the ADC and in succession the velocity dispersion was only possible for NGC1167. The results of the ADC for NGC1167 is shown in Figure 4.5, while the ADC analyses of the remaining galaxies of the sample can be seen in Section A.5.

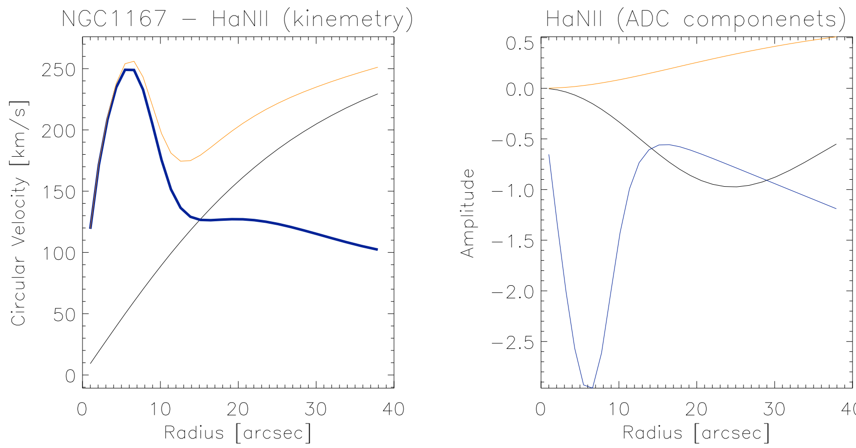

Figure 4.5: The figure shows the results of the ADC analysis of NGC1167. The *left panel* shows the azimuthal velocity (black line) together with the true circular velocity (orange line) and the amplitude of the ADC (blue line). The *right panel* shows the three components of the ADC. The major contribution results from the logarithmic derivative of the surface brightness (blue line). To a lesser extent the logarithmic derivative of the squared radial velocity disperion (black line) and a term including the core radius (orange line) influence the ADC.

When plotting the resulting true circular velocities for comparison, the mess becomes even more obvious. The true circular stellar velocities of 6 out of 10 galaxies show a bigger amplitude than the gaseous true circular velocities. This would make negative turbulent motions necessary to get these two curves to overlap, which is clearly unphysical. Unfortunately NGC1167 is one of these cases (as can be seen in Figure 4.6), which makes the results of this galaxy not plausible as well.
Nevertheless, the exercise to implent the separation of the different components of the velocity dispersion had been performed and the resulting graph of NGC1167 is shown in Figure 4.6. The gravitational component of the velocity dispersion takes over at a radius of about 13 arcsec (4.63 kpc) which is quite far from the kinematic center compared to the 8 arcsec (0.81 kpc) of the analysis

of Weijmans et al. (2008). But since the non turbulent true circular velocity of the gas and the true circular of the stars do not overlap in NCG1167 the result should not be taken seriously.

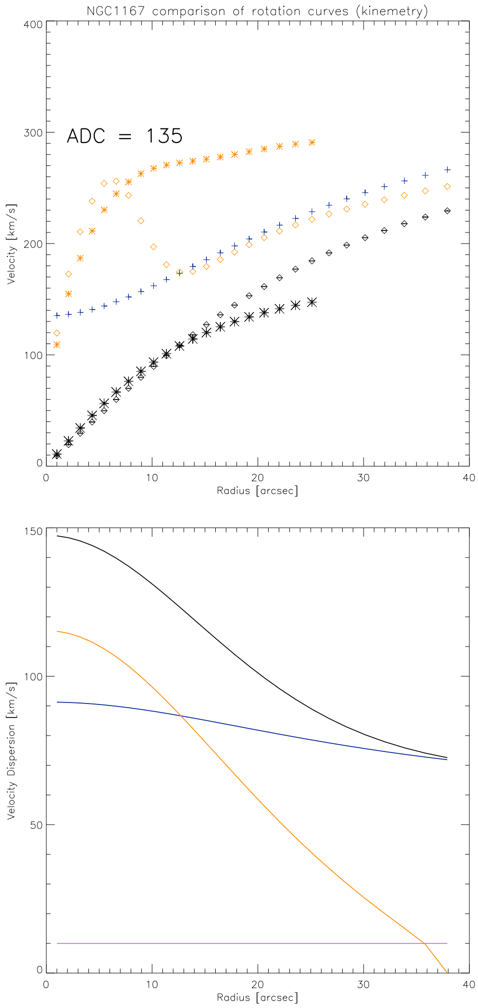

Figure 4.6: The *top panel* shows the comparison of the true circular velocites of the stars and the gas. The black curves show the azimuthal velocites and the orange curves the true circular velocities. To distinguish between the two kinematic tracers stars have been used for the stellar curves and diamonds for the gas curves. The blue crosses indicate the circular velocity of the gas resulting from the velocity dispersion neglecting turbulence.
The *bottom panel* shows the different disentangled components of the velocity dispersion of NGC1167. From top to bottom are shown the observed velocity dispersion (black line), the turbulent motions (orange line), the gravitational contribution (blue line) and the thermal motion (purple line).

Conclusion

On the basis of Weijmans et al. (2008) the idea was to expand their calculation of the stellar and gaseous true circular velocites to a broad variety of CALIFA galaxies. The goal was to test the feasibility of CALIFA data for this kind of analysis. The detailed data of the galaxies had been provided by the CALIFA team in form of separate datacubes for stellar and gaseous emission with two different resolution setups.
After determining the system velocity and kinematic position angle, it was possible to extract the radial profiles of the surface brightness, the azimuthal velocity and velocity dispersion using a fourier expansion along ellipses. To perform the ADC and obtain the true circular velocity these profiles were fitted, with parametric models.

After trying three different approaches concerning the stellar surface brightness, the unbinned data of the low resolution setup revealed itself as suited best for the ADC. For the other stellar profiles the binned data of the high resolution setup achieved the best results.
Concerning the gas emission, four different lines had been available. Unfortunately only unbinned data had been supplied, which revealed problems when using the high resolution lines, especially when extracting the velocity dispersion profiles. The Hα and [NII] could not be resolved due to the low resolution, but the extracted profiles from this line showed nevertheless the best quality.

The calculation of the true circular velocities of the stellar component of the galaxies seems to work. Although, at larger radii the true circular velocities of some galaxies show a tendency to start diverging, which could be explained by lowering the COVER parameter of kinemetry to allow worse sampled ellipses in the analysis.
But the analysis of the true circular velocities of the gas revealed bigger problems. The ADC did not behave as expected and even produced in some cases negative corrections to the azimuthal velocity especially at larger radii. Therefore it was rarely possible to identify a suitable value for the fixed ADC and subsequently to remove turbulence. But even in cases where the true circular velocities of the gas seemed fine, the comparison with the true circular velocity of the stars revealed chaos. There was no way to interpret the results in a physically meaningful way.

Since I re-calculated the paper of Weijmans et al. (2008) successfully and the results of the stellar kinematics seem correct, the problem must arise from the low signal-to-noise ratio of the input data of the gas. By the time this data is available in a binned version this analysis could be revisited to quantify turbulent motions for different morphological types.

Bibliography

Ade, P. et al. Planck 2013 results. xvi. cosmological parameters. *Astronomy and Astrophysics*, 2014.

Bender, R. and Moellenhoff, C. Morphological analysis of massive early-type galaxies in the virgo cluster. *Astronomy and Astrophysics*, 177:71–83, 1987.

Binney, J. and Tremaine, S. *Galactic dynamics*. Princeton University Press, 1987.

Bronstein, I. et al. *Taschenbuch der Mathematik*. Wissenschaftlicher Verlag Harri Deutsch GmbH, 2008.

Cappellari, M. Efficient multi-gaussian expansion of galaxies. *Monthly Notices of the Royal Astronomical Society*, 333:400–410, 2002.

Cappellari, M. Measuring the inclination and mass-to-light ratio of axisymmetric galaxies via anisotropic jeans models of stellar kinematics. *Monthly Notices of the Royal Astronomical Society*, 390:71–86, 2008.

Cappellari, M. and Copin, Y. Adaptive spatial binning of integral-field spectroscopic data using voronoi tessellations. *Monthly Notices of the Royal Astronomical Society*, 342:345–354, 2003.

de Zeeuw, T. Schwarzschild's method for constructing galaxy models, 2012. URL www.noao.edu/meetings/m31/files/Martin-Dynamics.pdf.

Emsellem, E. et al. The atlas3d project - iii. a census of the stellar angular momentum within the effective radius of early-type galaxies: unveiling the distribution of fast and slow rotators. *Monthly Notices of the Royal Astronomical Society*, 414:888–912, 2011.

Evans, N. and de Zeeuw, P. Observable properties of the power-law galaxies. *Monthly Notices of the Royal Astronomical Society*, 271:202–222, 1994.

Garcia-Gomez, C., Athanassoula, E., and Barbera, C. Analysis of the distribution of hii regions in external galaxies. iv. the new galaxy sample. position and inclination angles. *Astronomy and Astrophysics*, 389:68–83, 2002.

Garcia-Lorenzo, B. et al. Ionized gas kinematics of galaxies in the califa survey. i. *Astronomy and Astrophysics*, in preparation, 2014.

Golubov, O. and Just, A. Asymmetric drift and rotation curve from rave and segue data. *American Astronomical Society*, 2012.

Husemann, B. et al. Califa, the calar alto legacy integral field area survey: Ii. first public data release. *Astronomy and Astrophysics*, 549:87H, 2013.

Jedrzejewski, R. Ccd surface photometry of elliptical galaxies - i. observations, reduction and results. *Monthly Notices of the Royal Astronomical Society*, 226:747–768, 1987.

Krajnovic, D. et al. Kinemetry: a generalization of photometry to the higher moments of the line-of-sight velocity distribution. *Monthly Notices of the Royal Astronomical Society*, 366:787–802, 2005.

Markwardt, C. Non-linear least-squares fitting in idl with mpfit. *Astronomical Data Analysis Software and Systems XVIII*, 411:251, 2009.

McKee, C. and Ostriker, J. A theory of the interstellar medium - three components regulated by supernova explosions in an inhomogeneous substrate. *Astrophysical Journal*, 218:148–169, 1977.

Mo, H., van den Bosch, F., and White, S. *Galaxy Formation and Evolution*. Cambridge University Press, 1. edition, 2013.

Richstone, D. Scale-free models of galaxies. ii - a complete survey of orbits. *Astronomy and Astrophysics*, 252:496R, 1982.

Schwarzschild, M. A numerical model for a triaxial stellar system in dynamical equilibrium. *The Astrophysical Journal*, 232:236–247, 1979.

SDSS, 2013. URL www.sdss.org.

van den Bosch, R. and de Zeeuw, P. Estimating black hole masses in triaxial galaxies. *Monthly Notices of the Royal Astronomical Society*, 401:1770–1780, 2012.

Verdoes-Kleijn, G. et al. What drives the central velocity dispersion in nearby early-type galaxies? *Carnegie Observatories Astrophysics Series*, Edited by L. C. Ho, 2004.

Ward, D. Methods for determining galactic inclination, 2000. URL eo.ucar.edu/staff/dward/sao/spirals/methods.htm.

Weijmans, A. et al. The shape of the dark matter halo in the early-type galaxy ngc 2974. *Monthly Notices of the Royal Astronomical Society*, 383:1343–1358, 2008.

Weisstein, E. Integral of motion, 2013a. URL mathworld.wolfram.com/IntegralofMotion.html.

Weisstein, E. Leibniz integral rule, 2013b. URL mathworld.wolfram.com/LeibnizIntegralRule.html.

Appendix A

Appendix

A.1 Photometric Maps

Figure A.1: The *left image* shows NGC1167 and the *right image* NGC2253. The pictures are taken from the SDSS data base (SDSS).

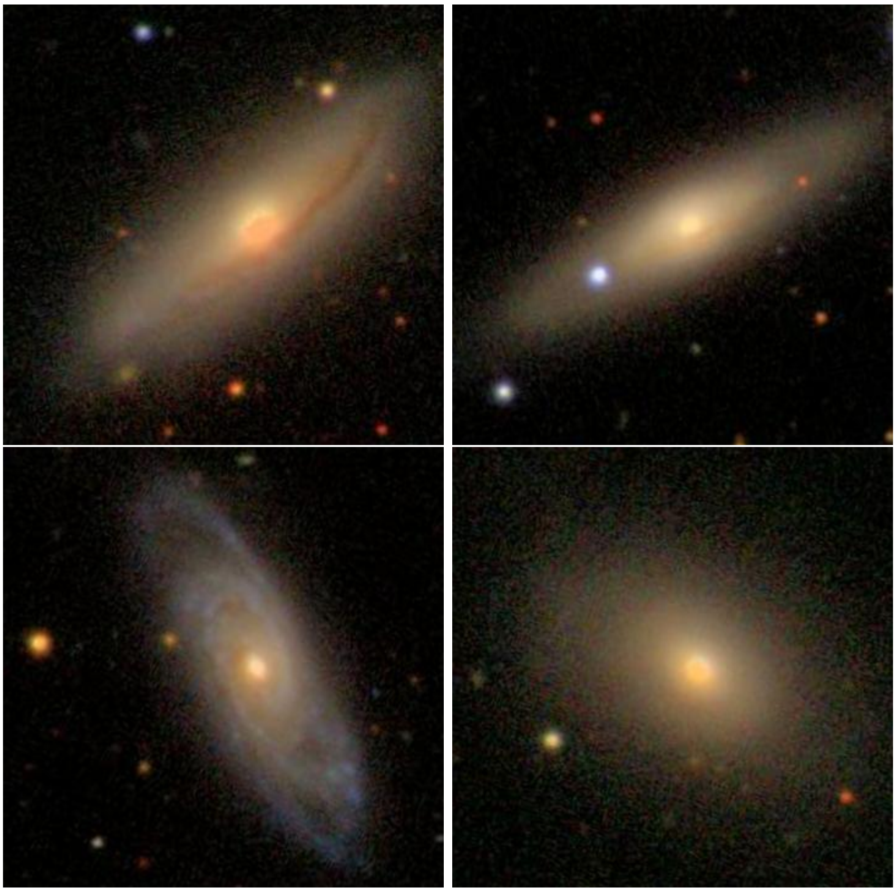

Figure A.2: The *top left image* shows NGC6081, the *top right image* NGC6762, the *bottom left image* NGC7466 and the *bottom right image* UGC05771. The pictures are taken from the SDSS data base (SDSS).

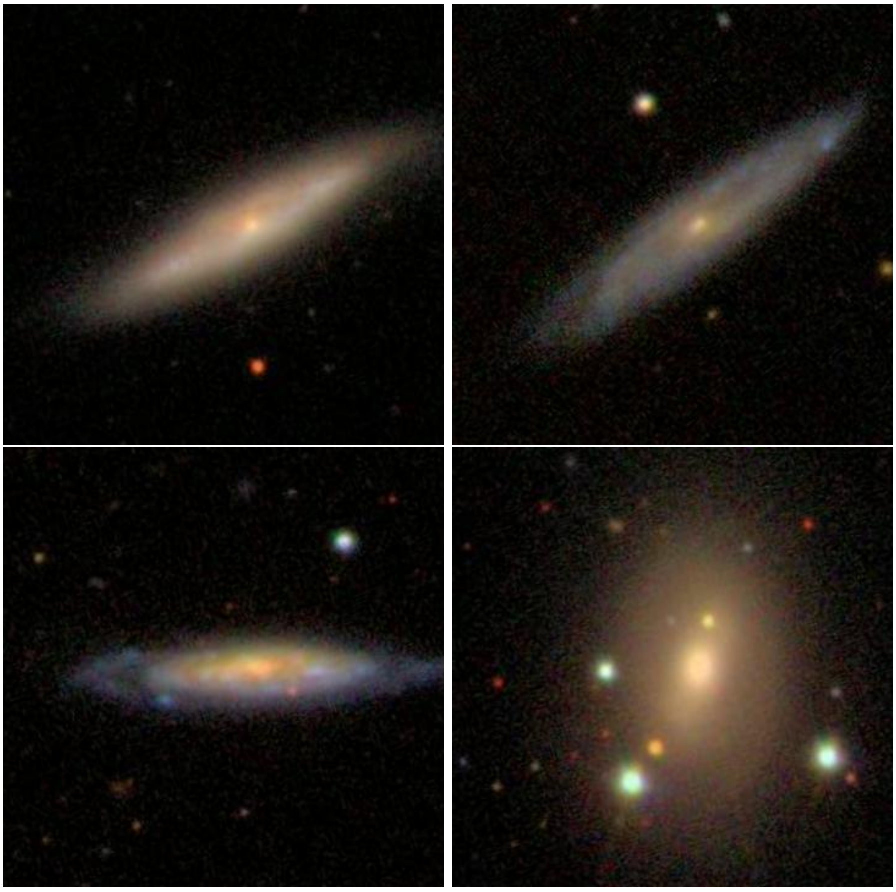

Figure A.3: The *top left image* shows UGC08778, the *top right image* UGC09873, the *bottom left image* UGC10384 and the *bottom right image* UGC11228. The pictures are taken from the SDSS data base (SDSS).

A.2 Kinematic Maps

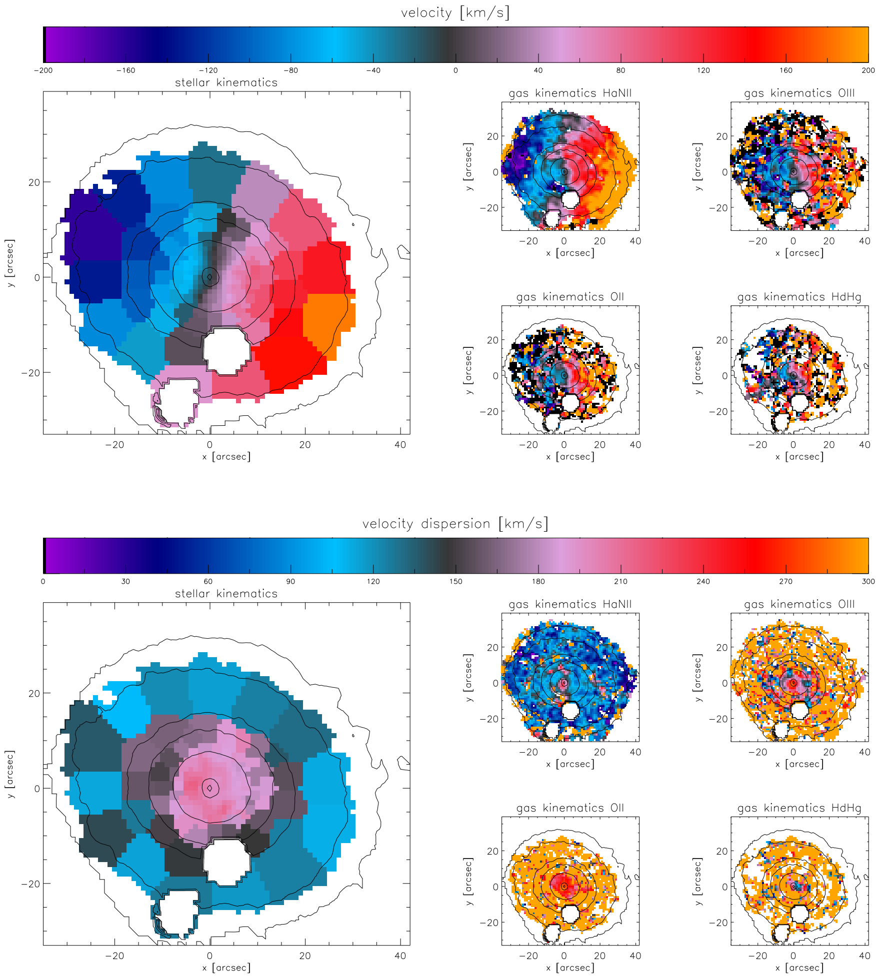

Figure A.4: The *upper panel* shows the Voronoi (Cappellari and Copin, 2003) binned kinematic velocity maps of the stellar (left) and unbinned gaseous (right) of the Hα+NII, OII, OIII and H_δ + H_γ lines, each separate, of NGC1167 overplotted with isophots with a dynamic range from -200 to 200 km s^{-1}. The *lower panel* shows the same but for the velocity dispersion and a dynamic range from 0 to 300 km s^{-1}.

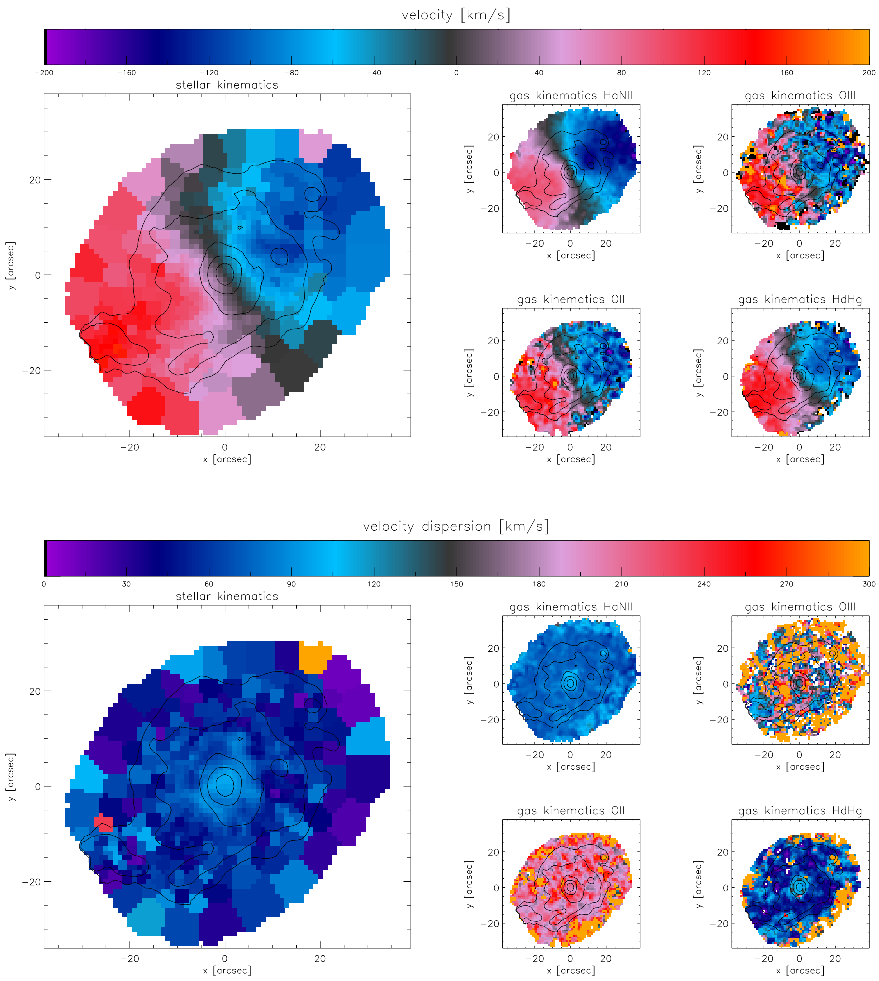

Figure A.5: The *upper panel* shows the Voronoi (Cappellari and Copin, 2003) binned kinematic velocity maps of the stellar (left) and unbinned gaseous (right) of the Hα+NII, OII, OIII and H_δ + H_γ lines, each separate, of NGC2253 overplotted with isophots with a dynamic range from -200 to 200 km s^{-1}. The *lower panel* shows the same but for the velocity dispersion and a dynamic range from 0 to 300 km s^{-1}.

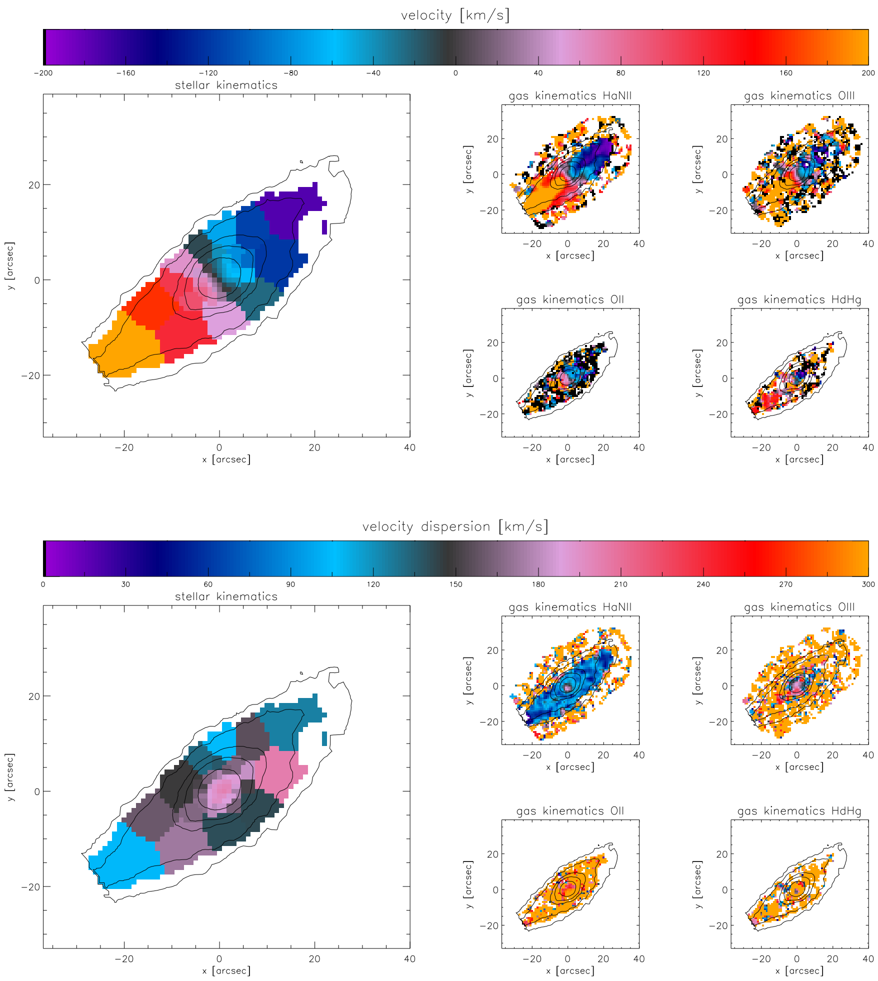

Figure A.6: The *upper panel* shows the Voronoi (Cappellari and Copin, 2003) binned kinematic velocity maps of the stellar (left) and unbinned gaseous (right) of the Hα+NII, OII, OIII and H_δ + H_γ lines, each separate, of NGC6081 overplotted with isophots with a dynamic range from -200 to 200 km s^{-1}. The *lower panel* shows the same but for the velocity dispersion and a dynamic range from 0 to 300 km s^{-1}.

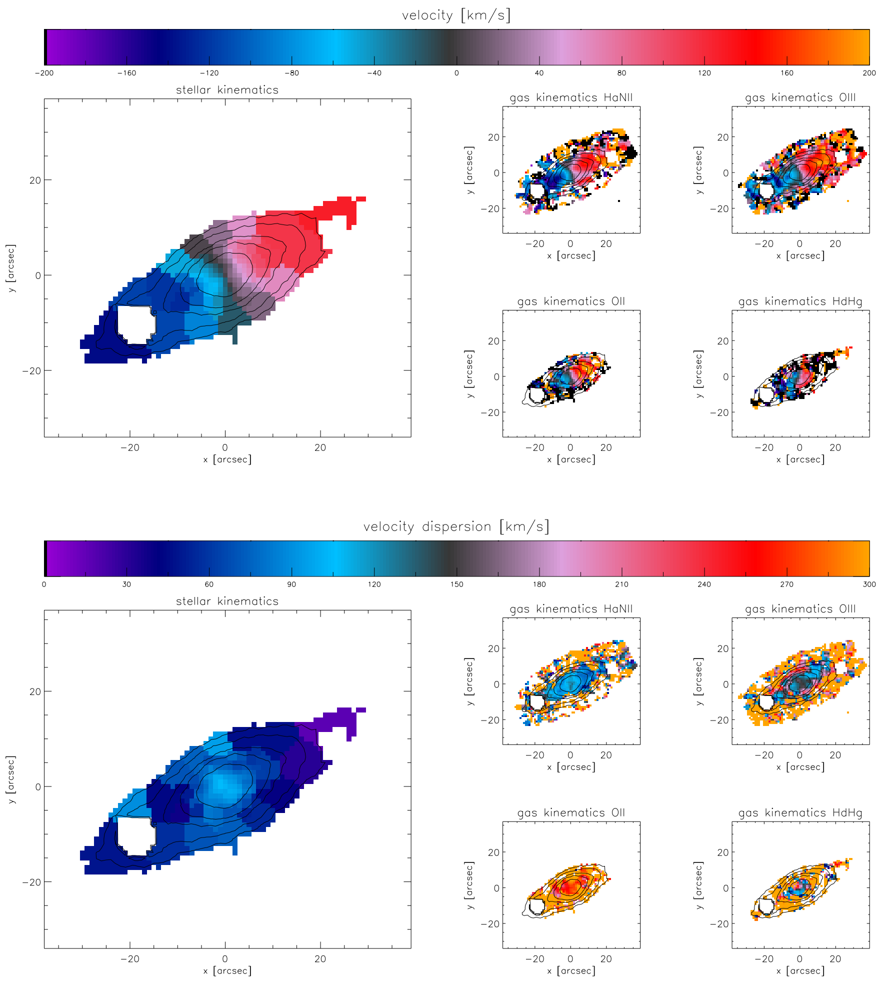

Figure A.7: The *upper panel* shows the Voronoi (Cappellari and Copin, 2003) binned kinematic velocity maps of the stellar (left) and unbinned gaseous (right) of the Hα+NII, OII, OIII and H_δ + H_γ lines, each separate, of NGC6762 overplotted with isophots with a dynamic range from -200 to 200 km s^{-1}. The *lower panel* shows the same but for the velocity dispersion and a dynamic range from 0 to 300 km s^{-1}.

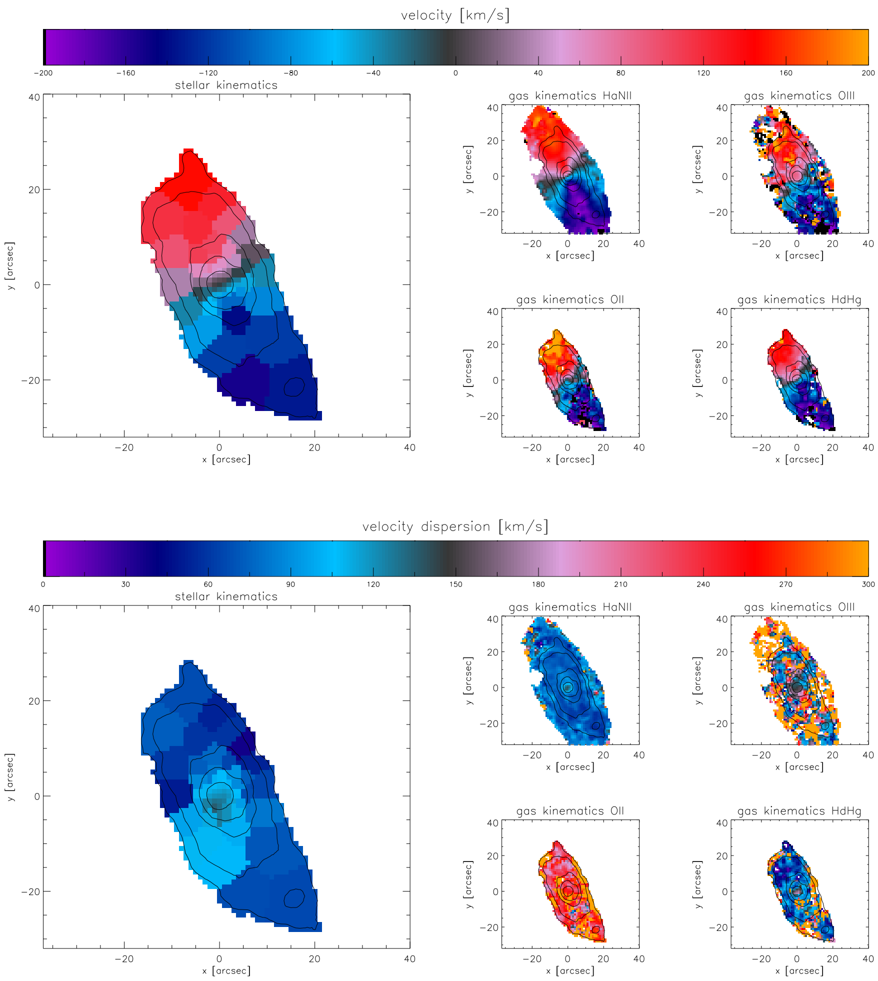

Figure A.8: The *upper panel* shows the Voronoi (Cappellari and Copin, 2003) binned kinematic velocity maps of the stellar (left) and unbinned gaseous (right) of the Hα+NII, OII, OIII and H_δ + H_γ lines, each separate, of NGC7466 overplotted with isophots with a dynamic range from -200 to 200 km s^{-1}. The *lower panel* shows the same but for the velocity dispersion and a dynamic range from 0 to 300 km s^{-1}.

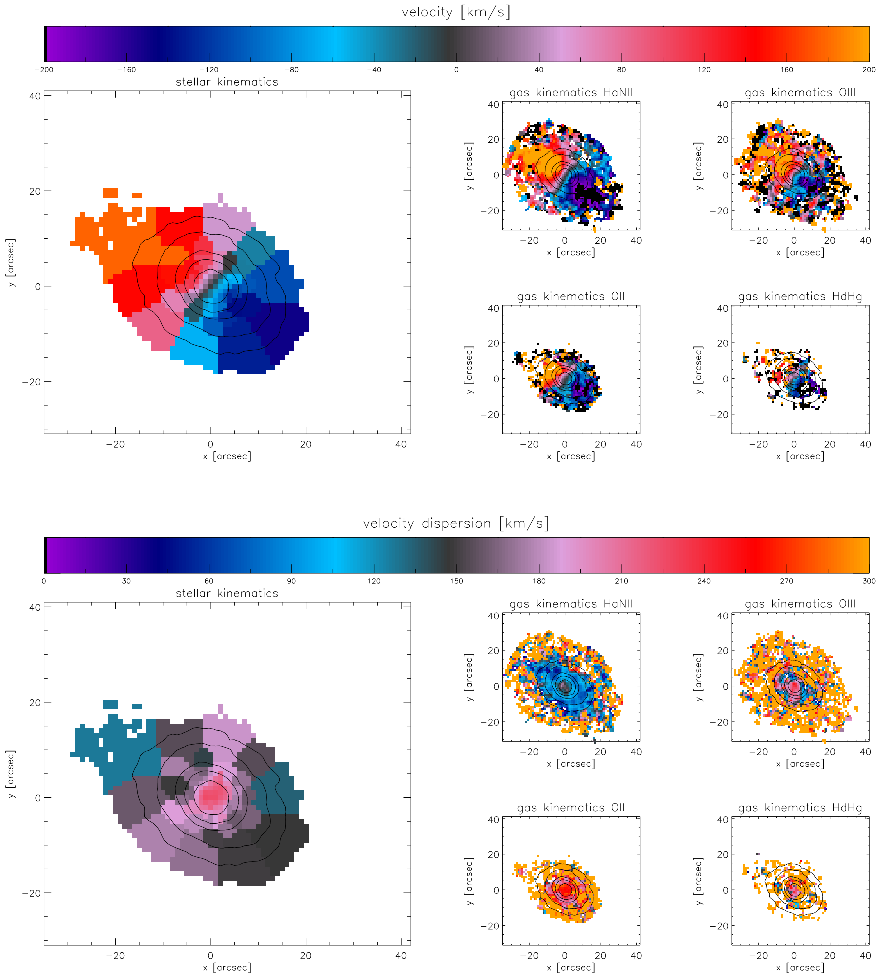

Figure A.9: The *upper panel* shows the Voronoi (Cappellari and Copin, 2003) binned kinematic velocity maps of the stellar (left) and unbinned gaseous (right) of the Hα+NII, OII, OIII and H$_\delta$ + H$_\gamma$ lines, each separate, of UGC05771 overplotted with isophots with a dynamic range from -200 to 200 km s^{-1}. The *lower panel* shows the same but for the velocity dispersion and a dynamic range from 0 to 300 km s^{-1}.

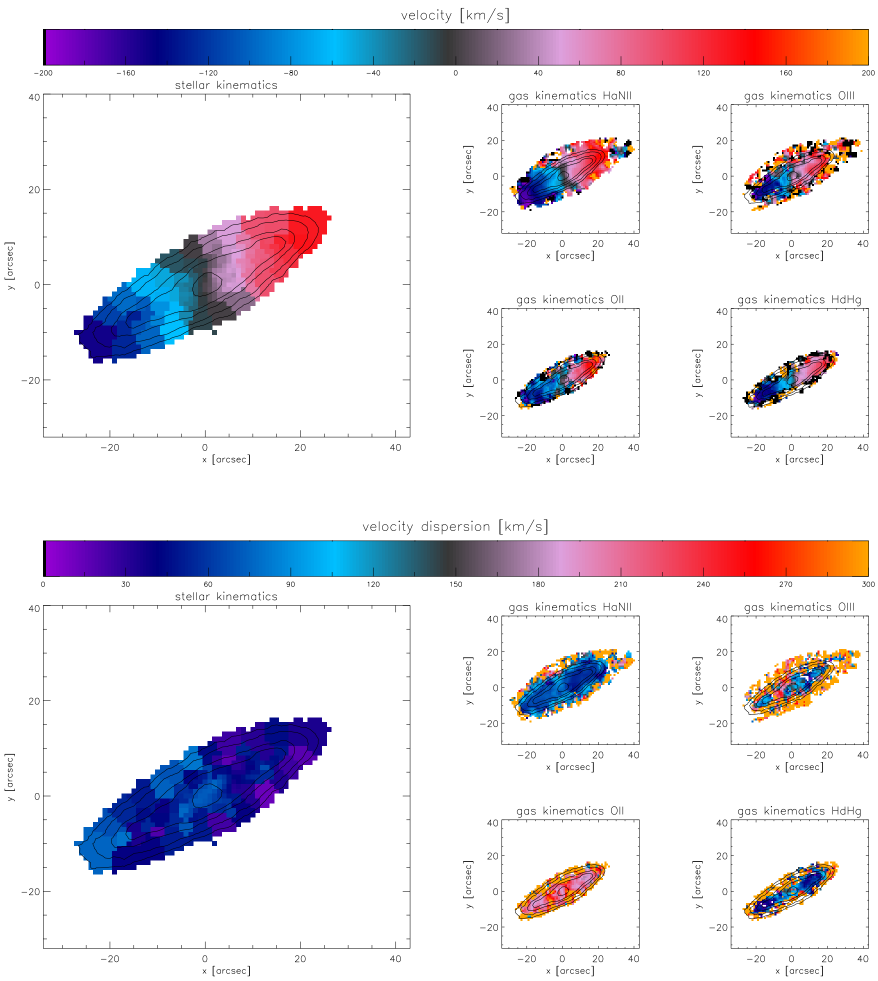

Figure A.10: The *upper panel* shows the Voronoi (Cappellari and Copin, 2003) binned kinematic velocity maps of the stellar (left) and unbinned gaseous (right) of the Hα+NII, OII, OIII and H$_\delta$ + H$_\gamma$ lines, each separate, of UGC08778 overplotted with isophots with a dynamic range from -200 to 200 km s^{-1}. The *lower panel* shows the same but for the velocity dispersion and a dynamic range from 0 to 300 km s^{-1}.

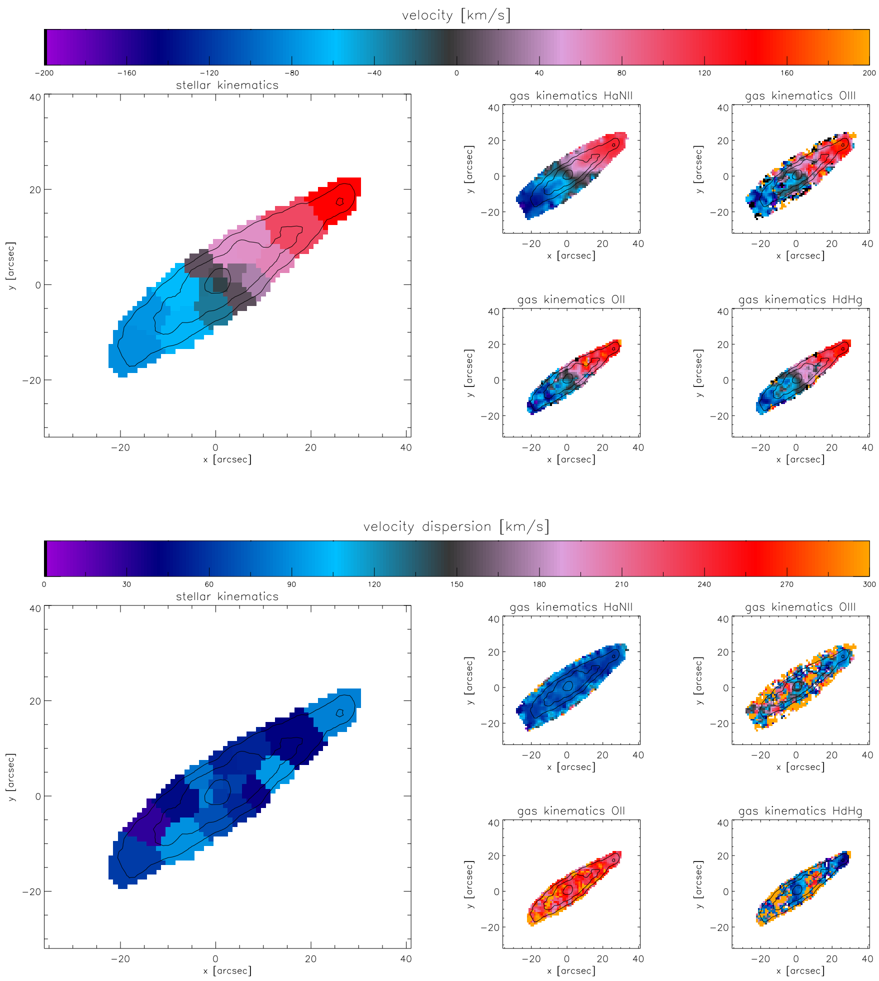

Figure A.11: The *upper panel* shows the Voronoi (Cappellari and Copin, 2003) binned kinematic velocity maps of the stellar (left) and unbinned gaseous (right) of the Hα+NII, OII, OIII and H$_\delta$ + H$_\gamma$ lines, each separate, of UGC09873 overplotted with isophots with a dynamic range from -200 to 200 km s^{-1}. The *lower panel* shows the same but for the velocity dispersion and a dynamic range from 0 to 300 km s^{-1}.

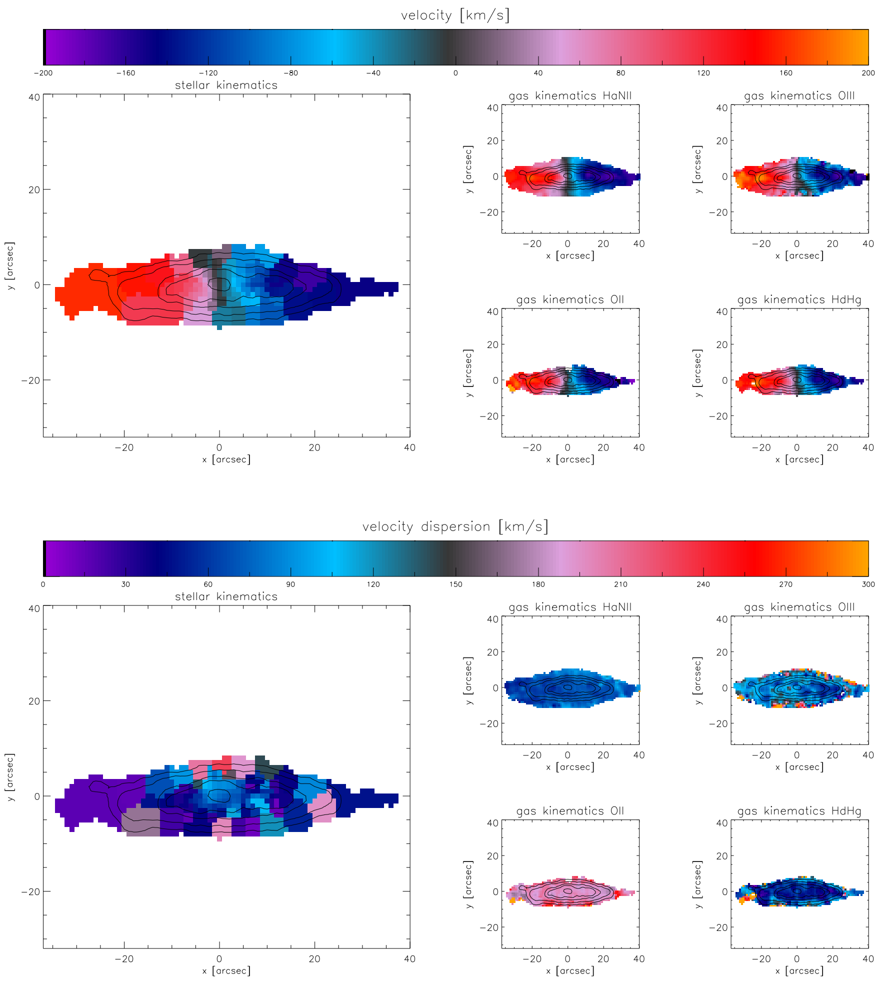

Figure A.12: The *upper panel* shows the Voronoi (Cappellari and Copin, 2003) binned kinematic velocity maps of the stellar (left) and unbinned gaseous (right) of the Hα+NII, OII, OIII and H$_\delta$ + H$_\gamma$ lines, each separate, of UGC10384 overplotted with isophots with a dynamic range from -200 to 200 km s^{-1}. The *lower panel* shows the same but for the velocity dispersion and a dynamic range from 0 to 300 km s^{-1}.

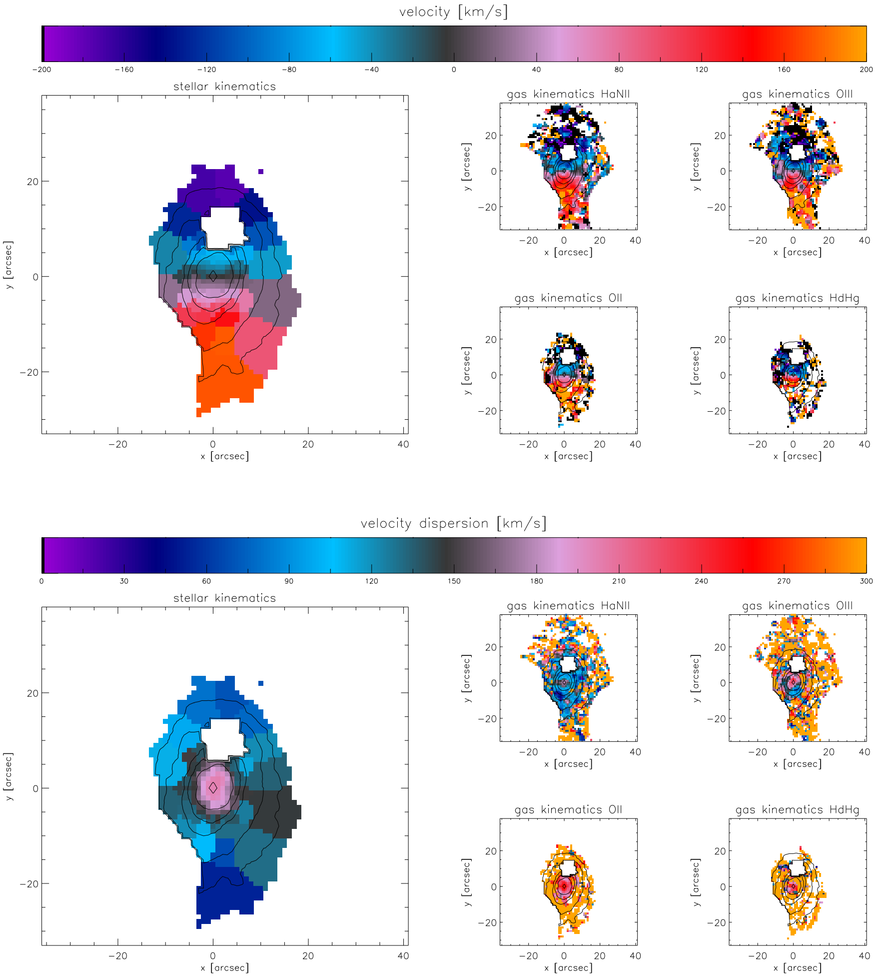

Figure A.13: The *upper panel* shows the Voronoi (Cappellari and Copin, 2003) binned kinematic velocity maps of the stellar (left) and unbinned gaseous (right) of the Hα+NII, OII, OIII and H$_\delta$ + H$_\gamma$ lines, each separate, of UGC11228 overplotted with isophots with a dynamic range from -200 to 200 km s^{-1}. The *lower panel* shows the same but for the velocity dispersion and a dynamic range from 0 to 300 km s^{-1}.

A.3 Position Angle

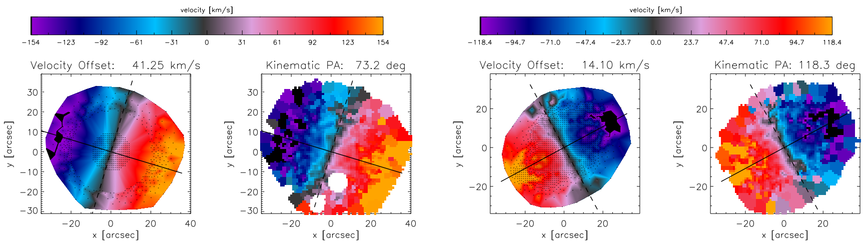

Figure A.14: The kinematic position angle of NGC1167 left panel and NGC2253 right panel. Shown is the binned data (right panel) as well as the symmetrised velocity field (left panel) with the considered points in the galaxy (black dots left panel). The solid lines are the velocity gradients and dashed lines show the parts without rotational velocity. The velocity offset is the median of the differences between the binned data and the symmetrised velocity field.

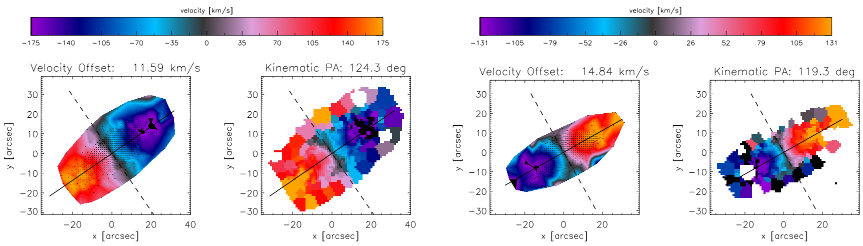

Figure A.15: The kinematic position angle of NGC6081 left panel and NGC6762 right panel. Shown is the binned data (right panel) as well as the symmetrised velocity field (left panel) with the considered points in the galaxy (black dots left panel). The solid lines are the velocity gradients and dashed lines show the parts without rotational velocity. The velocity offset is the median of the differences between the binned data and the symmetrised velocity field.

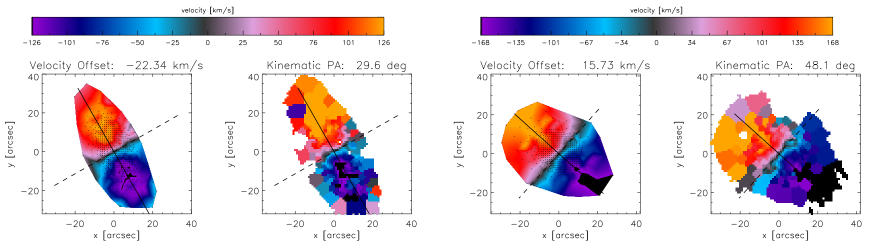

Figure A.16: The kinematic position angle of NGC7466 left panel and UGC05771 right panel. Shown is the binned data (right panel) as well as the symmetrised velocity field (left panel) with the considered points in the galaxy (black dots left panel). The solid lines are the velocity gradients and dashed lines show the parts without rotational velocity. The velocity offset is the median of the differences between the binned data and the symmetrised velocity field.

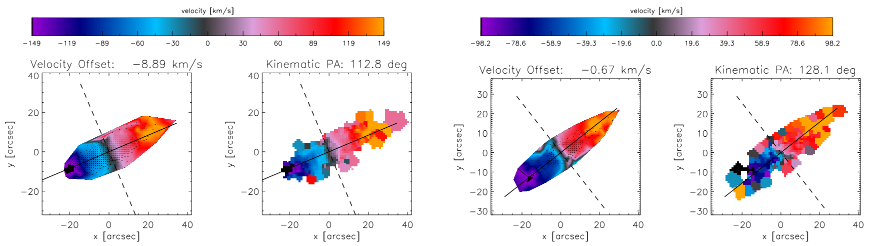

Figure A.17: The kinematic position angle of UGC08778 left panel and UGC09873 right panel. Shown is the binned data (right panel) as well as the symmetrised velocity field (left panel) with the considered points in the galaxy (black dots left panel). The solid lines are the velocity gradients and dashed lines show the parts without rotational velocity. The velocity offset is the median of the differences between the binned data and the symmetrised velocity field.

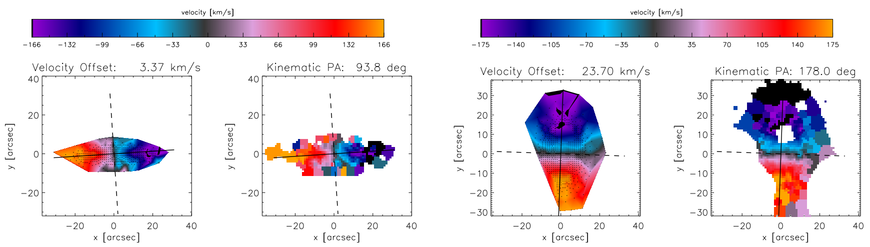

Figure A.18: The kinematic position angle of UGC10384 left panel and UGC11228 right panel. Shown is the binned data (right panel) as well as the symmetrised velocity field (left panel) with the considered points in the galaxy (black dots left panel). The solid lines are the velocity gradients and dashed lines show the parts without rotational velocity. The velocity offset is the median of the differences between the binned data and the symmetrised velocity field.

A.4 Fitted Profiles

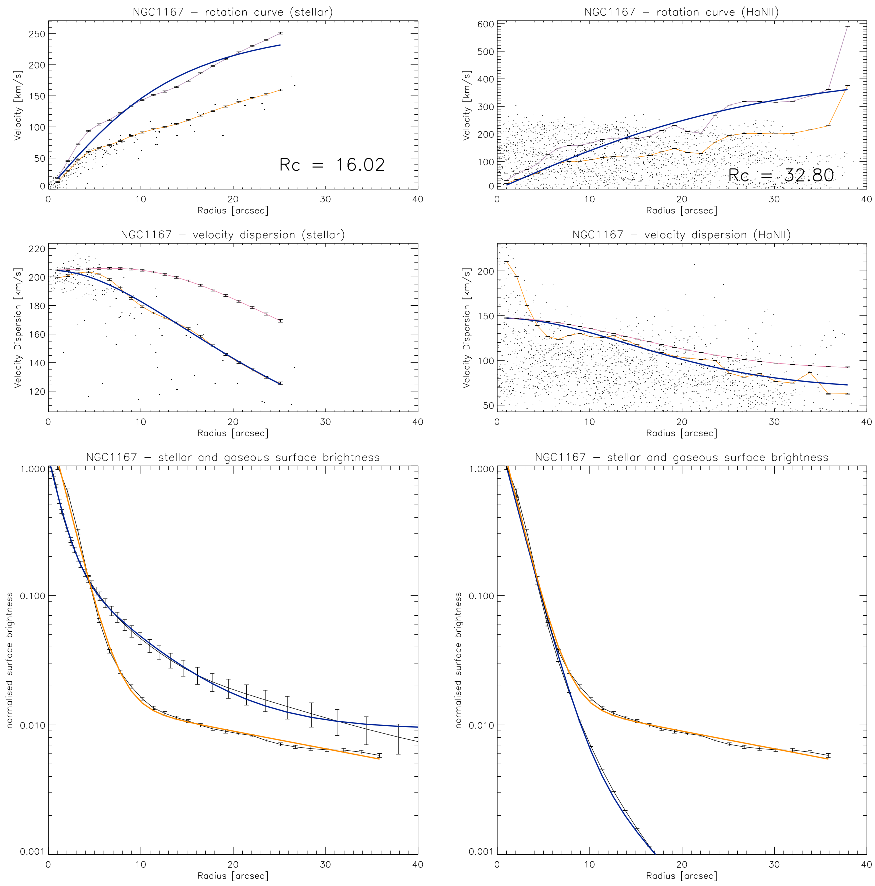

Figure A.19: This figure shows the radial profiles of NGC1167.
The *upper left panel* shows the velocity profile extracted with kinemetry (orange line), as well as the inclination corrected one (purple line) together with its best power law fit. The black dots represent the input data of kinemetry. Given is also the core radius of the fit in the lower right corner. The *upper right panel* shows the same but for the gas data.
The *middle panel* shows the observed velocity dispersion (orange line) with its single exponential fit and the from the fit obtained radial velocity dispersion σ_r (purple line). The *middle right panel* shows the same but for the gas data.
The *lower left panel* shows the radial surface brightness profile of extracted with MGE together with its best triple exponential fit (blue line) and the surface brightness of the gas extracted with kinemetry together with its best fit (orange line). In the *lower right panel* the MGE output is exchanged with the kinemetry output of the binned stellar flux analysis.

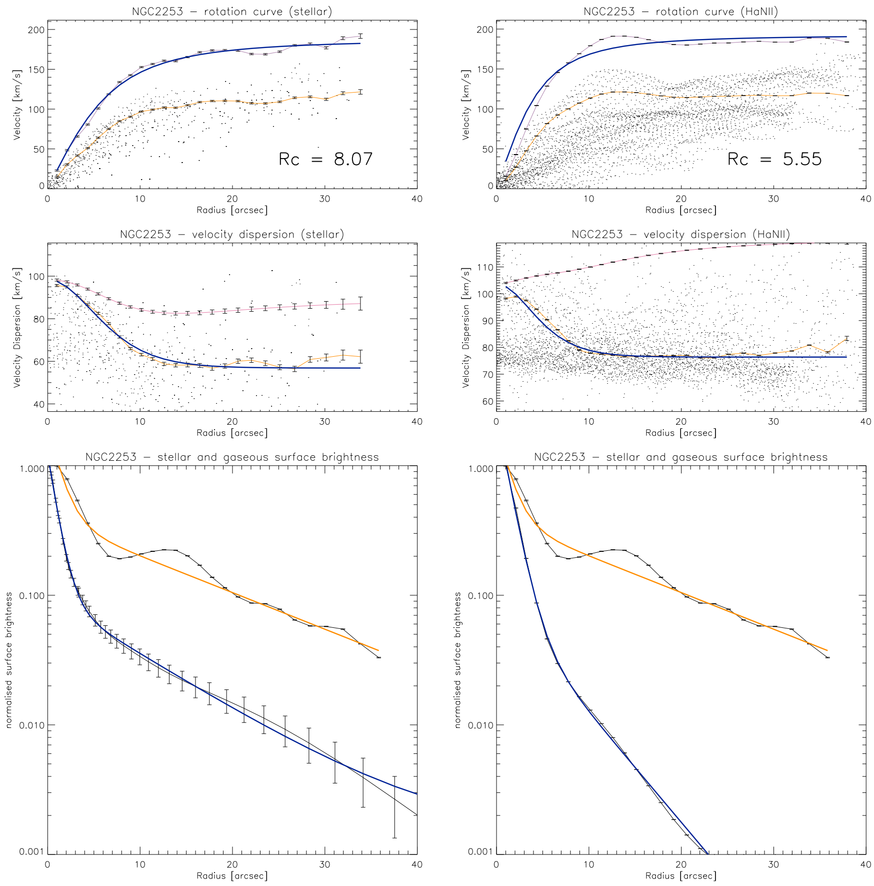

Figure A.20: This figure shows the radial profiles of NGC2253.
The *upper left panel* shows the velocity profile extracted with kinemetry (orange line), as well as the inclination corrected one (purple line) together with its best power law fit. The black dots represent the input data of kinemetry. Given is also the core radius of the fit in the lower right corner. The *upper right panel* shows the same but for the gas data.
The *middle panel* shows the observed velocity dispersion (orange line) with its single exponential fit and the from the fit obtained radial velocity dispersion σ_r (purple line). The *middle right panel* shows the same but for the gas data.
The *lower left panel* shows the radial surface brightness profile of extracted with MGE together with its best triple exponential fit (blue line) and the surface brightness of the gas extracted with kinemetry together with its best fit (orange line). In the *lower right panel* the MGE output is exchanged with the kinemetry output of the binned stellar flux analysis.

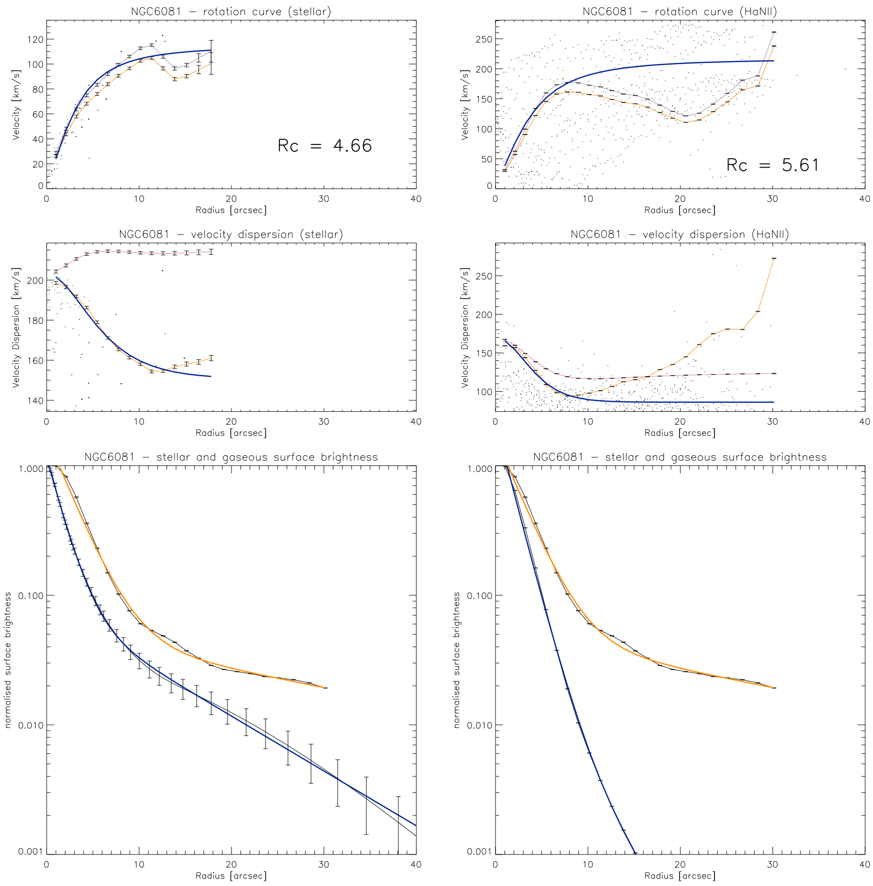

Figure A.21: This figure shows the radial profiles of NGC6081.
The *upper left panel* shows the velocity profile extracted with kinemetry (orange line), as well as the inclination corrected one (purple line) together with its best power law fit. The black dots represent the input data of kinemetry. Given is also the core radius of the fit in the lower right corner. The *upper right panel* shows the same but for the gas data.
The *middle panel* shows the observed velocity dispersion (orange line) with its single exponential fit and the from the fit obtained radial velocity dispersion σ_r (purple line). The *middle right panel* shows the same but for the gas data.
The *lower left panel* shows the radial surface brightness profile of extracted with MGE together with its best triple exponential fit (blue line) and the surface brightness of the gas extracted with kinemetry together with its best fit (orange line). In the *lower right panel* the MGE output is exchanged with the kinemetry output of the binned stellar flux analysis.

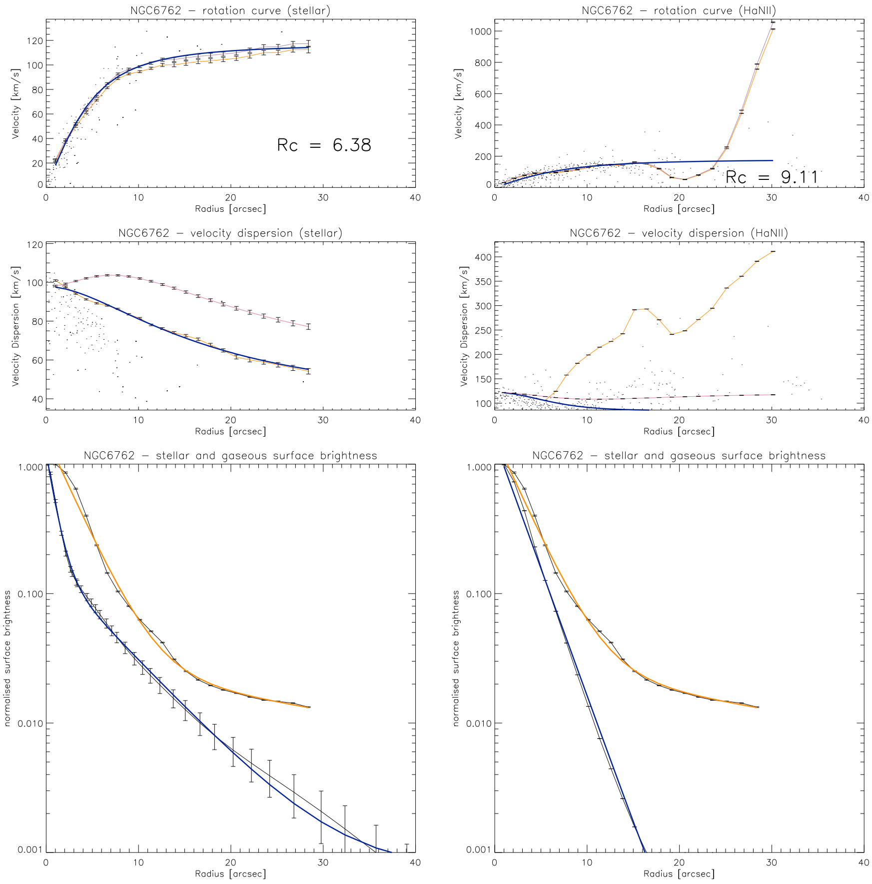

Figure A.22: This figure shows the radial profiles of NGC6762.
The *upper left panel* shows the velocity profile extracted with kinemetry (orange line), as well as the inclination corrected one (purple line) together with its best power law fit. The black dots represent the input data of kinemetry. Given is also the core radius of the fit in the lower right corner. The *upper right panel* shows the same but for the gas data.
The *middle panel* shows the observed velocity dispersion (orange line) with its single exponential fit and the from the fit obtained radial velocity dispersion σ_r (purple line). The *middle right panel* shows the same but for the gas data.
The *lower left panel* shows the radial surface brightness profile of extracted with MGE together with its best triple exponential fit (blue line) and the surface brightness of the gas extracted with kinemetry together with its best fit (orange line). In the *lower right panel* the MGE output is exchanged with the kinemetry output of the binned stellar flux analysis.

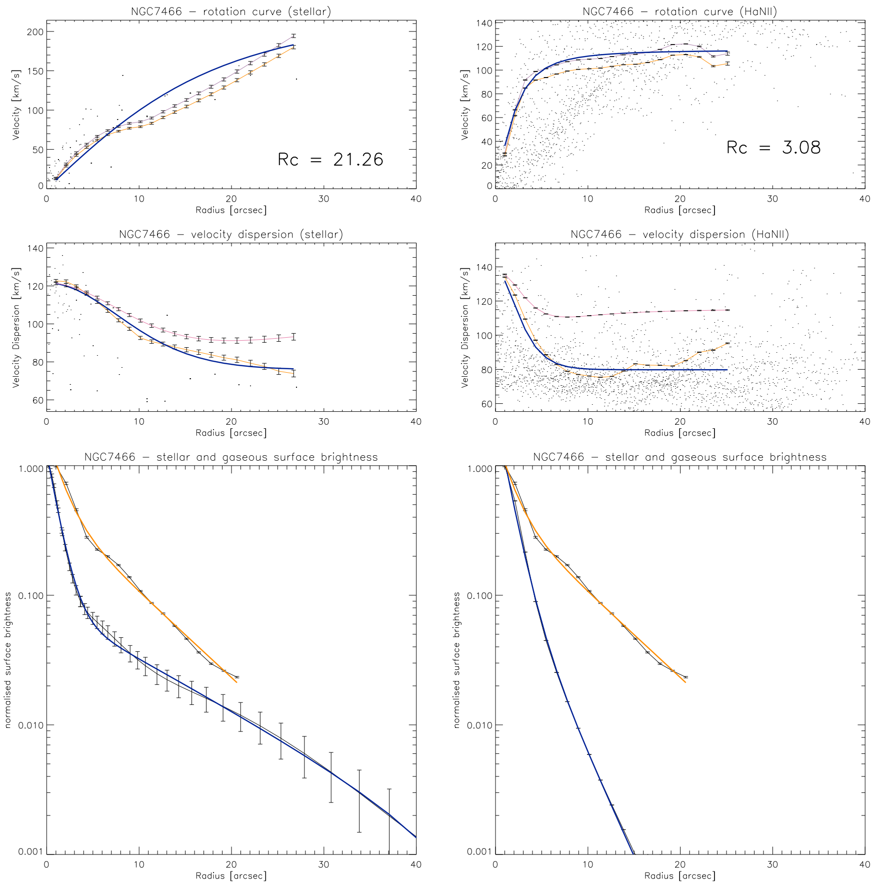

Figure A.23: This figure shows the radial profiles of NGC7466.
The *upper left panel* shows the velocity profile extracted with kinemetry (orange line), as well as the inclination corrected one (purple line) together with its best power law fit. The black dots represent the input data of kinemetry. Given is also the core radius of the fit in the lower right corner. The *upper right panel* shows the same but for the gas data.
The *middle panel* shows the observed velocity dispersion (orange line) with its single exponential fit and the from the fit obtained radial velocity dispersion σ_r (purple line). The *middle right panel* shows the same but for the gas data.
The *lower left panel* shows the radial surface brightness profile of extracted with MGE together with its best triple exponential fit (blue line) and the surface brightness of the gas extracted with kinemetry together with its best fit (orange line). In the *lower right panel* the MGE output is exchanged with the kinemetry output of the binned stellar flux analysis.

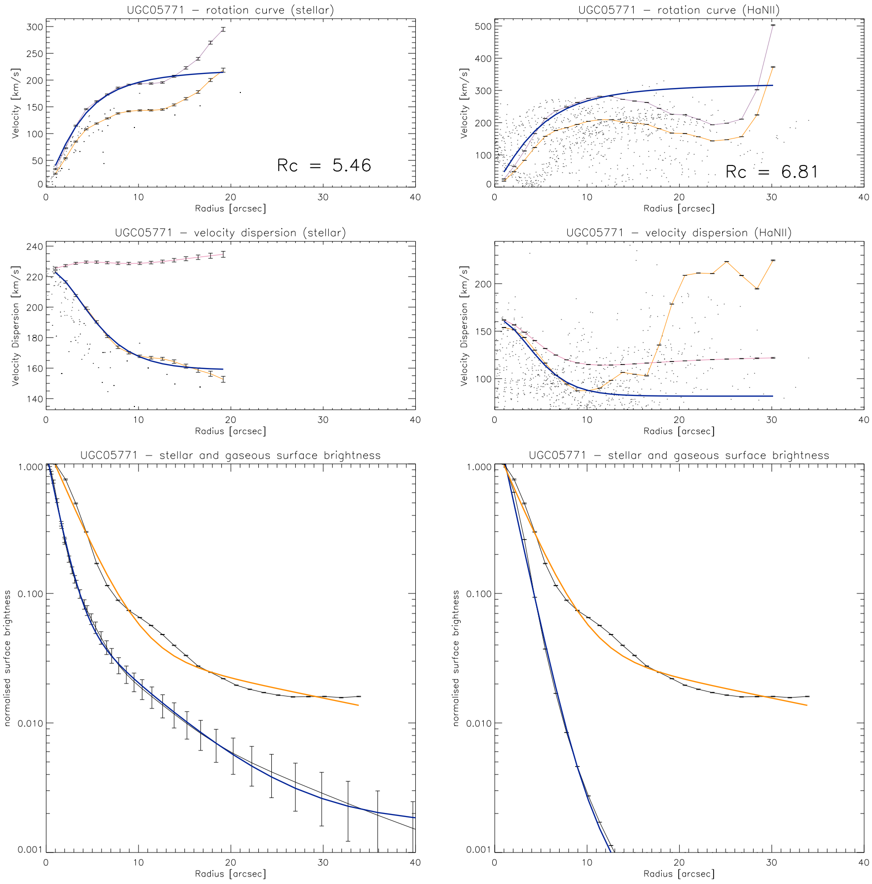

Figure A.24: This figure shows the radial profiles of UGC05771.
The *upper left panel* shows the velocity profile extracted with kinemetry (orange line), as well as the inclination corrected one (purple line) together with its best power law fit. The black dots represent the input data of kinemetry. Given is also the core radius of the fit in the lower right corner. The *upper right panel* shows the same but for the gas data.
The *middle panel* shows the observed velocity dispersion (orange line) with its single exponential fit and the from the fit obtained radial velocity dispersion σ_r (purple line). The *middle right panel* shows the same but for the gas data.
The *lower left panel* shows the radial surface brightness profile of extracted with MGE together with its best triple exponential fit (blue line) and the surface brightness of the gas extracted with kinemetry together with its best fit (orange line). In the *lower right panel* the MGE output is exchanged with the kinemetry output of the binned stellar flux analysis.

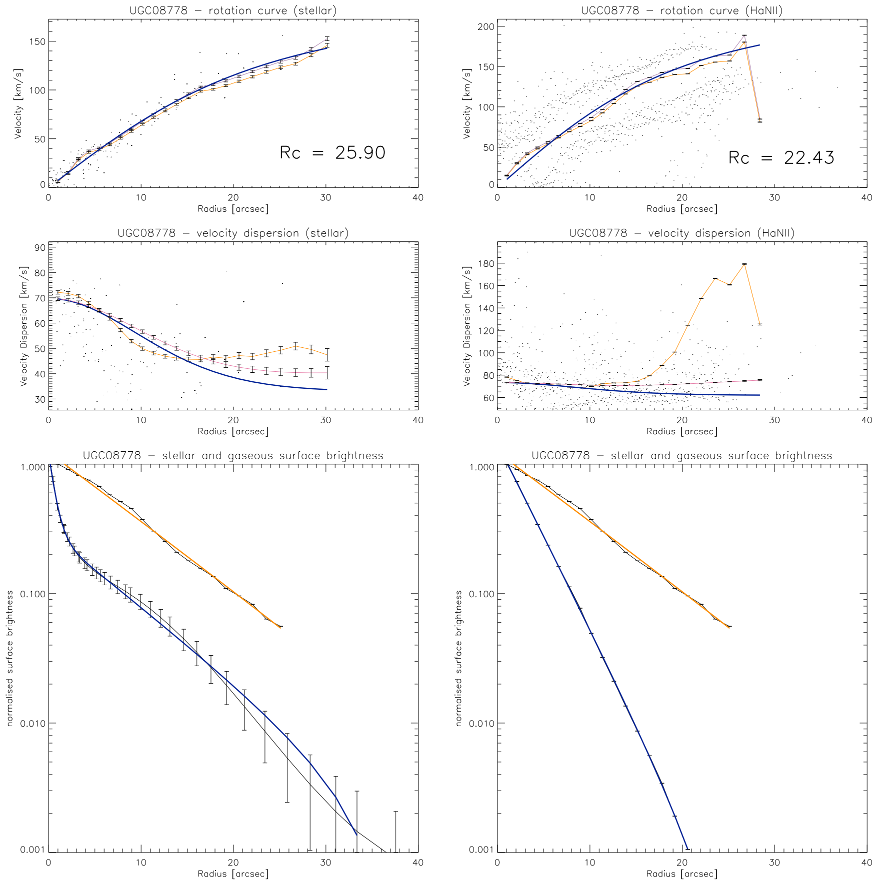

Figure A.25: This figure shows the radial profiles of UGC08778.
The *upper left panel* shows the velocity profile extracted with kinemetry (orange line), as well as the inclination corrected one (purple line) together with its best power law fit. The black dots represent the input data of kinemetry. Given is also the core radius of the fit in the lower right corner. The *upper right panel* shows the same but for the gas data.
The *middle panel* shows the observed velocity dispersion (orange line) with its single exponential fit and the from the fit obtained radial velocity dispersion σ_r (purple line). The *middle right panel* shows the same but for the gas data.
The *lower left panel* shows the radial surface brightness profile of extracted with MGE together with its best triple exponential fit (blue line) and the surface brightness of the gas extracted with kinemetry together with its best fit (orange line). In the *lower right panel* the MGE output is exchanged with the kinemetry output of the binned stellar flux analysis.

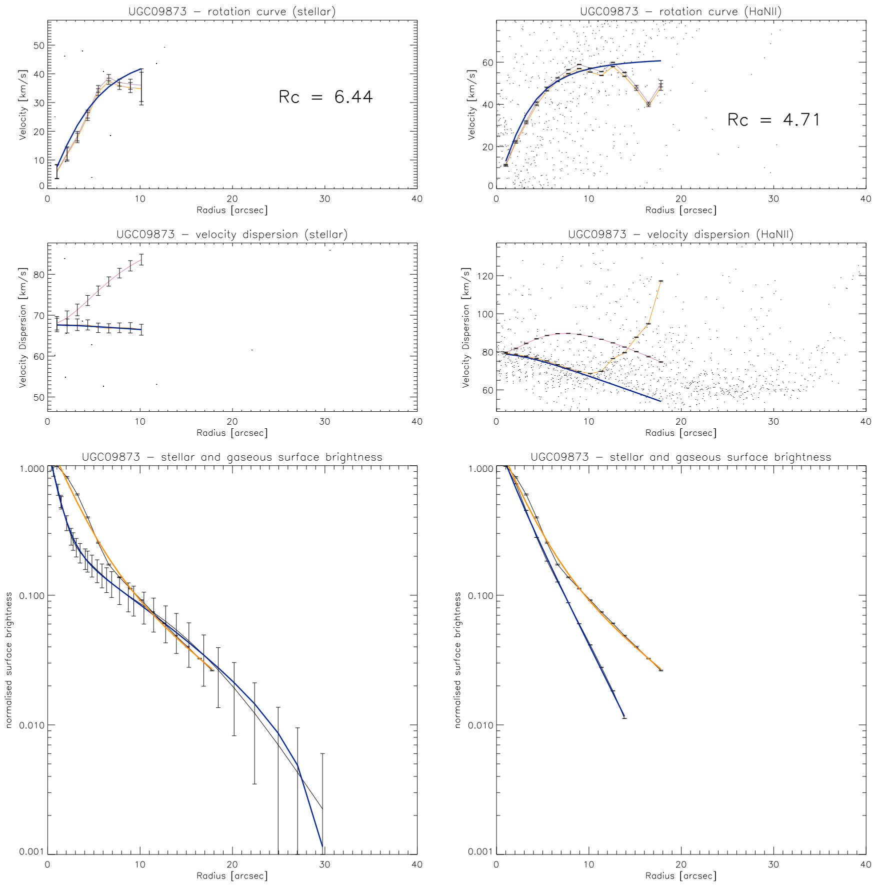

Figure A.26: This figure shows the radial profiles of UGC09873.
The *upper left panel* shows the velocity profile extracted with kinemetry (orange line), as well as the inclination corrected one (purple line) together with its best power law fit. The black dots represent the input data of kinemetry. Given is also the core radius of the fit in the lower right corner. The *upper right panel* shows the same but for the gas data.
The *middle panel* shows the observed velocity dispersion (orange line) with its single exponential fit and the from the fit obtained radial velocity dispersion σ_r (purple line). The *middle right panel* shows the same but for the gas data.
The *lower left panel* shows the radial surface brightness profile of extracted with MGE together with its best triple exponential fit (blue line) and the surface brightness of the gas extracted with kinemetry together with its best fit (orange line). In the *lower right panel* the MGE output is exchanged with the kinemetry output of the binned stellar flux analysis.

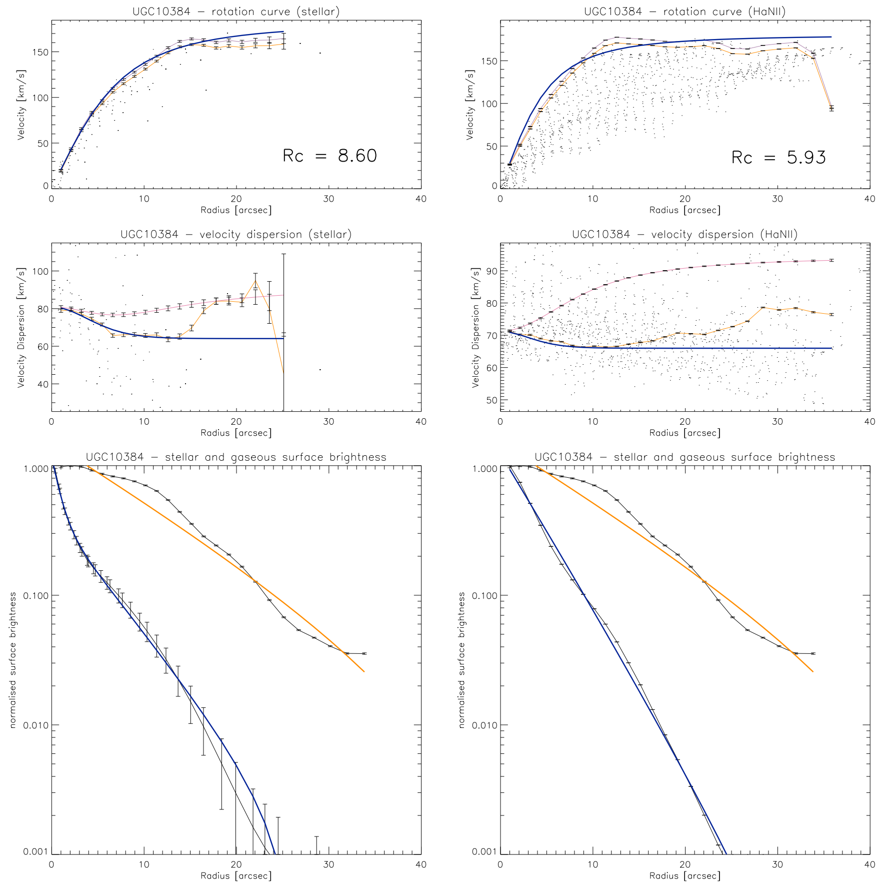

Figure A.27: This figure shows the radial profiles of UGC10384.
The *upper left panel* shows the velocity profile extracted with kinemetry (orange line), as well as the inclination corrected one (purple line) together with its best power law fit. The black dots represent the input data of kinemetry. Given is also the core radius of the fit in the lower right corner. The *upper right panel* shows the same but for the gas data.
The *middle panel* shows the observed velocity dispersion (orange line) with its single exponential fit and the from the fit obtained radial velocity dispersion σ_r (purple line). The *middle right panel* shows the same but for the gas data.
The *lower left panel* shows the radial surface brightness profile of extracted with MGE together with its best triple exponential fit (blue line) and the surface brightness of the gas extracted with kinemetry together with its best fit (orange line). In the *lower right panel* the MGE output is exchanged with the kinemetry output of the binned stellar flux analysis.

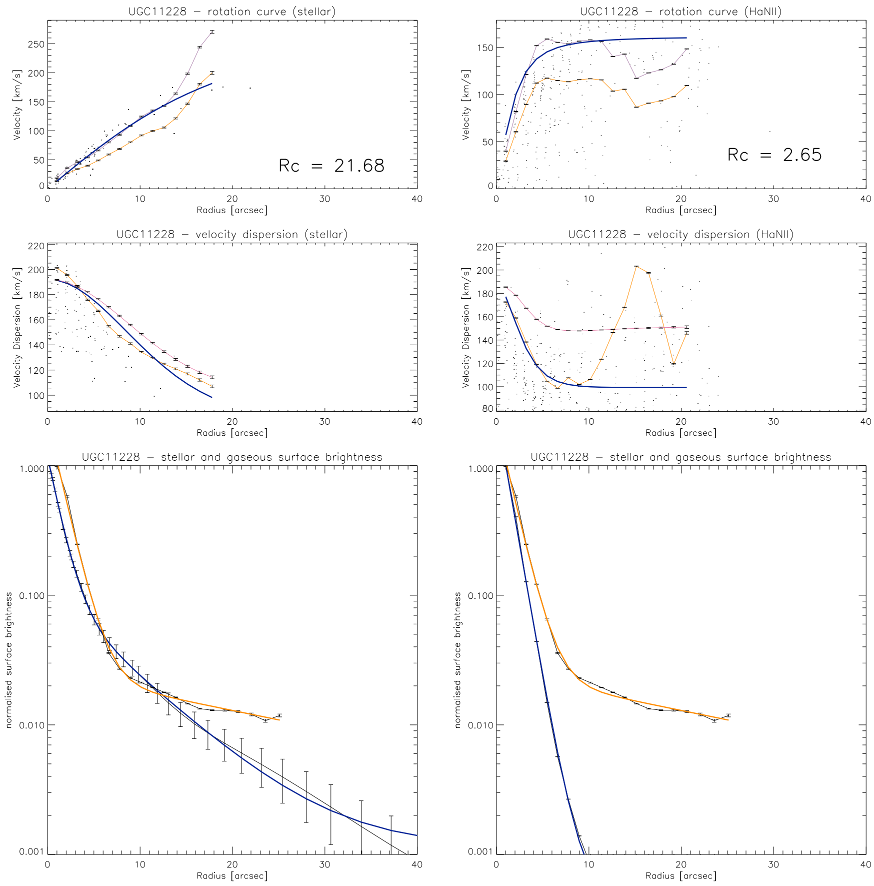

Figure A.28: This figure shows the radial profiles of UGC11228.
The *upper left panel* shows the velocity profile extracted with kinemetry (orange line), as well as the inclination corrected one (purple line) together with its best power law fit. The black dots represent the input data of kinemetry. Given is also the core radius of the fit in the lower right corner. The *upper right panel* shows the same but for the gas data.
The *middle panel* shows the observed velocity dispersion (orange line) with its single exponential fit and the from the fit obtained radial velocity dispersion σ_r (purple line). The *middle right panel* shows the same but for the gas data.
The *lower left panel* shows the radial surface brightness profile of extracted with MGE together with its best triple exponential fit (blue line) and the surface brightness of the gas extracted with kinemetry together with its best fit (orange line). In the *lower right panel* the MGE output is exchanged with the kinemetry output of the binned stellar flux analysis.

A.5 Asymmetric Drift Correction

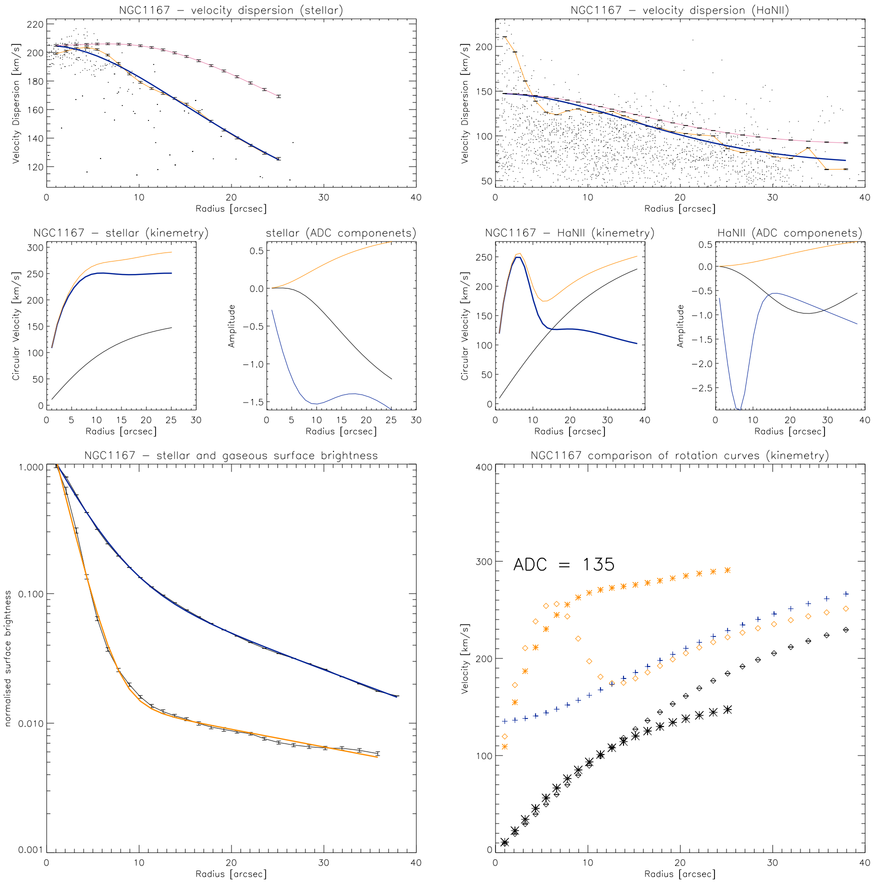

Figure A.29: The asymmetric drift analysis of NGC1167.
The *top row* shows the extracted velocity dispersion profile (orange line) of the stars *left* and the gas *right* together with its best exponential fit and the calculated radial velocity dispersion (purple line).
The *first panel* in the *middle row* shows on the left hand side the fit to the observed rotational velocity (black line) and the true circular velocity (orange line), as well as the ADC itself in blue. The *second panel* shows the different terms of the ADC seperated. In blue the logarithmic derivative of the surface brightness and in black the logarithmic derivative of the squared radial velocity dispersion. The green line is dominated by the value of the core radius, reaching one at infinity. The *third* and *fourth panel* show the same, but for the gas.
The *lower left panel* shows the surface brightness profile of the stars (blue line) and the those of the gas (orange line) both extracted from the unbinned CALIFA data with kinemetry.
The *lower right panel* is the first try of finding the correct plateau of the ADC of the gas. Black stars (stars) and diamonds (gas) are the observed profiles, the orange ones are the true circular profiles obtained from the fits and the blue crosses should be the true circular profile of the gas, when ignoring turbulent velocity dispersion.

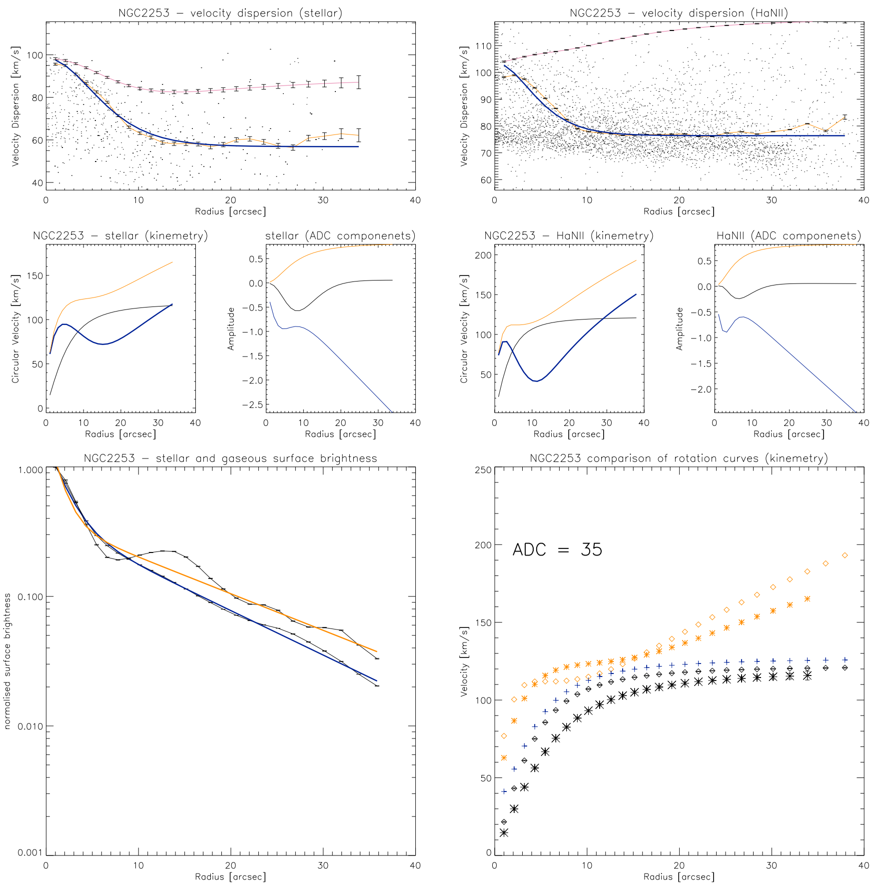

Figure A.30: The asymmetric drift analysis of NGC2253.
The *top row* shows the extracted velocity dispersion profile (orange line) of the stars *left* and the gas *right* together with its best exponential fit and the calculated radial velocity dispersion (purple line).
The *first panel* in the *middle row* shows on the left hand side the fit to the observed rotational velocity (black line) and the true circular velocity (orange line), as well as the ADC itself in blue. The *second panel* shows the different terms of the ADC seperated. In blue the logarithmic derivative of the surface brightness and in black the logarithmic derivative of the squared radial velocity dispersion. The green line is dominated by the value of the core radius, reaching one at infinity. The *third* and *fourth panel* show the same, but for the gas.
The *lower left panel* shows the surface brightness profile of the stars (blue line) and the those of the gas (orange line) both extracted from the unbinned CALIFA data with kinemetry.
The *lower right panel* is the first try of finding the correct plateau of the ADC of the gas. Black stars (stars) and diamonds (gas) are the observed profiles, the orange ones are the true circular profiles obtained from the fits and the blue crosses should be the true circular profile of the gas, when ignoring turbulent velocity dispersion.

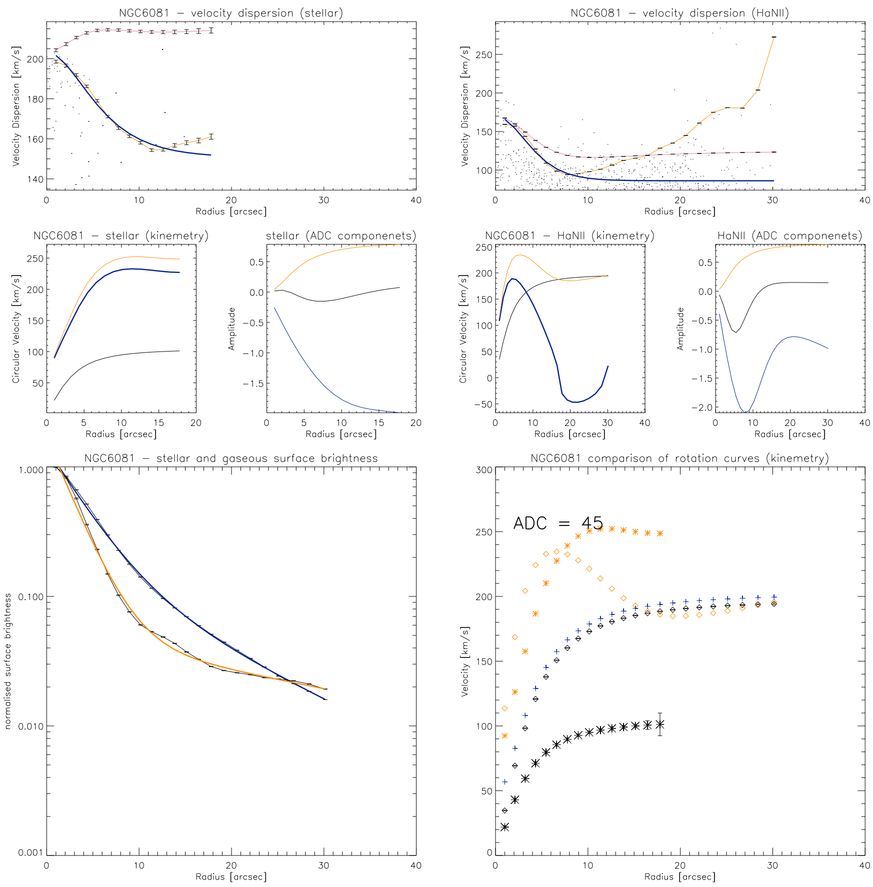

Figure A.31: The asymmetric drift analysis of NGC6081.
The *top row* shows the extracted velocity dispersion profile (orange line) of the stars *left* and the gas *right* together with its best exponential fit and the calculated radial velocity dispersion (purple line).
The *first panel* in the *middle row* shows on the left hand side the fit to the observed rotational velocity (black line) and the true circular velocity (orange line), as well as the ADC itself in blue. The *second panel* shows the different terms of the ADC seperated. In blue the logarithmic derivative of the surface brightness and in black the logarithmic derivative of the squared radial velocity dispersion. The green line is dominated by the value of the core radius, reaching one at infinity. The *third* and *fourth panel* show the same, but for the gas.
The *lower left panel* shows the surface brightness profile of the stars (blue line) and the those of the gas (orange line) both extracted from the unbinned CALIFA data with kinemetry.
The *lower right panel* is the first try of finding the correct plateau of the ADC of the gas. Black stars (stars) and diamonds (gas) are the observed profiles, the orange ones are the true circular profiles obtained from the fits and the blue crosses should be the true circular profile of the gas, when ignoring turbulent velocity dispersion.

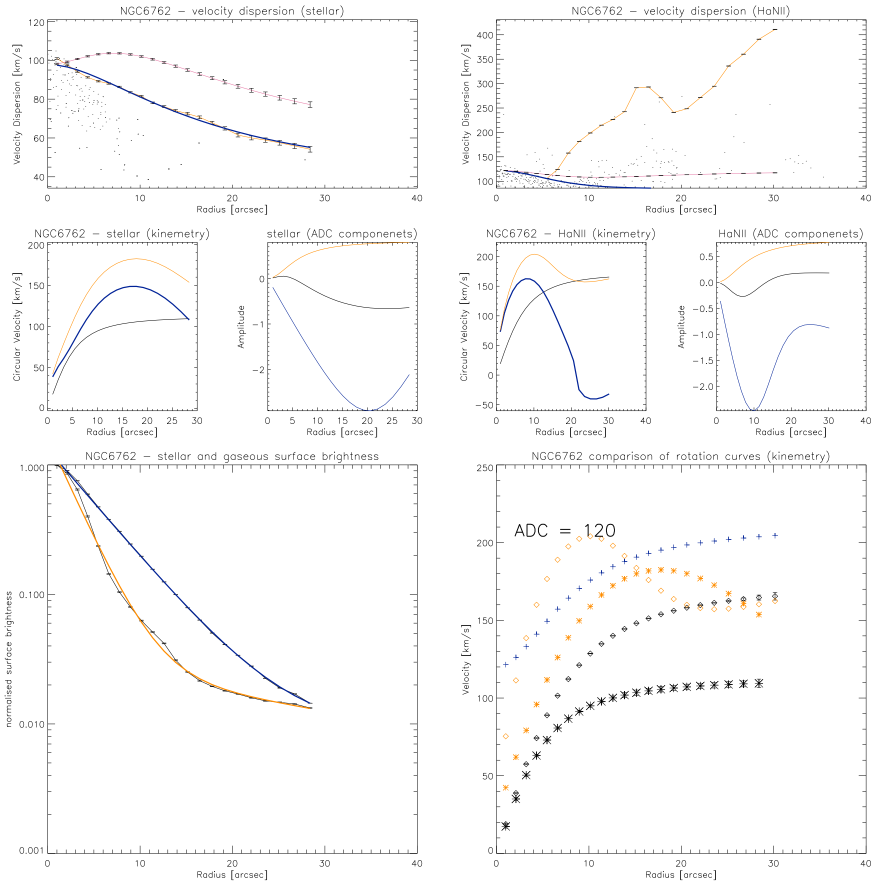

Figure A.32: The asymmetric drift analysis of NGC6762.
The *top row* shows the extracted velocity dispersion profile (orange line) of the stars *left* and the gas *right* together with its best exponential fit and the calculated radial velocity dispersion (purple line).
The *first panel* in the *middle row* shows on the left hand side the fit to the observed rotational velocity (black line) and the true circular velocity (orange line), as well as the ADC itself in blue. The *second panel* shows the different terms of the ADC seperated. In blue the logarithmic derivative of the surface brightness and in black the logarithmic derivative of the squared radial velocity dispersion. The green line is dominated by the value of the core radius, reaching one at infinity. The *third* and *fourth panel* show the same, but for the gas.
The *lower left panel* shows the surface brightness profile of the stars (blue line) and the those of the gas (orange line) both extracted from the unbinned CALIFA data with kinemetry.
The *lower right panel* is the first try of finding the correct plateau of the ADC of the gas. Black stars (stars) and diamonds (gas) are the observed profiles, the orange ones are the true circular profiles obtained from the fits and the blue crosses should be the true circular profile of the gas, when ignoring turbulent velocity dispersion.

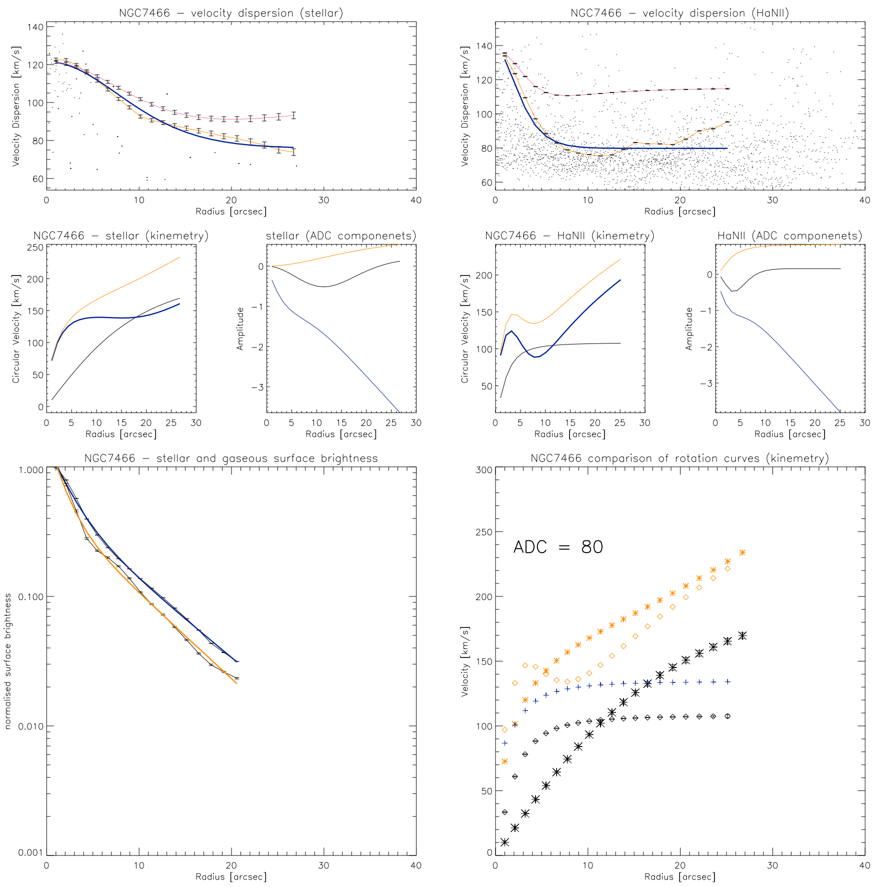

Figure A.33: The asymmetric drift analysis of NGC7466.
The *top row* shows the extracted velocity dispersion profile (orange line) of the stars *left* and the gas *right* together with its best exponential fit and the calculated radial velocity dispersion (purple line).
The *first panel* in the *middle row* shows on the left hand side the fit to the observed rotational velocity (black line) and the true circular velocity (orange line), as well as the ADC itself in blue. The *second panel* shows the different terms of the ADC seperated. In blue the logarithmic derivative of the surface brightness and in black the logarithmic derivative of the squared radial velocity dispersion. The green line is dominated by the value of the core radius, reaching one at infinity. The *third* and *fourth panel* show the same, but for the gas.
The *lower left panel* shows the surface brightness profile of the stars (blue line) and the those of the gas (orange line) both extracted from the unbinned CALIFA data with kinemetry.
The *lower right panel* is the first try of finding the correct plateau of the ADC of the gas. Black stars (stars) and diamonds (gas) are the observed profiles, the orange ones are the true circular profiles obtained from the fits and the blue crosses should be the true circular profile of the gas, when ignoring turbulent velocity dispersion.

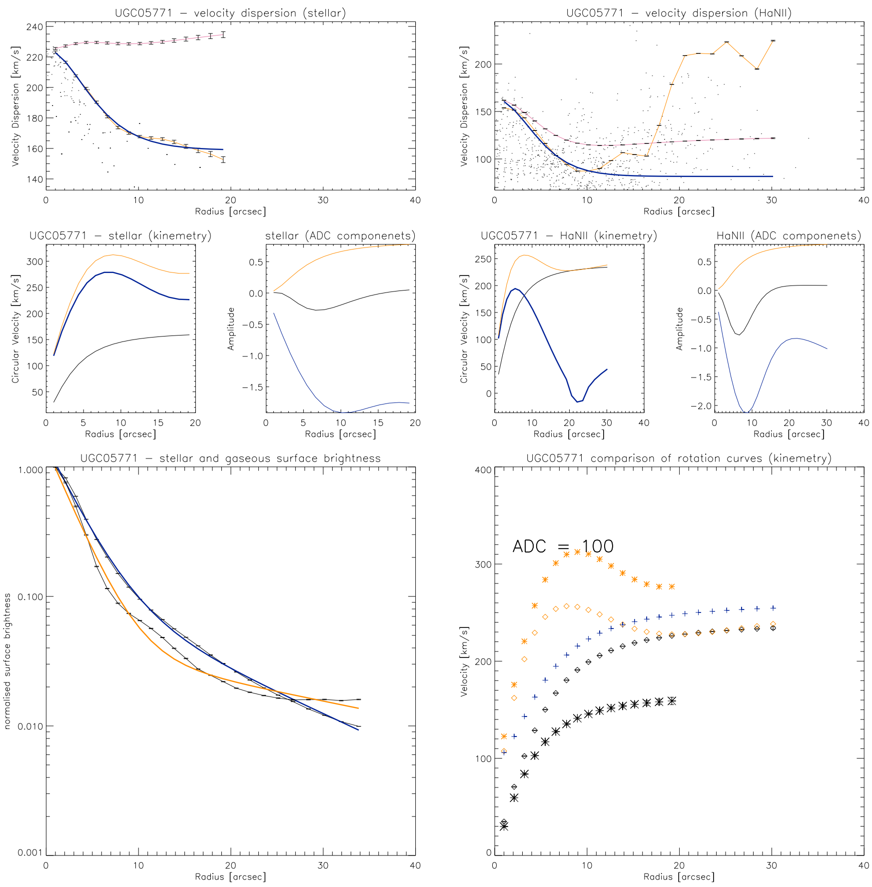

Figure A.34: The asymmetric drift analysis of UGC05771.

The *top row* shows the extracted velocity dispersion profile (orange line) of the stars *left* and the gas *right* together with its best exponential fit and the calculated radial velocity dispersion (purple line).

The *first panel* in the *middle row* shows on the left hand side the fit to the observed rotational velocity (black line) and the true circular velocity (orange line), as well as the ADC itself in blue. The *second panel* shows the different terms of the ADC seperated. In blue the logarithmic derivative of the surface brightness and in black the logarithmic derivative of the squared radial velocity dispersion. The green line is dominated by the value of the core radius, reaching one at infinity. The *third* and *fourth panel* show the same, but for the gas.

The *lower left panel* shows the surface brightness profile of the stars (blue line) and the those of the gas (orange line) both extracted from the unbinned CALIFA data with kinemetry.

The *lower right panel* is the first try of finding the correct plateau of the ADC of the gas. Black stars (stars) and diamonds (gas) are the observed profiles, the orange ones are the true circular profiles obtained from the fits and the blue crosses should be the true circular profile of the gas, when ignoring turbulent velocity dispersion.

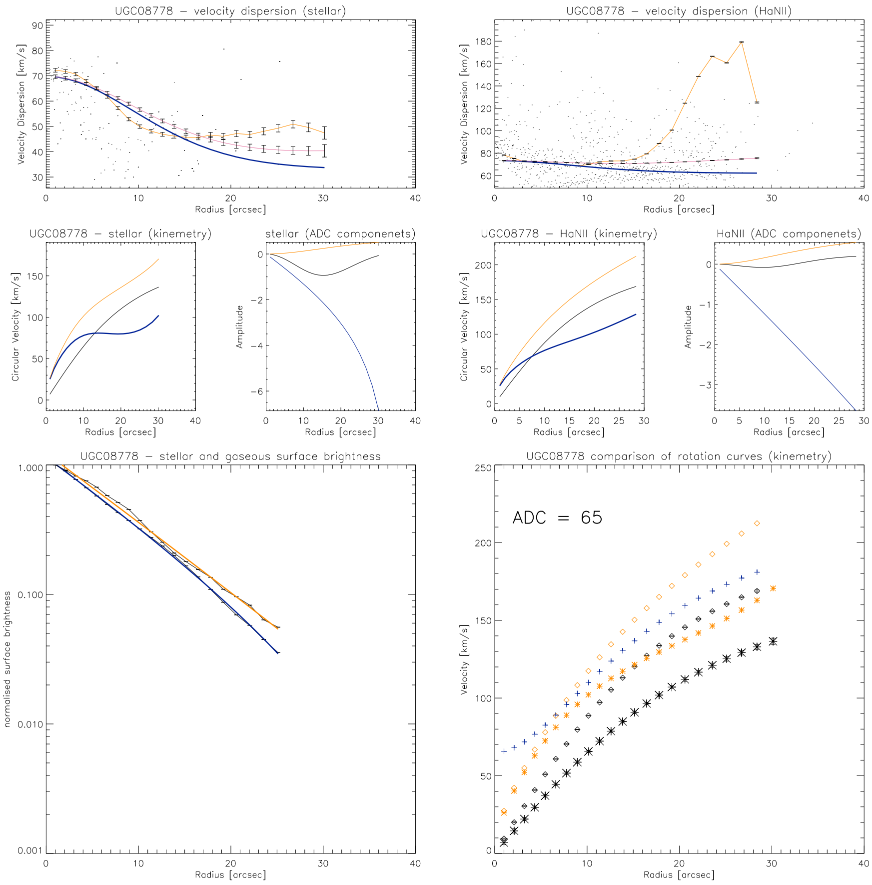

Figure A.35: The asymmetric drift analysis of UGC08778.
The *top row* shows the extracted velocity dispersion profile (orange line) of the stars *left* and the gas *right* together with its best exponential fit and the calculated radial velocity dispersion (purple line).
The *first panel* in the *middle row* shows on the left hand side the fit to the observed rotational velocity (black line) and the true circular velocity (orange line), as well as the ADC itself in blue. The *second panel* shows the different terms of the ADC seperated. In blue the logarithmic derivative of the surface brightness and in black the logarithmic derivative of the squared radial velocity dispersion. The green line is dominated by the value of the core radius, reaching one at infinity. The *third* and *fourth panel* show the same, but for the gas.
The *lower left panel* shows the surface brightness profile of the stars (blue line) and the those of the gas (orange line) both extracted from the unbinned CALIFA data with kinemetry.
The *lower right panel* is the first try of finding the correct plateau of the ADC of the gas. Black stars (stars) and diamonds (gas) are the observed profiles, the orange ones are the true circular profiles obtained from the fits and the blue crosses should be the true circular profile of the gas, when ignoring turbulent velocity dispersion.

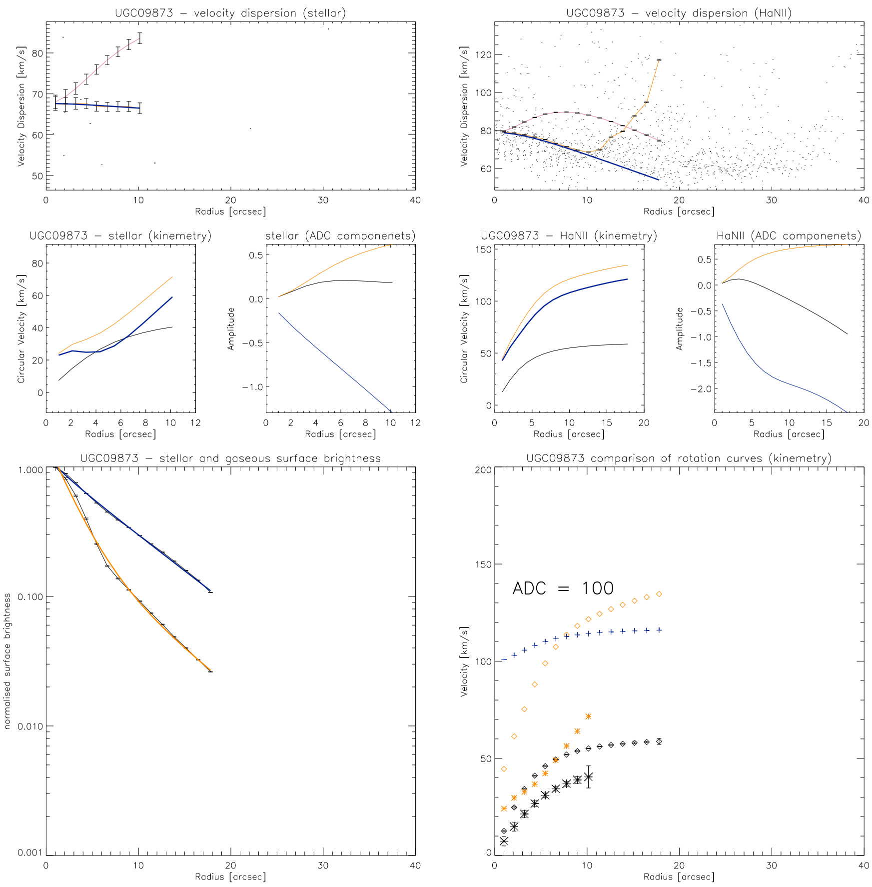

Figure A.36: The asymmetric drift analysis of UGC09873.
The *top row* shows the extracted velocity dispersion profile (orange line) of the stars *left* and the gas *right* together with its best exponential fit and the calculated radial velocity dispersion (purple line).
The *first panel* in the *middle row* shows on the left hand side the fit to the observed rotational velocity (black line) and the true circular velocity (orange line), as well as the ADC itself in blue. The *second panel* shows the different terms of the ADC seperated. In blue the logarithmic derivative of the surface brightness and in black the logarithmic derivative of the squared radial velocity dispersion. The green line is dominated by the value of the core radius, reaching one at infinity. The *third* and *fourth panel* show the same, but for the gas.
The *lower left panel* shows the surface brightness profile of the stars (blue line) and the those of the gas (orange line) both extracted from the unbinned CALIFA data with kinemetry.
The *lower right panel* is the first try of finding the correct plateau of the ADC of the gas. Black stars (stars) and diamonds (gas) are the observed profiles, the orange ones are the true circular profiles obtained from the fits and the blue crosses should be the true circular profile of the gas, when ignoring turbulent velocity dispersion.

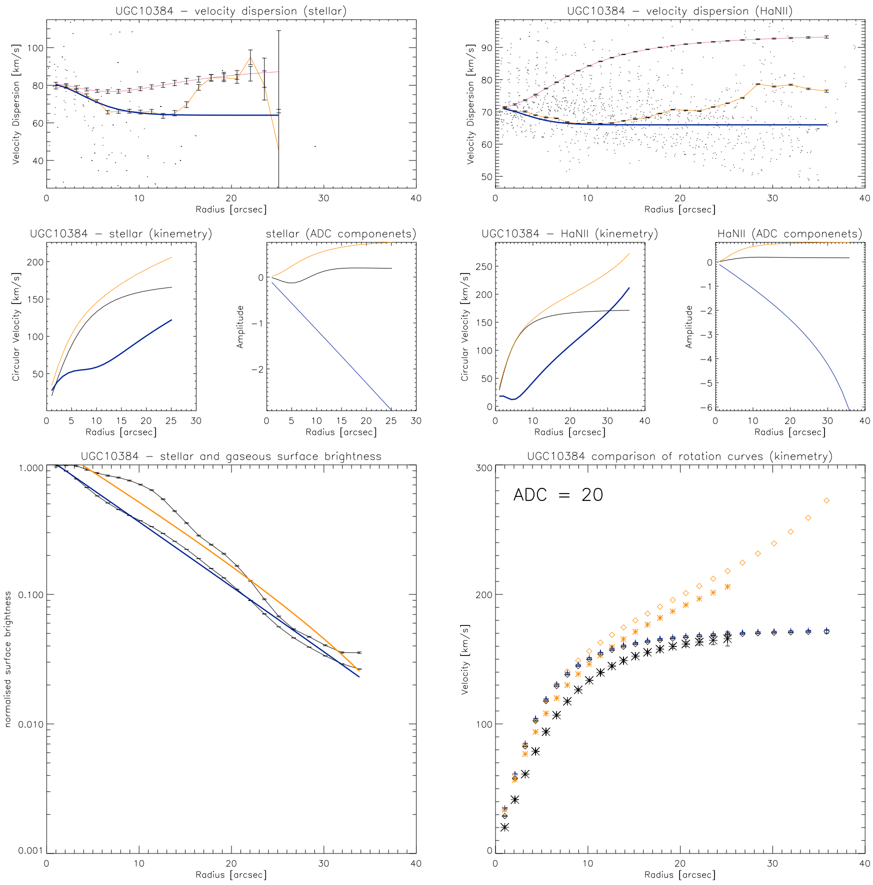

Figure A.37: The asymmetric drift analysis of UGC10384.
The *top row* shows the extracted velocity dispersion profile (orange line) of the stars *left* and the gas *right* together with its best exponential fit and the calculated radial velocity dispersion (purple line).
The *first panel* in the *middle row* shows on the left hand side the fit to the observed rotational velocity (black line) and the true circular velocity (orange line), as well as the ADC itself in blue. The *second panel* shows the different terms of the ADC seperated. In blue the logarithmic derivative of the surface brightness and in black the logarithmic derivative of the squared radial velocity dispersion. The green line is dominated by the value of the core radius, reaching one at infinity. The *third* and *fourth panel* show the same, but for the gas.
The *lower left panel* shows the surface brightness profile of the stars (blue line) and the those of the gas (orange line) both extracted from the unbinned CALIFA data with kinemetry.
The *lower right panel* is the first try of finding the correct plateau of the ADC of the gas. Black stars (stars) and diamonds (gas) are the observed profiles, the orange ones are the true circular profiles obtained from the fits and the blue crosses should be the true circular profile of the gas, when ignoring turbulent velocity dispersion.

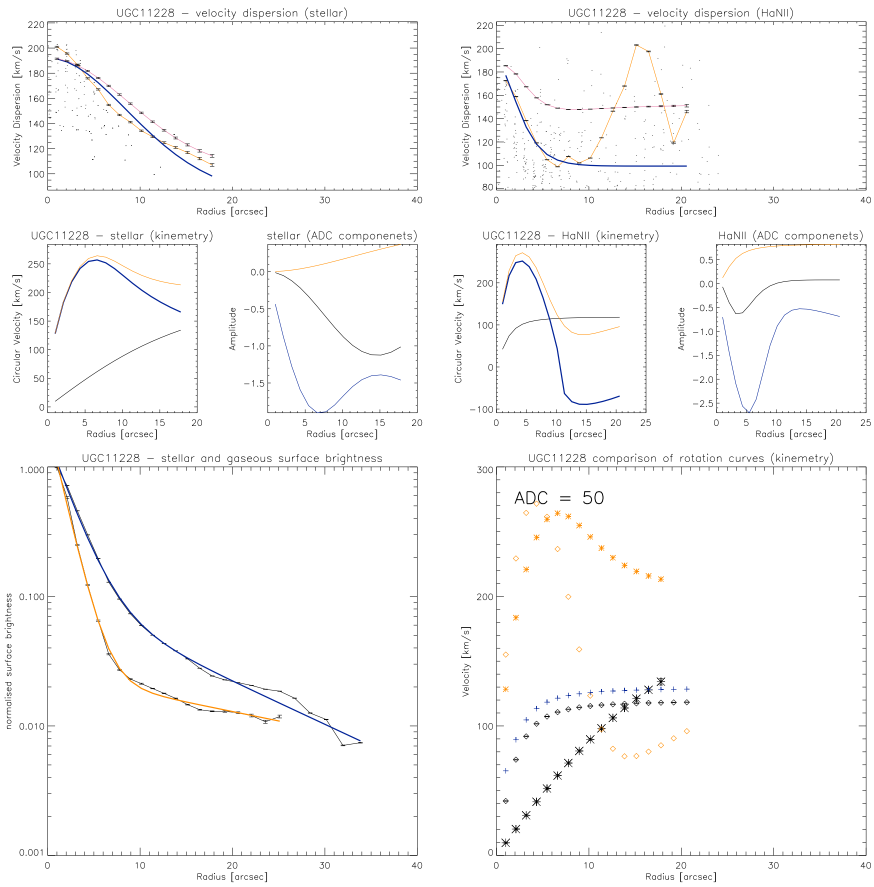

Figure A.38: The asymmetric drift analysis of UGC11228.
The *top row* shows the extracted velocity dispersion profile (orange line) of the stars *left* and the gas *right* together with its best exponential fit and the calculated radial velocity dispersion (purple line).
The *first panel* in the *middle row* shows on the left hand side the fit to the observed rotational velocity (black line) and the true circular velocity (orange line), as well as the ADC itself in blue. The *second panel* shows the different terms of the ADC seperated. In blue the logarithmic derivative of the surface brightness and in black the logarithmic derivative of the squared radial velocity dispersion. The green line is dominated by the value of the core radius, reaching one at infinity. The *third* and *fourth panel* show the same, but for the gas.
The *lower left panel* shows the surface brightness profile of the stars (blue line) and the those of the gas (orange line) both extracted from the unbinned CALIFA data with kinemetry.
The *lower right panel* is the first try of finding the correct plateau of the ADC of the gas. Black stars (stars) and diamonds (gas) are the observed profiles, the orange ones are the true circular profiles obtained from the fits and the blue crosses should be the true circular profile of the gas, when ignoring turbulent velocity dispersion.

A.6 Other Gaseous Tracers

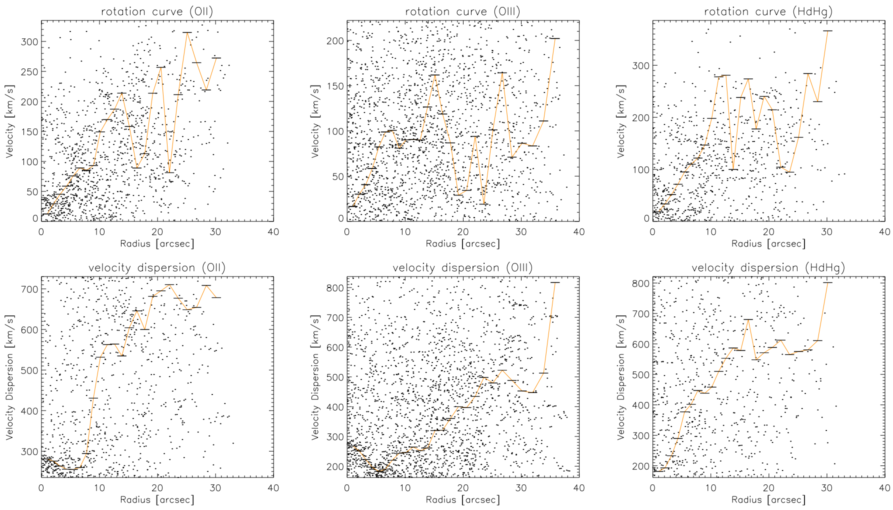

Figure A.39: The radial profiles of the other lines available for the gas kinematics of NGC1167. The *upper* row shows the radial velocity profiles and the *lower* row shows the radial velocity dispersion profiles. The black dots represent in each panel the input data for kinemetry.

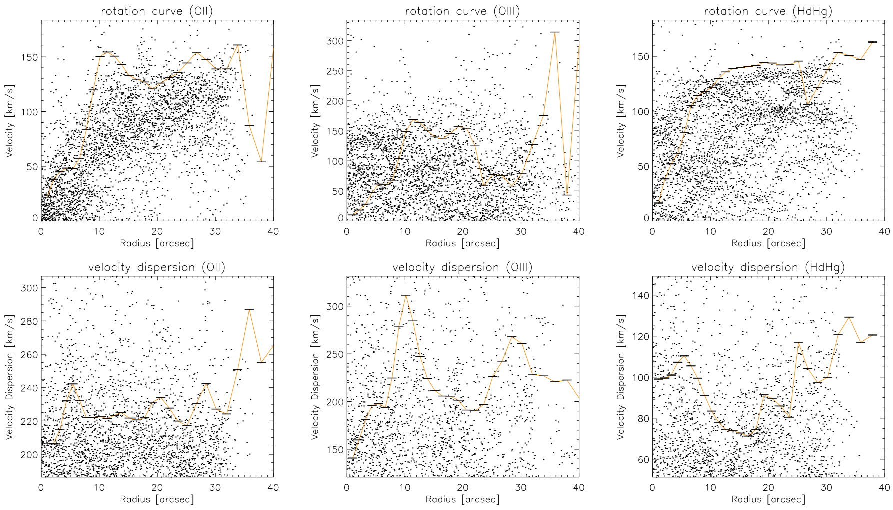

Figure A.40: The radial profiles of the other lines available for the gas kinematics of NGC2253. The *upper* row shows the radial velocity profiles and the *lower* row shows the radial velocity dispersion profiles. The black dots represent in each panel the input data for kinemetry.

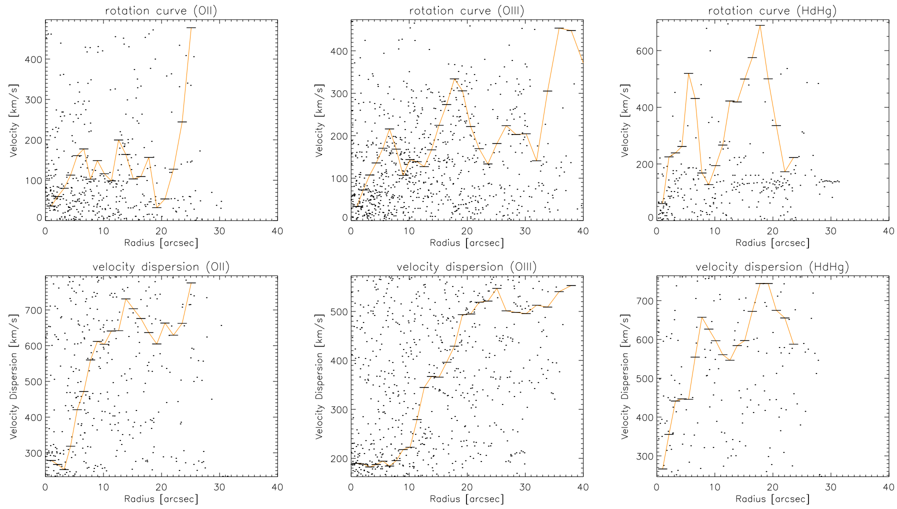

Figure A.41: The radial profiles of the other lines available for the gas kinematics of NGC6081. The *upper* row shows the radial velocity profiles and the *lower* row shows the radial velocity dispersion profiles. The black dots represent in each panel the input data for kinemetry.

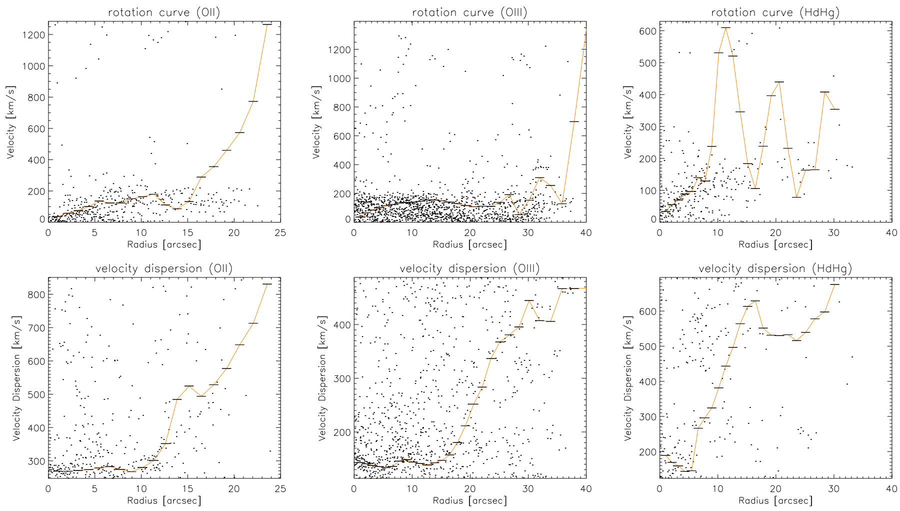

Figure A.42: The radial profiles of the other lines available for the gas kinematics of NGC6762. The *upper* row shows the radial velocity profiles and the *lower* row shows the radial velocity dispersion profiles. The black dots represent in each panel the input data for kinemetry.

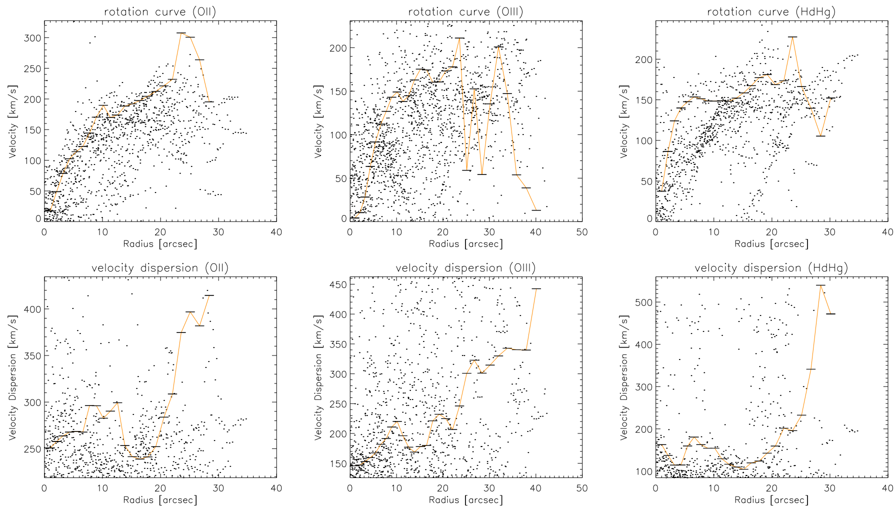

Figure A.43: The radial profiles of the other lines available for the gas kinematics of NGC7466. The *upper* row shows the radial velocity profiles and the *lower* row shows the radial velocity dispersion profiles. The black dots represent in each panel the input data for kinemetry.

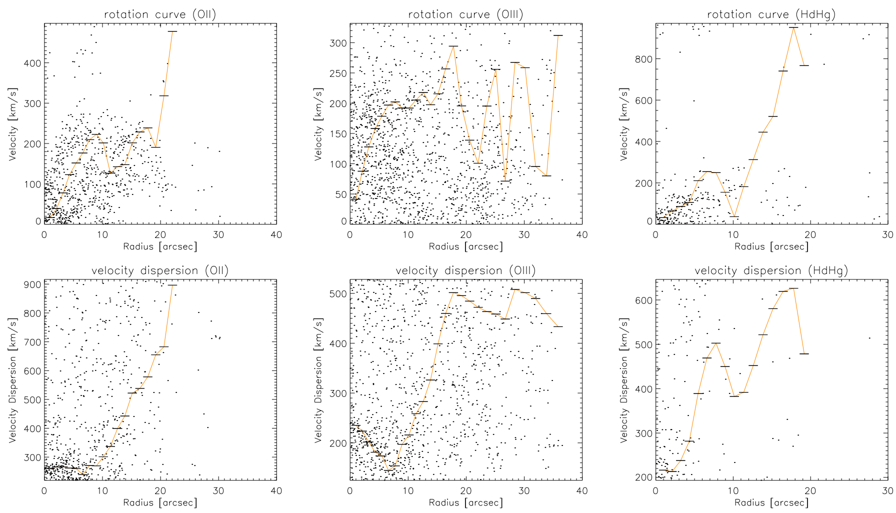

Figure A.44: The radial profiles of the other lines available for the gas kinematics of UGC05771. The *upper* row shows the radial velocity profiles and the *lower* row shows the radial velocity dispersion profiles. The black dots represent in each panel the input data for kinemetry.

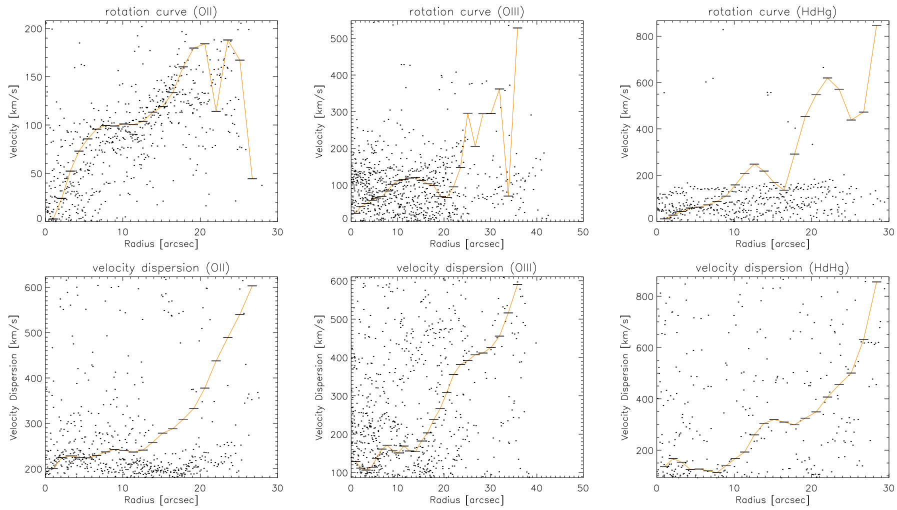

Figure A.45: The radial profiles of the other lines available for the gas kinematics of UGC08778. The *upper* row shows the radial velocity profiles and the *lower* row shows the radial velocity dispersion profiles.

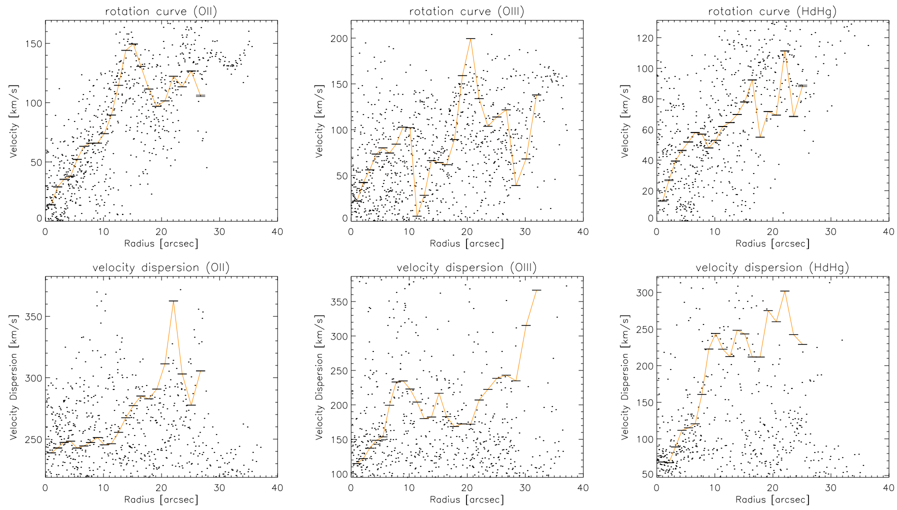

Figure A.46: The radial profiles of the other lines available for the gas kinematics of UGC09873. The *upper* row shows the radial velocity profiles and the *lower* row shows the radial velocity dispersion profiles. The black dots represent in each panel the input data for kinemetry.

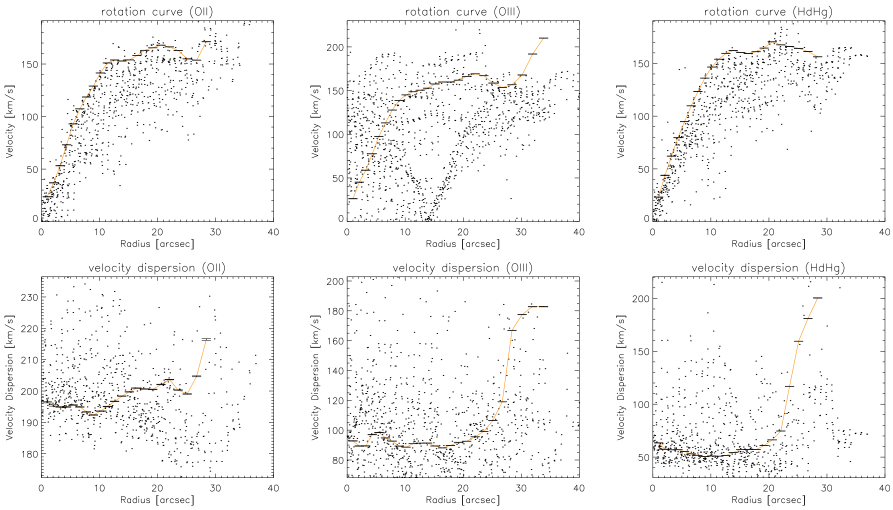

Figure A.47: The radial profiles of the other lines available for the gas kinematics of UGC10384. The *upper* row shows the radial velocity profiles and the *lower* row shows the radial velocity dispersion profiles. The black dots represent in each panel the input data for kinemetry.

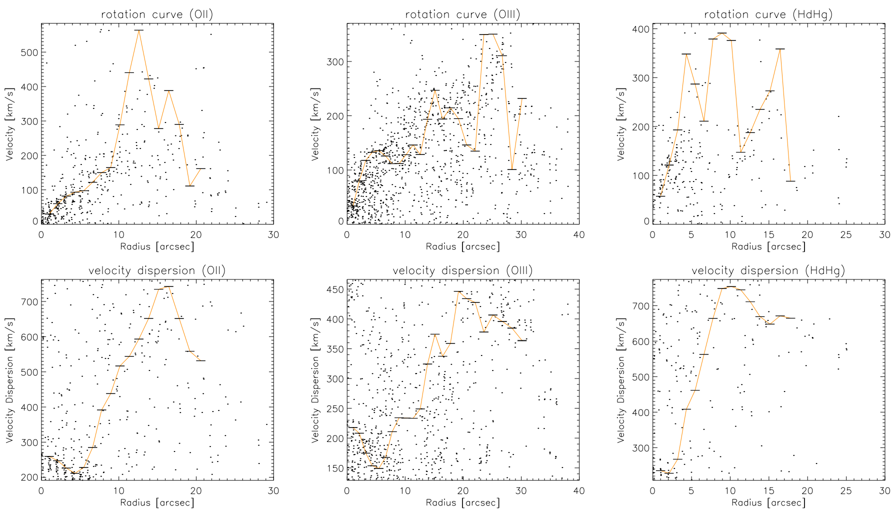

Figure A.48: The radial profiles of the other lines available for the gas kinematics of UGC11228. The *upper row* shows the radial velocity profiles and the *lower row* shows the radial velocity dispersion profiles. The black dots represent in each panel the input data for kinemetry.

A.7 Asymmetric Drift Correction – Wrong Input

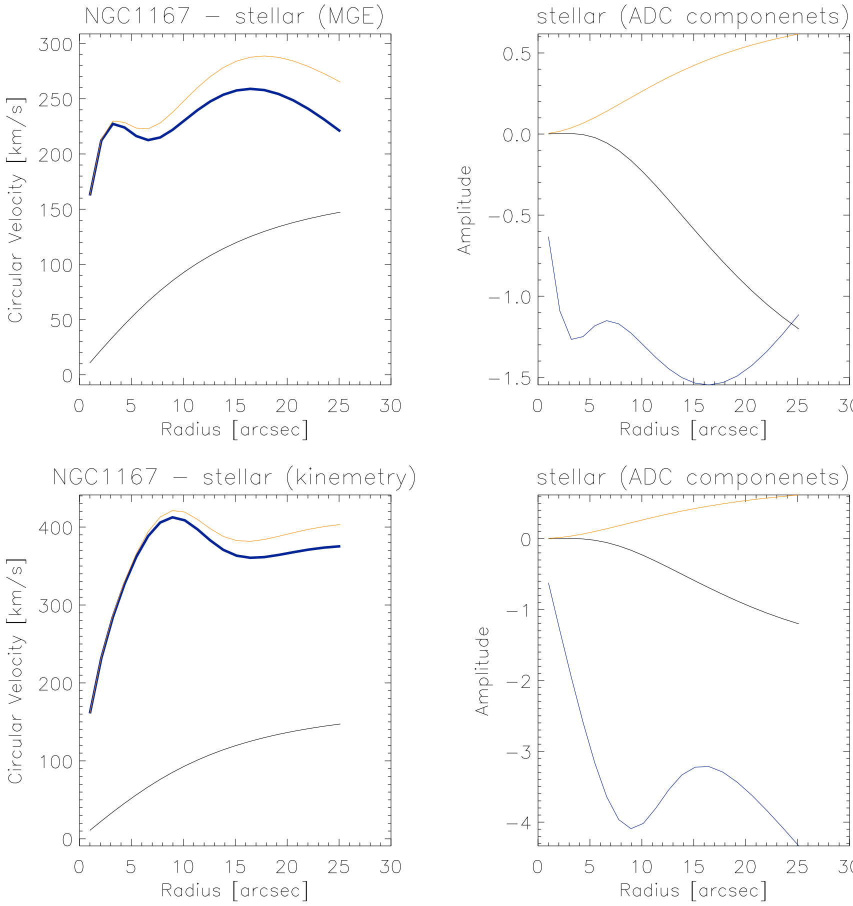

Figure A.49: The true circular velocity and ADC of NGC1167 obtained with the wrong surface brightness profiles.
The *first panel* shows the observed rotational velocity (black line) and the true circular velocity (orange line) for the stars obtained from the stellar surface brightness profile extracted with MGE from the SDSS z-band *top row* and extracted with kinemetry from the binned data of the V1200 setup *bottom row*. In blue the ADC is given.
The *second panel* shows the different terms in the ADC. The blue line represents the logarithmic derivative of the surface brightness and the black one the logarithmic derivative of the squared velocity dispersion. The green line is dominated by the value of the core radius reaching one at infinity.

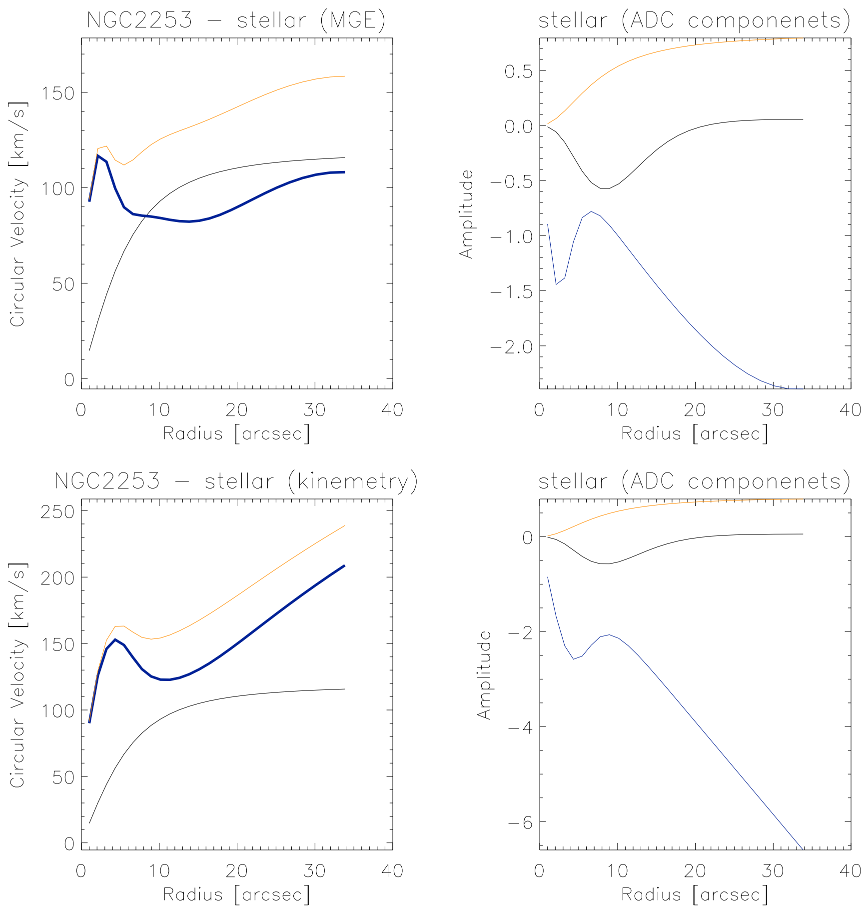

Figure A.50: The true circular velocity and ADC of NGC2253 obtained with the wrong surface brightness profiles.
The *first panel* shows the observed rotational velocity (black line) and the true circular velocity (orange line) for the stars obtained from the stellar surface brightness profile extracted with MGE from the SDSS z-band *top row* and extracted with kinemetry from the binned data of the V1200 setup *bottom row*. In blue the ADC is given.
The *second panel* shows the different terms in the ADC. The blue line represents the logarithmic derivative of the surface brightness and the black one the logarithmic derivative of the squared velocity dispersion. The green line is dominated by the value of the core radius reaching one at infinity.

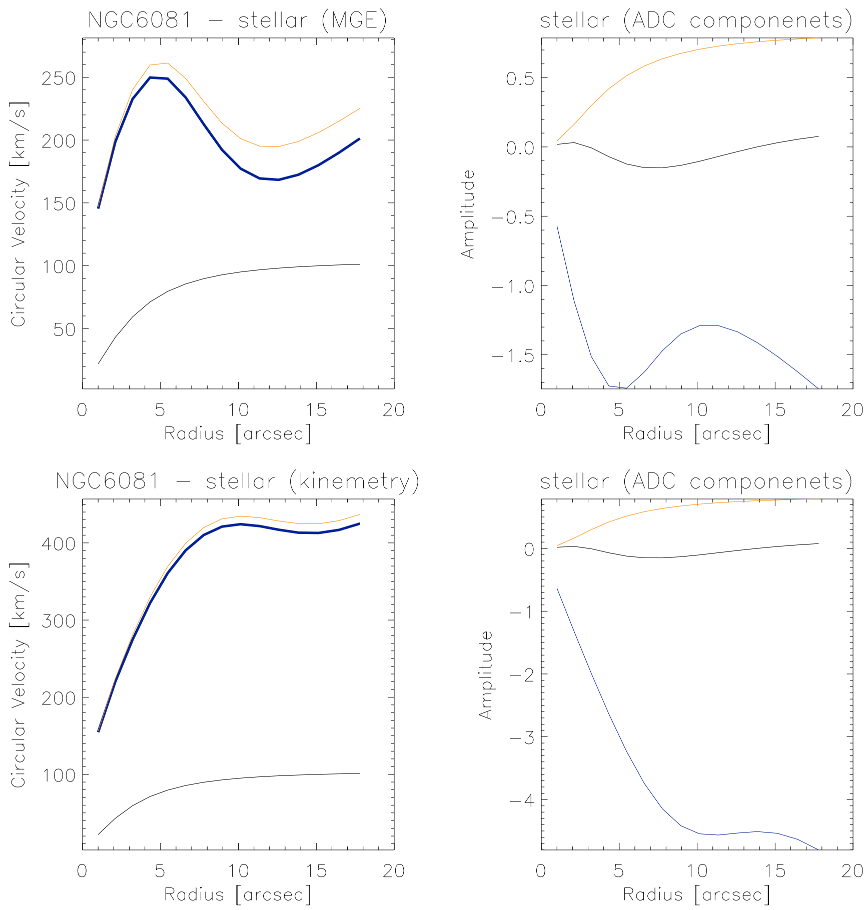

Figure A.51: The true circular velocity and ADC of NGC6081 obtained with the wrong surface brightness profiles.
The *first panel* shows the observed rotational velocity (black line) and the true circular velocity (orange line) for the stars obtained from the stellar surface brightness profile extracted with MGE from the SDSS z-band *top row* and extracted with kinemetry from the binned data of the V1200 setup *bottom row*. In blue the ADC is given.
The *second panel* shows the different terms in the ADC. The blue line represents the logarithmic derivative of the surface brightness and the black one the logarithmic derivative of the squared velocity dispersion. The green line is dominated by the value of the core radius reaching one at infinity.

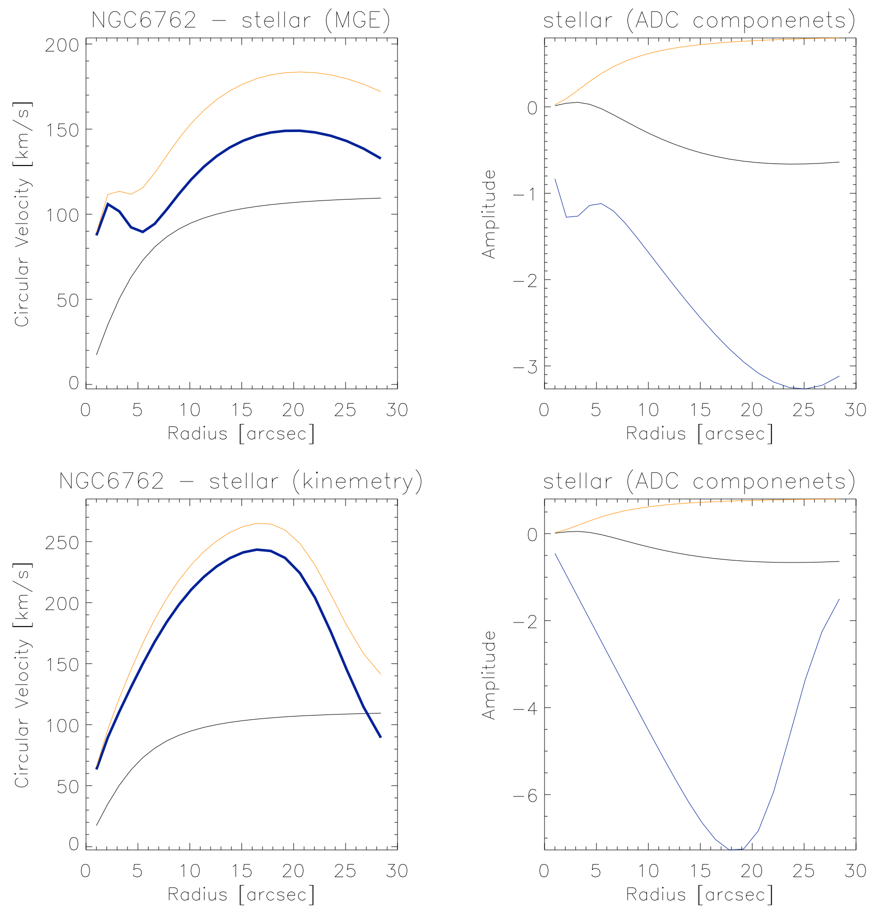

Figure A.52: The true circular velocity and ADC of NGC6762 obtained with the wrong surface brightness profiles.
The *first panel* shows the observed rotational velocity (black line) and the true circular velocity (orange line) for the stars obtained from the stellar surface brightness profile extracted with MGE from the SDSS z-band *top row* and extracted with kinemetry from the binned data of the V1200 setup *bottom row*. In blue the ADC is given.
The *second panel* shows the different terms in the ADC. The blue line represents the logarithmic derivative of the surface brightness and the black one the logarithmic derivative of the squared velocity dispersion. The green line is dominated by the value of the core radius reaching one at infinity.

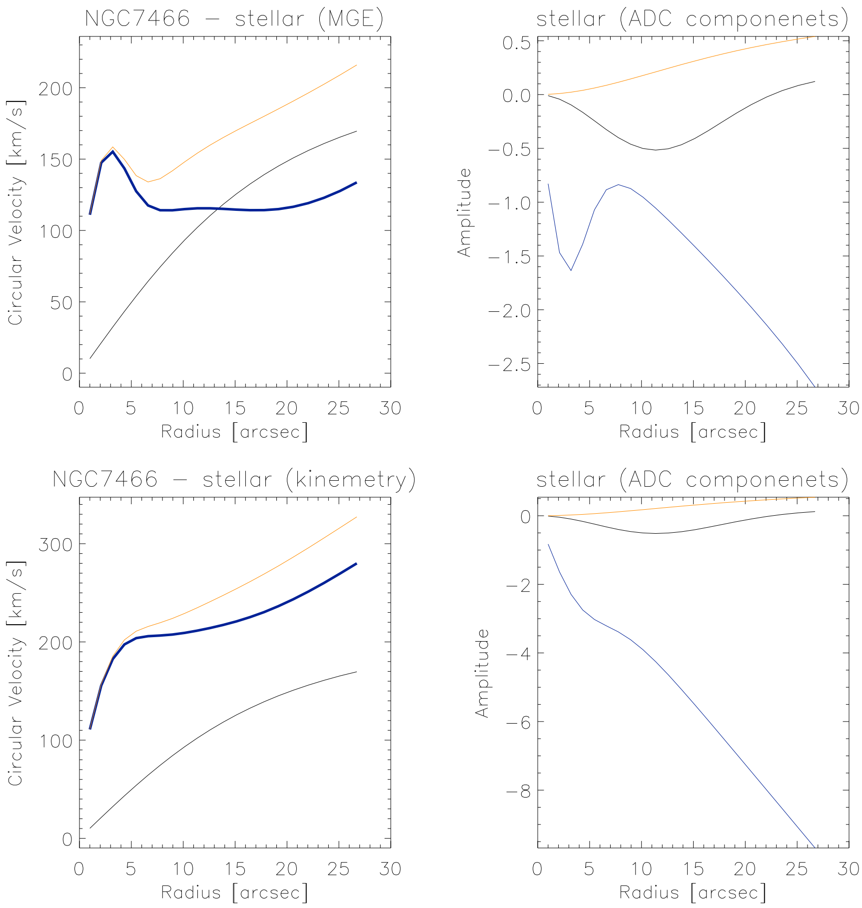

Figure A.53: The true circular velocity and ADC of NGC7466 obtained with the wrong surface brightness profiles.
The *first panel* shows the observed rotational velocity (black line) and the true circular velocity (orange line) for the stars obtained from the stellar surface brightness profile extracted with MGE from the SDSS z-band *top row* and extracted with kinemetry from the binned data of the V1200 setup *bottom row*. In blue the ADC is given.
The *second panel* shows the different terms in the ADC. The blue line represents the logarithmic derivative of the surface brightness and the black one the logarithmic derivative of the squared velocity dispersion. The green line is dominated by the value of the core radius reaching one at infinity.

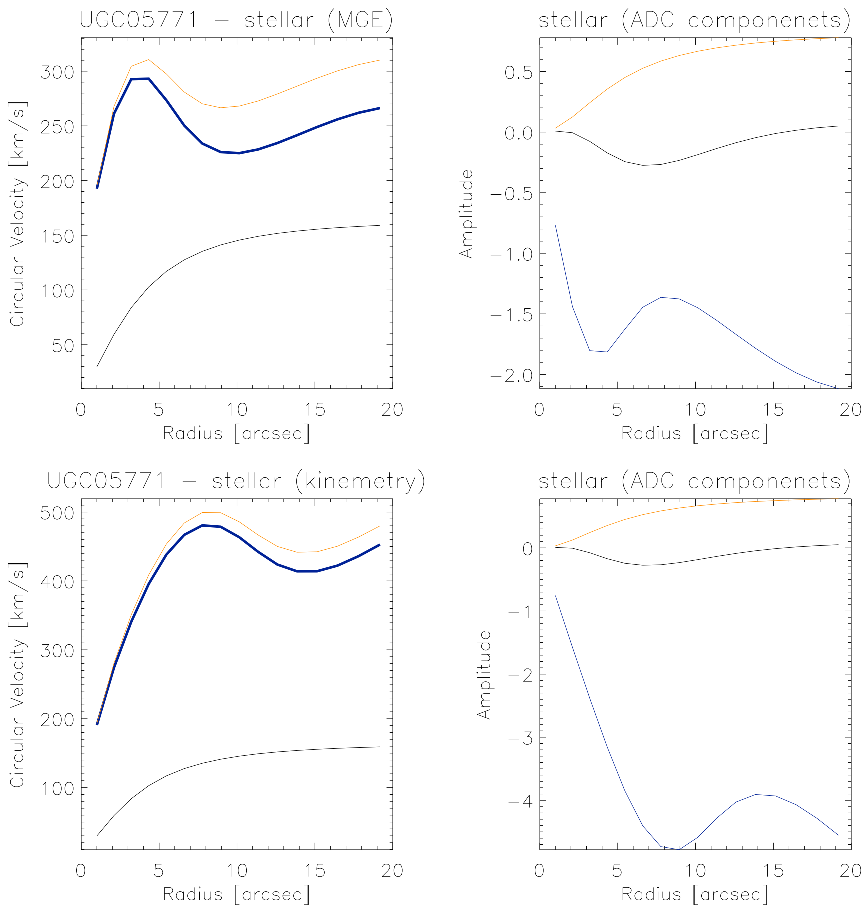

Figure A.54: The true circular velocity and ADC of UGC05771 obtained with the wrong surface brightness profiles.
The *first panel* shows the observed rotational velocity (black line) and the true circular velocity (orange line) for the stars obtained from the stellar surface brightness profile extracted with MGE from the SDSS z-band *top row* and extracted with kinemetry from the binned data of the V1200 setup *bottom row*. In blue the ADC is given.
The *second panel* shows the different terms in the ADC. The blue line represents the logarithmic derivative of the surface brightness and the black one the logarithmic derivative of the squared velocity dispersion. The green line is dominated by the value of the core radius reaching one at infinity.

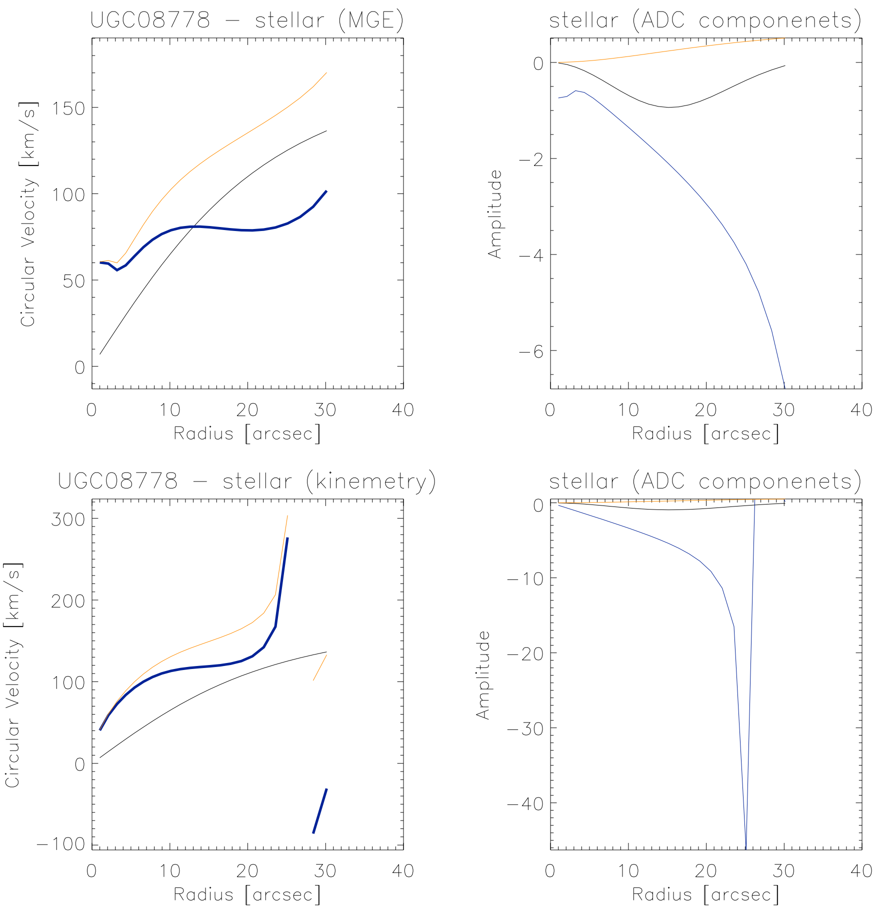

Figure A.55: The true circular velocity and ADC of UGC08778 obtained with the wrong surface brightness profiles.
The *first panel* shows the observed rotational velocity (black line) and the true circular velocity (orange line) for the stars obtained from the stellar surface brightness profile extracted with MGE from the SDSS z-band *top row* and extracted with kinemetry from the binned data of the V1200 setup *bottom row*. In blue the ADC is given.
The *second panel* shows the different terms in the ADC. The blue line represents the logarithmic derivative of the surface brightness and the black one the logarithmic derivative of the squared velocity dispersion. The green line is dominated by the value of the core radius reaching one at infinity.

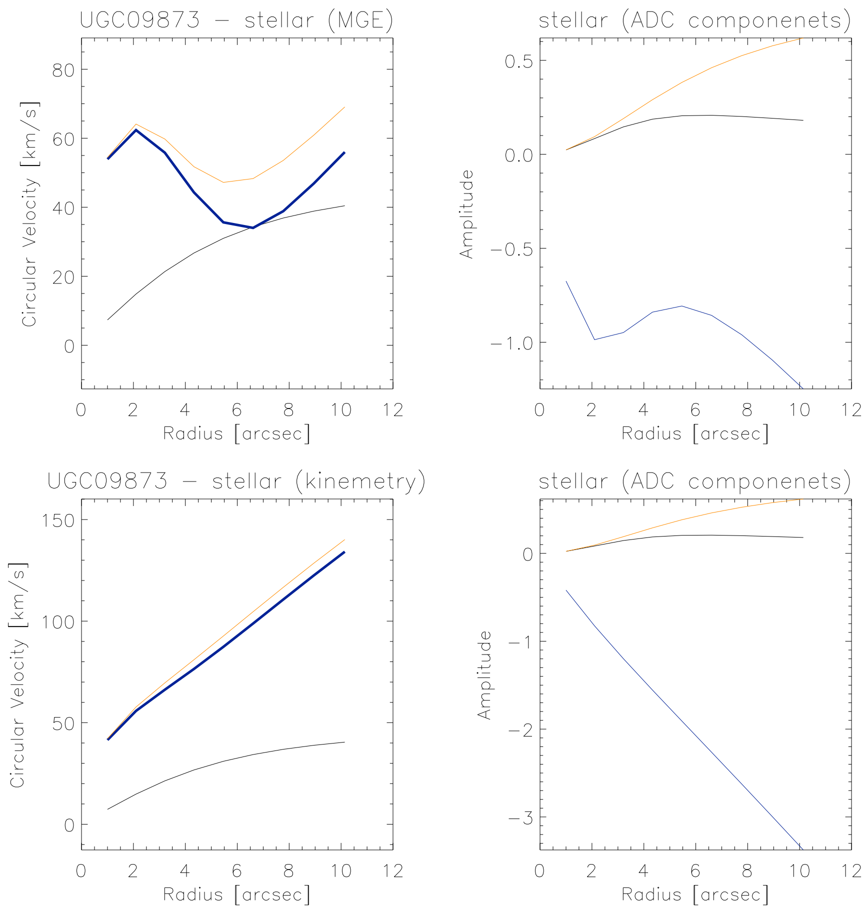

Figure A.56: The true circular velocity and ADC of UGC09873 obtained with the wrong surface brightness profiles.
The *first panel* shows the observed rotational velocity (black line) and the true circular velocity (orange line) for the stars obtained from the stellar surface brightness profile extracted with MGE from the SDSS z-band *top row* and extracted with kinemetry from the binned data of the V1200 setup *bottom row*. In blue the ADC is given.
The *second panel* shows the different terms in the ADC. The blue line represents the logarithmic derivative of the surface brightness and the black one the logarithmic derivative of the squared velocity dispersion. The green line is dominated by the value of the core radius reaching one at infinity.

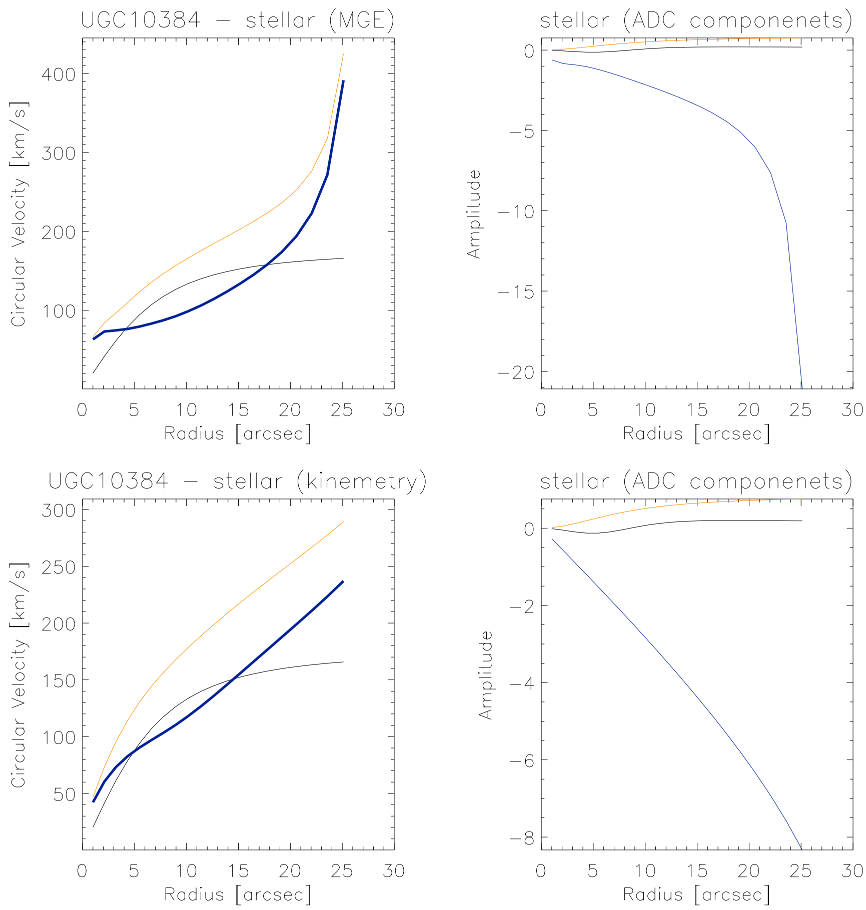

Figure A.57: The true circular velocity and ADC of UGC10384 obtained with the wrong surface brightness profiles.
The *first panel* shows the observed rotational velocity (black line) and the true circular velocity (orange line) for the stars obtained from the stellar surface brightness profile extracted with MGE from the SDSS z-band *top row* and extracted with kinemetry from the binned data of the V1200 setup *bottom row*. In blue the ADC is given.
The *second panel* shows the different terms in the ADC. The blue line represents the logarithmic derivative of the surface brightness and the black one the logarithmic derivative of the squared velocity dispersion. The green line is dominated by the value of the core radius reaching one at infinity.

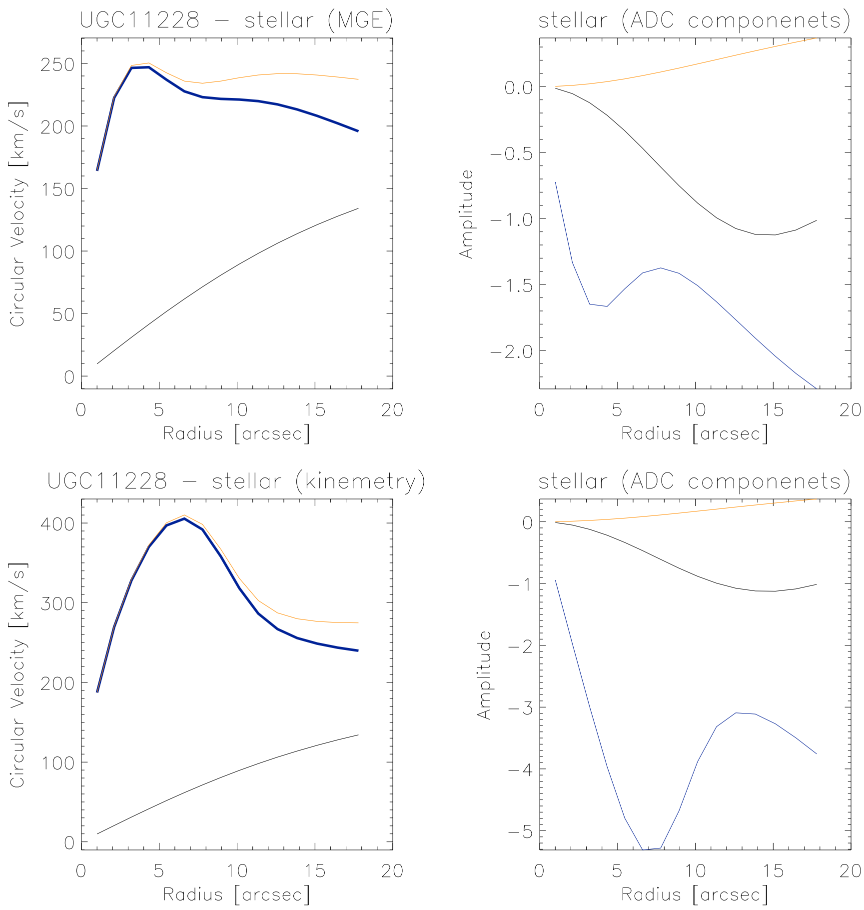

Figure A.58: The true circular velocity and ADC of UGC11228 obtained with the wrong surface brightness profiles.
The *first panel* shows the observed rotational velocity (black line) and the true circular velocity (orange line) for the stars obtained from the stellar surface brightness profile extracted with MGE from the SDSS z-band *top row* and extracted with kinemetry from the binned data of the V1200 setup *bottom row*. In blue the ADC is given.
The *second panel* shows the different terms in the ADC. The blue line represents the logarithmic derivative of the surface brightness and the black one the logarithmic derivative of the squared velocity dispersion. The green line is dominated by the value of the core radius reaching one at infinity.

A.8 Curriculum Vitae

Arzt Markus, BSc BSc

Education

1996 – 2000	**Kreativ - Volksschule**, *Schlierbach*, OÖ.
2000 – 2008	**BRG/BORG**, *Kirchdorf a.d. Krems*, OÖ, SC Member.
2009 – 2012	**Bachelor Astronomy**, *University of Vienna*.
2010 – 2013	**Bachelor Physics**, *University of Vienna*.
2012 – 2014	**Master Astronomy**, *University of Vienna*.
2012	**Summerschool**, *Alpbach*, TI.
2013	**Erasmus**, *Leuven*, BE.

Work Experience

2006 – 2011	**Traineeships**, *LKUF OÖ, Zementwerk Kirchdorf*.
2008 – 2009	**Civilian Service**, *LKH Kirchdorf*.
2012 – 2013	**Tutor**, *University of Vienna*, Department for Astrophysics.

Languages

German	**Mother tongue**
English	**Fluent**
Dutch	**Basics**
Latin	**Basics**